APPLICATION OF THE THERMAL TRANSIENT ANEMOMETER (TTA) FOR VEHICULAR SHROUD ANALYSIS

By

Travis Wesley

A THESIS

Submitted to
Michigan State University
in partial fulfillment of the requirements
for the degree of

Mechanical Engineering – Master of Science

2024

ABSTRACT

Experimental efforts were conducted with the use of a Thermal Transient Anemometer (TTA) to analyze flow distributions exiting a vehicular radiator. These experiments were motivated by the interest to explore how modifications to the geometry of the vehicle's shroud could potentially improve airflow across the face of the radiator. The TTA instrument is a frame composed of twenty-three cells that are capable of measuring the average velocity through the area of the cell. The twenty-three cells provide a velocity profile that spans across the outlet cross-section of the radiator.

The experiments recorded in this paper consists of three configurations for analysis: (i) radiator-only, (ii) radiator with the stock shroud and (iii) radiator with a modified shroud. The design of the modified shroud was first modeled using ANSYS Fluent to confirm the potential improvements to the flow of the system. With the improvements confirmed, the modified shroud was then constructed with the use of additive manufacturing. The radiator was first tested and analyzed without a shroud connected to the outlet to determine the flow distribution of the system independent from shroud effects. This analysis consisted of an averaged airflow velocity range of 2.26 m/s - 7.00 m/s. The airflow velocity range was accomplished by changing the pressure difference from the ambient (atmospheric) conditions to the upper receiver of the Axial Fan Research and Development (AFRD) facility. Following, the stock shroud and modified shroud were attached to the radiator and the flow distribution for the two configurations were recorded. The stock shroud and modified shroud experiments yielded in an averaged airflow velocity range of 0.78 m/s - 3.04 m/s and 0.77 m/s - 2.98 m/s, respectively. The flow rate of the system did not have a significant change between the two shroud geometries. For each shroud's measured flow rate, the curves tended to remain within the standard error envelope of each curve. The modified shroud was determined to increase the flow distribution with an improvement of the homogenization of the radiator's outlet profile.

ACKNOWLEDGEMENTS

I would like to acknowledge and sincerely thank my research advisor, Dr. Ricardo Mejia-Alvarez for his guidance throughout my graduate school experience. His advice and knowledge carried me throughout my research experience.

I would also like to thank the other faculty members and graduate students that helped me along the way. Specifically, Dr. John Foss and Dr. Bei Fan for their participation on my committee. Dr. Foss supported my research work throughout the entire process, and without his experience and knowledge I could not have been successful. Dr. Fan provided great feedback with her participation in my thesis defense. Many other graduate students provided much support and ideas to allow me to accomplish the challenges that arose throughout my research.

Ronald Semel, from the Ford Motor Company, provided much support with consistently meeting to provide feedback and advice for the research effort. He also participated in my defense committee and provided feedback that allowed to me to accurately correlate my research to the industrial applications.

Lastly, I would like to thank my family and friends for their support and patience throughout this project. Their support allowed for me to pursue and finish my graduate school research and thesis.

TABLE OF CONTENTS

1 Introduction

1.1 Motivation

Many automobiles, including both gasoline-powered and electrically powered, utilize a radiator for thermal energy management. As an example, a gas-powered internal combustion engine produces excess thermal energy that is dissipated from the radiator as airflow passes through the fins. The excess thermal energy is carried from the engine to the radiator using a fluid. This fluid absorbs the heat from the engine and sheds the heat when passing through the radiator. The radiator's fins help to distribute the thermal energy through conductive heat transfer in combination with the airflow that also removes the thermal energy by convective heat transfer.

Understanding how the airflow that passes through the radiator is distributed across the radiator's face can allow for more efficient thermal management designs to be implemented in this system. The performance of the radiator can vary as the inlet flow is varied at low to high speeds, where at lower speeds an exhaust fan may be utilized to draw flow through the system to increase the cooling rate. The performance of the radiator can be influenced by the shroud attached downstream of the inlet flow which can constrict the flow after it has passed through the radiator, causing certain areas of the radiator to experience a difference of the incoming flow velocity. By studying how changes to the shroud's geometry can be implemented to improve airflow characteristics across the radiator's face, the overall performance of the system can be improved.

1.2 Thermal Transient Anemometer

The Thermal Transient Anemometer (TTA) is a device that allows for a planer profile of fluid velocity to be measured. The current TTA was built in order to measure airflow velocity through a specific radiator, which is used for the studies done in this effort. The frame of TTA is split into twenty-three cells that allows for a full profile velocity to be measured as flow exits from the radiator. Each cell has tungsten wire that is strung across in a multi-X pattern. These wires measure the average flow rate through the individual cell. The frame is connected to an electrical control unit which controls the operations of the TTA through software located on a local computer. This control unit sends heating and sensing electrical currents to the tungsten wires. Utilizing the profile of the TTA for the purposes of this research, the effects the shroud has on the flow through the radiator can be measured. These measurements allow for the performance of the radiator to be analyzed based on the shroud effects.

The measurement of the fluid flow velocity is determined by a relationship between resistance decay of the tungsten wires and the fluid flow across the wires. Similar to hot wire anemometers, the resistance of the heated wire changes in the presence of a relatively cooler flowing fluid over the wires as convective heat transfer removes the thermal energy from the wires. The rate at which the air is moving is proportional to the change of the wire's electrical resistance. However, for the TTA's measurement process, the time duration in which it takes the sensing wire's resistance to decay to a predetermined resistance level after being heated is measured. The predetermined resistance level is based on a ratio that allows for the time constant of the rate of decay to be measured. The time constant can be related to the velocity, therefore allowing for the velocity of the fluid to be determined. Further explanation of this process is detailed in the Calibration section.

The TTA has many advantages for this particular application as it was designed with the motivation of being used for measurement of flow exiting a vehicular radiator. These advantages include not having to traverse the instrument as one would have to with a hot wire probe, minimal obstruction of the flow path through the system while recording data, and the ability to provide an averaged velocity distribution across the outlet plane of the radiator.

1.3 Previous Work

Previous works have been done in order to construct the TTA and apply the instrument in similar measuring environments. In a paper published by Foss et al. (2004) [3], the TTA was first introduced. The motivation for developing this instrument was for the use of measuring the flow distribution from a vehicular radiator. Dr. Foss et al. (2004) presented the capability of the TTA concept and its advantages for the particular use of measuring velocity profiles where the velocity may be varied. This paper also contains description behind the development and science of how the TTA is able to record averaged velocity readings. The TTA was revisited in a later paper, Dr. Foss et al. (2006) [2]. This work demonstrated the capability of the TTA to perform in the presence of varying turbulence and heat transfer. In a Master's thesis done by James Leung (2018) [4], the current TTA configuration was constructed and tested. Leung also described the calibration process, as well as documenting the performance of the TTA in the presence of a nonuniform velocity distribution. In a Master's thesis done by Sarah Plant (2020) [5], the calibration and performance of the TTA are described. Specifically, the performance of the TTA in nonuniform velocity distributions was further explored. These previous works, especially the last two thesis

works mentioned by Leung and Plant, provided a guide which allowed the present efforts to be accomplished.

1.4 Objectives

The aim of this study is to analyze the airflow through the radiator and quantify the effects the shroud has on the potential performance of the cooling system. Further, an analysis of the design of the shroud is visited to improve the airflow across the radiator. To accomplish this, the stock shroud that is currently being utilized (seen in Figure 1.1) is compared against a modified shroud constructed through the use of additive manufacturing (seen in Figure 1.2). The knowledge gained from this study can be utilized for the improvement of the vehicular cooling systems found in most gas-powered and electrical vehicles.

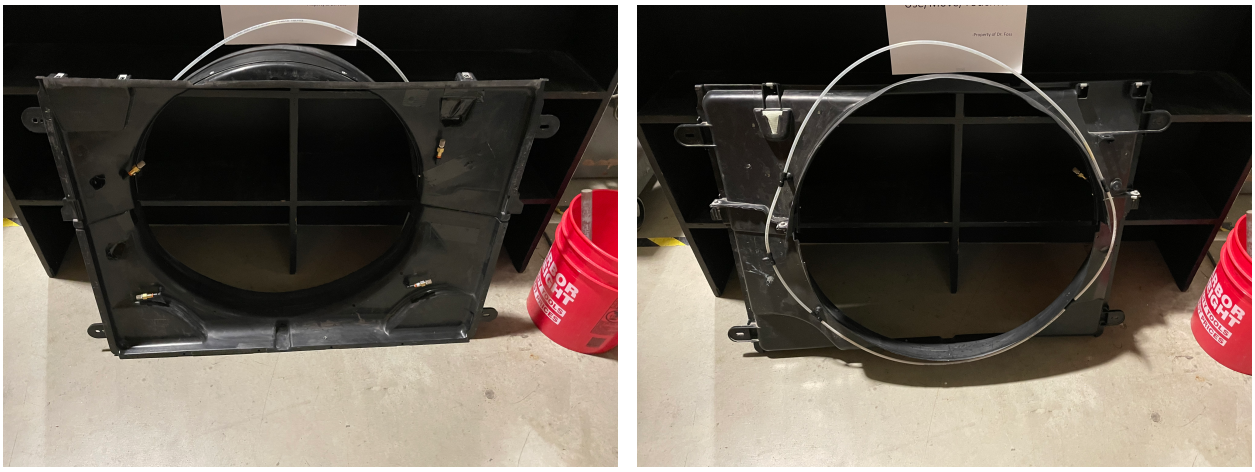

Figure 1.1: Stock Shroud

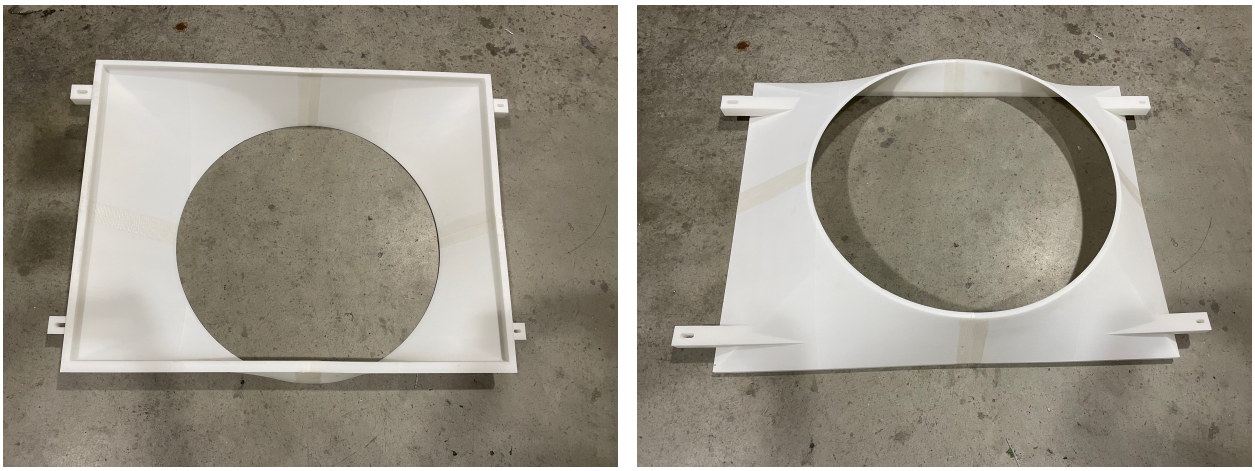

Figure 1.2: Modified Shroud

2 Facility, Equipment, and Instrumentation

2.1 AFRD Facility

The Axial Fan Research and Development (AFRD) facility is the basis for which the calibration and experiments with the TTA were conducted. The AFRD facility allows for airflow experiments to be conducted in various configurations utilizing the vertical wind tunnel system. This is accomplished by a blower inducing a pressure drop from the laboratory to the upper receiver of the AFRD, causing ambient air to flow through the inlet exposed at the top of the facility. The velocity of the air is controlled using a throttle that can adjust the outlet area of the blower that removes air from the facility. Increasing or decreasing the area results in a change to the mass flow exiting the system, thus allowing for the velocity to be varied.

The AFRD has a large inlet at the top of the structure. This inlet allows for the staging of equipment and behaves as the inlet to the vertical wind tunnel. For the calibration and experiments using the TTA in this document, this inlet is where the instrument is placed. The area of the inlet can be adjusted by placing frames to only allow airflow through the desired inlet area.

A schematic of the AFRD can be seen in Figure 2.1. The schematic and further detailed information regarding how the AFRD facility can be utilized can be found in Plant (2020) [5].

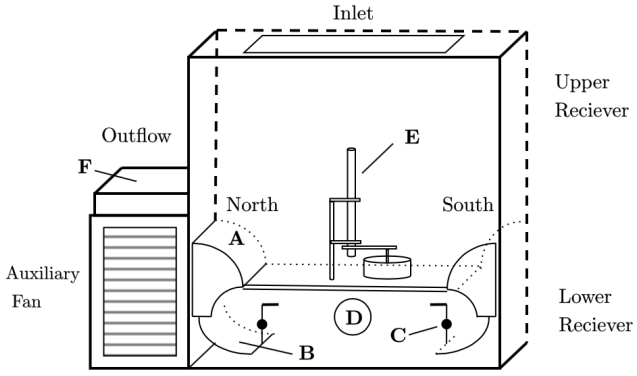

Figure 2.1: AFRD Facility Schematic

2.2 Thermal Transient Anemometer

The TTA is a device that can be used to measure spatially averaged air velocity; it is built to span a large rectangular region such as a vehicular radiator. The present TTA is separated into

twenty-three rectangular grid cells; see Figure 2.2.

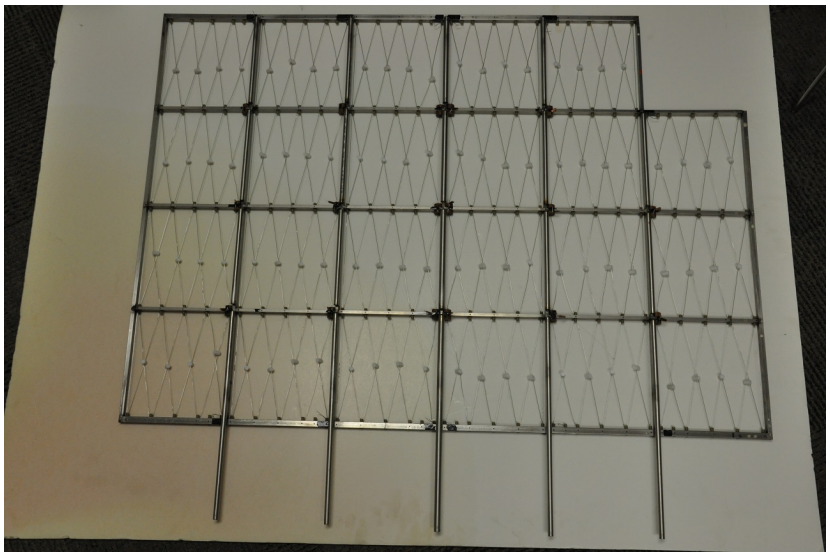

Figure 2.2: TTA Instrumentation

The TTA resembles a 4 x 6 grid pattern with a single cell missing. The reference layout of the cell numbering system for this research effort can be seen in Figure 2.3.

4	8	12	16	20	
3	7	11	15	19	23
2	6	10	14	18	22
1	5	9	13	17	21
R1	R2	R3	R4	R5	R6

Figure 2.3: TTA Cell and Row Orientation

The cell missing, which would be cell 24, was not fabricated due to design constraints of the testing shroud. The TTA frame is made of stainless steel. Each cell is wired with tungsten wire in a multi-X pattern passing through Garolite rods to insulate the wires from the frame. To prevent contact of the wires in the multi-X pattern, which could result in conductive heat transfer between the wires, Teflon spacers separate the wires in the crossing patterns. The tungsten wires are electrically connected through the use terminal blocks. The instrument is connected to an electronic control

unit, which is ultimately connected to the computer located at the facility. This control unit uses a 2 A electrical current that heats the tungsten wires, one row at a time, to increase the resistance of each wire for a set duration. Following this heating period, the control unit changes the electrical current to a 10 mA sensing current and measures the time in which it takes the wires to return to a set resistance. The time in which it takes the resistance to decay to this predetermined resistance can be related to the average velocity of the airflow through the cell. The rate of decay of the cell's sensing wires is shown in equation (2.1) below as noted by Plant (2020) [5],

$$\mathrm{R}^* = \frac{\mathrm{R(t)} - \mathrm{R_a}}{\mathrm{R_0} - \mathrm{R_a}} = \mathrm{e}^{\frac{-\mathrm{t}}{\tau}}, \tag{2.1}$$

where R^* is the dimensionless resistance value, R is the resistance of the wire, t is the measured time, and τ is the time constant of the decay. Subscripts a and 0 represent ambient and initial conditions, respectively. This equation allows for the measurement of the time duration starting after the sensing wire is heated to when the dimensionless resistance variable $\mathrm{R}^* = \mathrm{e}^{-1}$ has been reached, resulting in the time constant being determined as this is when $\mathrm{t} = \tau$. A full description of this process can be found in Leung (2018) [4].

The calibration of the TTA allows for each cell to individually measure the average velocity through the cell. This calibration is suggested to be done every few months of use to ensure any changes to the resistance of the wires is captured. Since each cell measures the fluid velocity individually, each cell must also be calibrated individually. This results in a set of three calibration constants found for each cell. The process for determining these constants is explained in the Calibration section.

2.2.1 Pressure Transducer

Two different pressure transducers were utilized in this research effort. The first pressure transducer, displayed in Figure 2.4, was used to measure the pressure difference from the ambient pressure and the pressure in the upper receiver of the AFRD controlled by the blower. This pressure transducer had one port open to the ambient pressure and the other connected to a tygon tube, connected to the upper receiver of the AFRD facility. This configuration allowed for the difference of the two pressures to be recorded with the use of a demodulator and data acquisition device. The demodulator used was a Validyne demodulator seen in Figure 2.5, which was able to deliver the

measurement data to the LabJack data acquisition device. The LabJack data acquisition device is discussed further in an upcoming section. This configuration allowed for the continuous measurements of the pressure difference to be recorded for both calibration purposes and experimental purposes.

Figure 2.4: Pressure Transducer

Figure 2.5: Validyne Demodulator

The other pressure transducer that was utilized, the MKS Baratron capacitance manometer seen in Figure 2.6, was used for the calibration of the fiber-film probe. This pressure transducer was connected to the slit-jet apparatus and was used to determine the pressure difference from the ambient pressure and the plenum pressure to determine the fluid flow velocity. The Baratron was also connected to the LabJack data acquisition device such that the pressure difference measurements could be recorded throughout the fiber-film probe's calibration process. Further explanation about the procedure of this calibration process is detailed in the Calibration section.

Figure 2.6: MKS Baratron Capacitance Manometer

2.2.2 CTA and Fiber-Film Probe

A fiber-film probe and constant temperature anemometer (CTA) were used in conjunction to measure airflow velocity. The fiber-film probe was used to measure the average flow velocity at a single position. This probe was connected to the CTA, which keeps the probe at a constant temperature and measures the voltage required to do so. The probe and CTA were then connected to the LabJack data acquisition device for recording the velocity measurements.

Both the CTA and the fiber-film probe were manufactured by Dantec Dynamics. The CTA used, referred to as Dantec Dynamic's MiniCTA, can be seen in Figure 2.7.

Figure 2.7: Dantec Dynamics MiniCTA

The fiber-film probe can be seen in Figure 2.8. The probe is composed of quartz-fibers with a diameter of 70 µm and an active sensing length of 1.2 mm. The fibers are covered by a nickel thin-film and then coated by quartz. This probe is capable of measuring one-dimensional gas flow velocities.

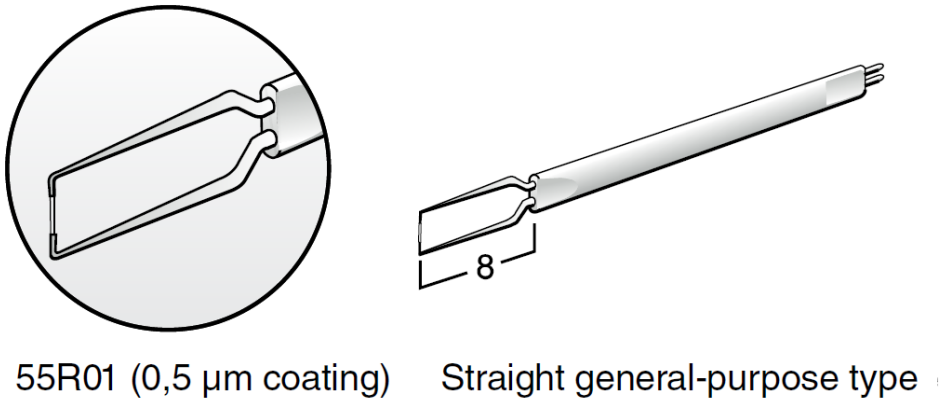

Figure 2.8: Dantec Dynamics Fiber-Film

2.2.3 LabJack DAQ

The LabJack data acquisition device used in this paper is the LabJack T-7 Pro board. This data acquisition device converts the analog input to a 16 bit digital format output. Software that is installed on the computer at the lab is able to store the measurements received from the LabJack. The LabJack was used for recording pressure measurements with both transducers and measurements taken by the fiber-film probe with the CTA. The device can be seen in Figure 2.9.

Figure 2.9: LabJack T-7 Pro

2.3 Slit-Jet

A slit-jet apparatus was used for the purpose of calibrating the fiber-film probe. This instrument has an established relationship of the fluid flow velocity as a function of the distance from the plenum face. The slit-jet configuration can be seen in Figure 2.10. A blower was attached to the lower portion of the slit-jet apparatus. The air flow can be controlled by opening and closing the inlet gate valve. Adjusting this valve controls the pressure in the plenum, thus allowing the flow velocity to be controlled. More details of the velocity relationship used for the calibration process are documented in the Calibration section and detailed further in Azar (1997) [1].

Figure 2.10: Slit-Jet Instrument

2.4 Radiator Housing

For the experiments conducted in this paper, a radiator housing structure was constructed for the mounting of the radiator. This configuration allowed for the flow to be directed only through the radiator and allowed for a shroud to be attached on the opposite side. The radiator housing was composed of slotted extruded aluminum bars to build the frame and supports of the radiator. Medium-density fiberboard was used to create an enclosed surface around the frame. Foam pads were placed around the perimeter of the bottom of the housing structure in order to create a seal as the weight of the mount compressed the foam. Any remaining areas of potential leakage concern were then covered in tape to ensure an airtight seal. This structure can be seen in Figure 2.11.

Figure 2.11: Radiator Housing

3 Calibration

3.1 TTA Calibration

This section will give a brief overview of the calibration procedure for the TTA. The Master's thesis by Plant (2020) [5] was followed closely to accomplish the calibration for the use of the TTA documented in this paper and can be used as a reference for more details about this process. This process can also be found documented in the Master's thesis by Leung (2018) [4]. The TTA was calibrated utilizing the AFRD facility previously described. The TTA was placed on a medium-density fiber board that reduced the inlet of the AFRD to the size of the TTA frame. To ensure uniform flow into the inlet, quarter-rounds were placed to straighten the flow as it passes over the TTA and into the inlet. The set up of the calibration process can be seen in Figure 3.1.

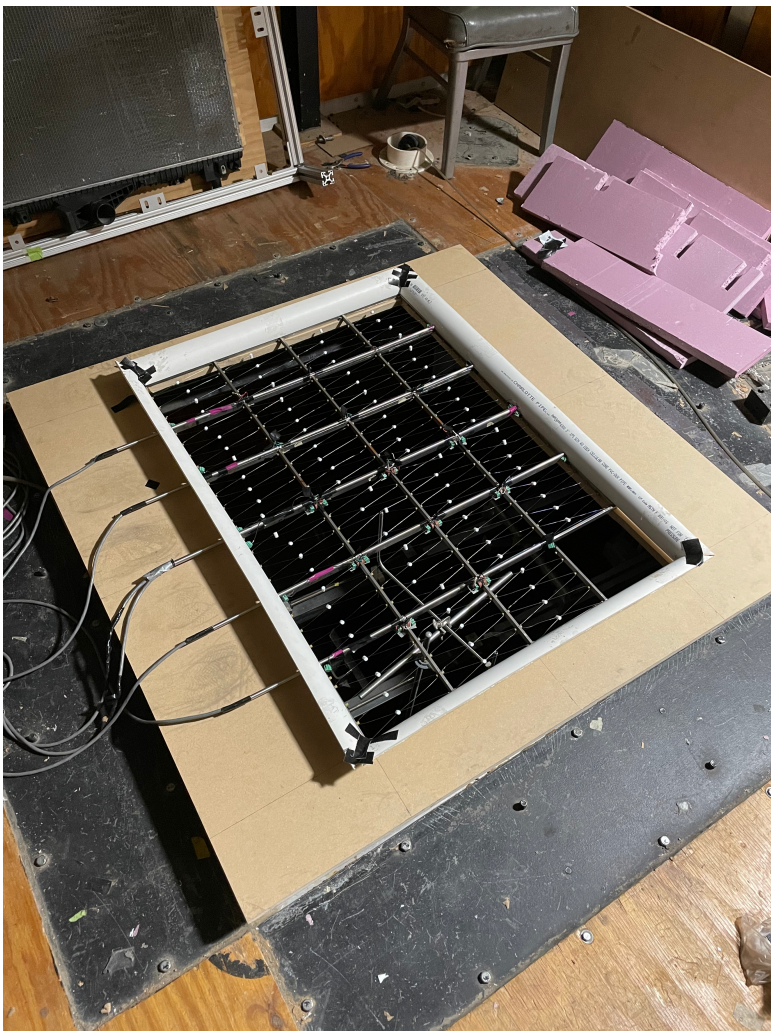

Figure 3.1: TTA Calibration Set Up

In order to perform the calibration, another technique must be used to determine the

average fluid flow velocity of the air entering through the AFRD's inlet. This was able to be accomplished utilizing two different methods in this research. One method utilized a pressure transducer to determine the pressure difference between the ambient pressure and the pressure in the upper receiver of the AFRD. The other method was done by using a calibrated fiber-film probe with a CTA. These methods are described in further detail in the following sections.

At a given flow velocity, determined by using one of the previously described methods that is independent of the TTA, software at the lab in combination with the electronic control unit is able to measure the inverse of the time constant, τ^{-1}, exhibited for each cell. This resulted in fifteen to sixteen measurements of the τ^{-1} value at a single fluid flow velocity condition. The average of the recorded τ^{-1} values was determined and related to the separately measured average flow velocity condition. This process was repeated again at each of the other desired flow velocity conditions to develop the data points necessary for the full velocity range. Once all of the targeted velocity steps for the specified range of flow velocity has been fully recorded (recommended at least ten velocity steps) the τ^{-1} values are plotted against the measured average flow velocities. The calibration constants for each individual cell can determined through the use of a curve fitting tool, utilizing a least squares method for fitting the curve to the relationship of the sensing wires and fluid velocity. The relation between the τ^{-1}value and fluid flow velocity is displayed in equation (3.1).

$$\tau^{-1} = A \cdot U^{B} + C \qquad (3.1)$$

Post-processing was done after the measurements to ensure the behavior of each cell on the TTA were reasonable and no technical malfunctions have occurred. Common issues that can cause errors in measurements include loose connection of the sensing wires at the terminal boxes of the TTA and/or the sensing wires in contact with the frame of the TTA resulting in electrical short circuits. Once the post-processing analysis has been conducted, the TTA could be used to conduct measurements with the determined calibration constants.

3.2 Pressure Transducer

For one calibration method of the TTA, a pressure transducer was utilized to determine the average flow velocity that entered through the AFRD inlet. This was done by measuring the

pressure difference of the ambient pressure and the pressure in the upper receiver of the AFRD. The incoming flow velocity can be related to that of the measured pressure difference with Bernoulli's equation (3.2),

$$\Delta P = \frac{1}{2}\rho U^2, \tag{3.2}$$

where $\Delta P = P_a - P_{UR}$, P being the pressure measurements, subscripts a and UR denoting the ambient and upper receiver properties, respectively.

To determine the ambient air density for the velocity calculation, the temperature and ambient pressure were measured such that the ideal gas law (3.3) could be used to calculate the density.

$$P = \rho R_g T \tag{3.3}$$

The temperature was measured via a thermometer placed in the laboratory and the ambient pressure was determined from the Lansing Airport measurements, which is nearby and at a relatively same altitude. Rearranging equations (3.2) and (3.3), the average velocity can be determined as displayed in (3.4).

$$U_{avg} = \sqrt{\frac{2 \cdot \Delta P_{avg}}{P_a/\left(R_g \cdot T_a\right)}} \tag{3.4}$$

The TTA was calibrated with the pressure transducer at ambient conditions of 1020.6 mb and 26 C. The velocity range measured by the pressure transducer resulted in a calibration range 1.33 - 11.96 m/s. With the flow velocity able to be determined, the previously described calibration process of the TTA could be followed. The ten velocity steps used in the calibration process can be seen in Table 3.1. Figure 3.2 shows the calibration plot of the first row, containing cells 1 - 4. The calibration constants for all cells can be found in Table A.1. Calibration plots for each row containing all twenty-three cells can be seen in the Figures A.1 – A.6.

Table 3.1: Velocity and Pressure Measurements for TTA Calibration with Pressure Transducer

Velocity Step	ΔP (Pa)	U_{avg} (m/s)
1	1.05	1.33
2	1.40	1.53
3	1.69	1.69
4	3.03	2.26
5	4.86	2.86
6	8.74	3.83
7	21.07	5.95
8	38.04	8.00
9	59.24	9.98
10	85.04	11.96

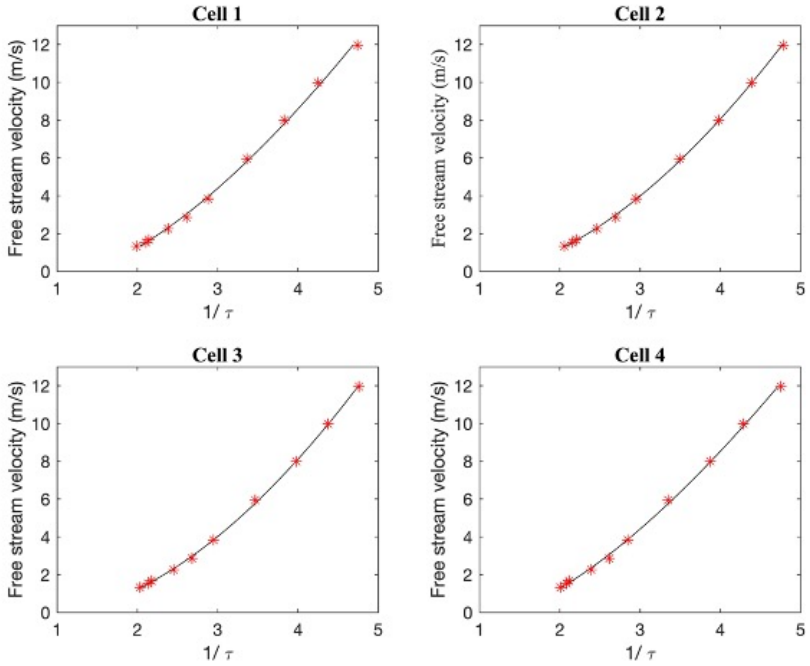

Figure 3.2: Cells 1-4 Calibration Curves - Pressure Transducer

3.2.1 Fiber-Film Probe

The fiber-film probe was also utilized to calibrate the TTA. The fiber-film probe offered the ability to calibrate the TTA at a lower velocity range than the pressure transducer due to the

sensitivity of the transducer. This probe needed to be calibrated before being used to calibrate the TTA, with details described in the following section. With the probe calibrated, the velocity the probe is experiencing can be determined by using the equation below (3.5).

$$U = \left(\frac{E^2 - A}{B}\right)^{\frac{1}{C}} \quad (3.5)$$

This equation relates the voltage measurements, E, to the flow velocity, U, using the calibration constants. The calibration constants of probe are displayed in the following section.

The fiber-film was placed slightly below the sensing wires of the TTA, approximately 4 cm below, in order to determine the average velocity of flow entering the inlet of the AFRD during the TTA calibration process. This configuration can be in Figure 3.3.

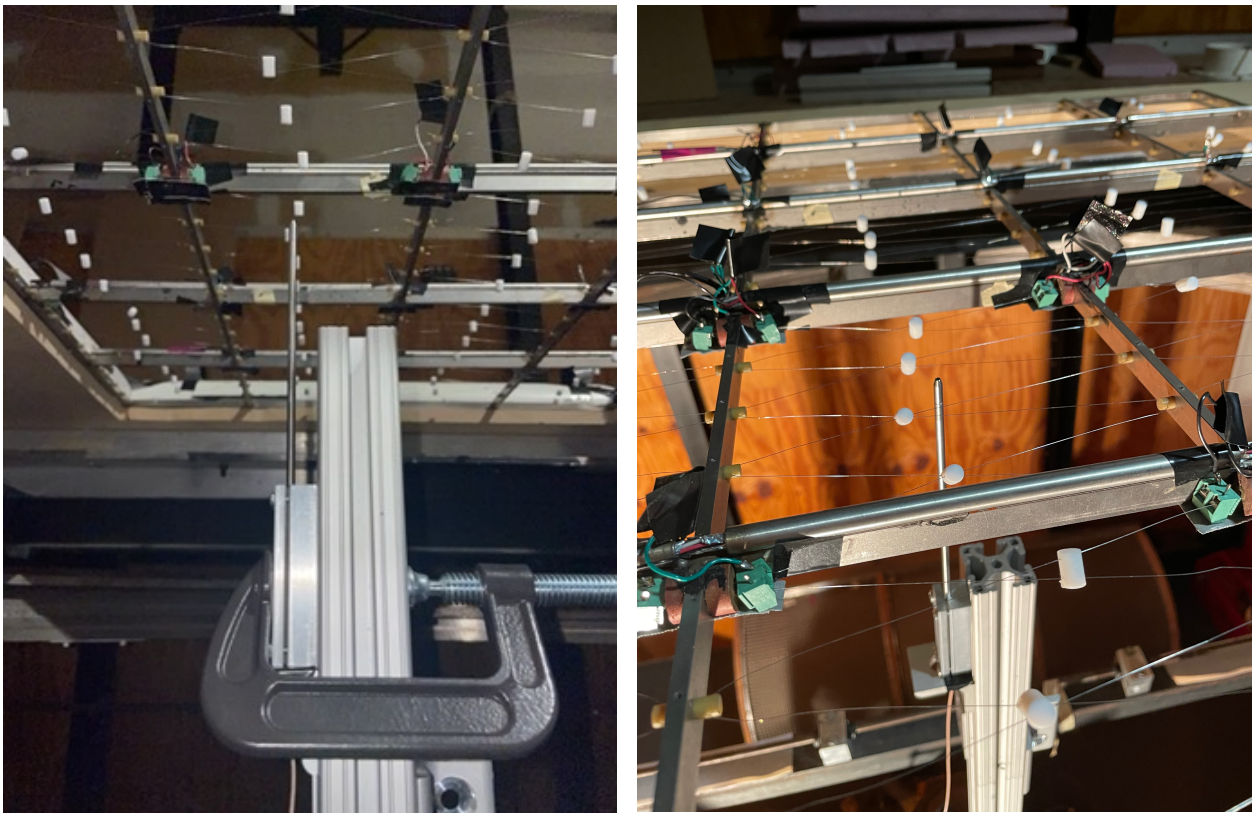

Figure 3.3: Fiber-film probe position for TTA calibration

Similar to the pressure transducer, the probe was also used to determine the average velocity throughout the entire calibration process of the TTA. The average velocity range measured by the fiber-film probe was 0.34 - 9.32 m/s. The twelve velocity steps used in the calibration process can be seen in

Table 3.2. Figure 3.4 shows the calibration plots of row 1, containing cells 1 - 4. The change from ten velocity steps to twelve when going from the pressure transducer to the fiber-film probe was done to ensure more lower velocity points were recorded for a better curve fitting in the lower velocity range. The calibration constants for the TTA with this method can be seen in Table A.2. All calibration plots can be seen in the Figures A.7 – A.12.

Table 3.2: Velocity and Pressure Measurements for TTA Calibration with Fiber-film Probe Data

Velocity Step	E (V)	U_{avg} (m/s)
1	1.33	0.34
2	1.42	0.53
3	1.48	0.71
4	1.53	0.90
5	1.61	1.27
6	1.67	1.59
7	1.72	1.87
8	1.85	2.93
9	1.94	3.92
10	2.09	6.03
11	2.22	8.30
12	2.26	9.32

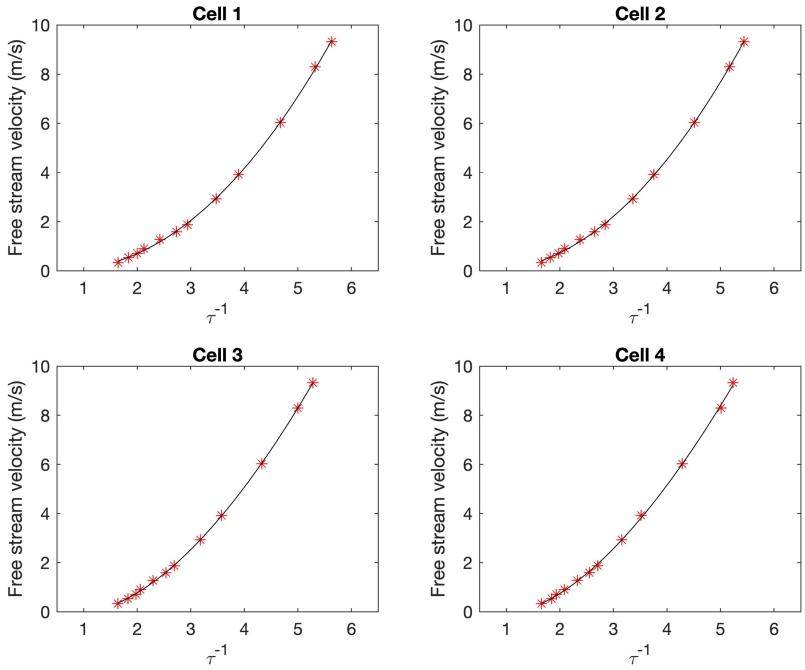

Figure 3.4: Cells 1-4 Calibration Curves - Fiber-film Probe

3.3 Fiber-Film Probe Calibration

The calibration of the fiber-film probe was done using a slit-jet instrument located in the facility. The probe was calibrated by traversing the probe at a series of determined positions relative to the plenum of the slit-jet. These positions spanned from inside to outside of the slit-jet's plenum plane. The traversing was done with the probe attached to a linear translation stage that used a micrometer, allowing for precise traversing of the probe. The advantage of using the slit-jet was the relationship that existed from the variation of air velocity with the distance relative to the plenum of the slit-jet. This relationship is described more in the following section and can also be found documented in Azar (1997) [1].

The calibration was split into two continuously measured processes: (i) adjustment of the probe location relative to the plenum using the linear stage while keeping the flow velocity constant and (ii) adjustment of the gated valve that controlled the flow velocity while keeping the probe in a fixed location. The velocity adjustment was accomplished by increasing the area of the inlet to the blower, resulting in an increased velocity at the outlet of the slit-jet.

First, the probe began inside the plenum of the slit-jet at a particular slit-width value. This is determined by measuring the width of the outlet of the slit-jet, W, and determining the distance

the fiber-film is from the plenum, x, resulting in the slit-width ratio x/W which can be seen in Figure 3.5. Using the relationship between the slit-width and the velocity distribution (seen in Figure 3.7 in the slit-jet subsection), the target stations were determined in order to record velocity steps for the lower region for the calibration velocity range. The probe was traversed to the eleven different stations, beginning at a slit-width position of $x/W = -1.0$ and ending at $x/W = 0.0$.

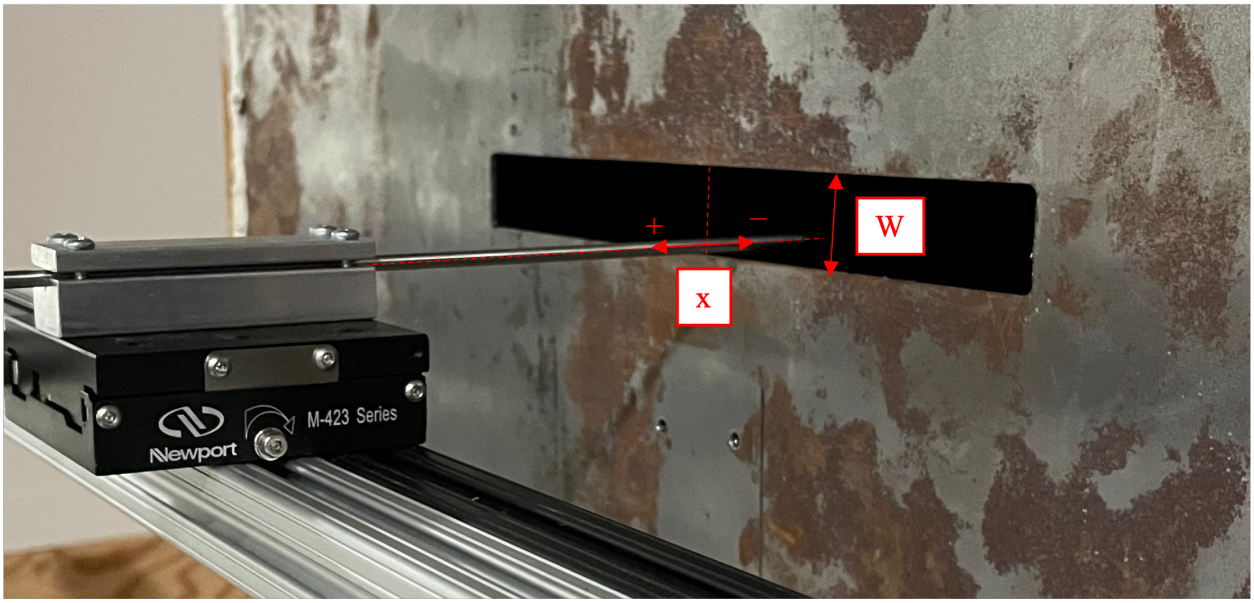

Figure 3.5: Diagram of Slit-Jet Dimensions for Slit-width Measurement

Continuing the measurements with the probe fixed at the $x/W = 0.0$ position, the throttle of the slit-jet was increased in six steps in order to reach velocity points at the higher region of the calibration range.

This calibration process yielded seventeen total measurement locations in which the calibration range of the probe resulted in 0.48 - 9.46 m/s. The velocity measurements can be seen in Table 3.3 and the calibration curve displayed in Figure 3.6.

Table 3.3: Fiber-film Probe Calibration Data

x/W	$u(x)/U_0$	ΔP (Pa)	U_0 (m/s)	U_{calc} (m/s)
-1.0	0.184	4.36	2.72	0.48
-0.9	0.201	4.36	2.72	0.52
-0.8	0.221	4.36	2.72	0.57
-0.7	0.246	4.36	2.72	0.64
-0.6	0.276	4.36	2.72	0.71
-0.5	0.313	4.36	2.72	0.81
-0.4	0.358	4.36	2.72	0.92
-0.3	0.414	4.36	2.72	1.07
-0.2	0.482	4.36	2.72	1.24
-0.1	0.562	4.36	2.72	1.45
0.0	0.648	4.36	2.72	1.66
0.0	0.648	5.62	3.09	1.94
0.0	0.648	12.65	4.63	2.97
0.0	0.648	22.49	6.17	3.96
0.0	0.648	50.60	9.26	6.00
0.0	0.648	89.96	12.35	7.95
0.0	0.648	123.00	14.44	9.46

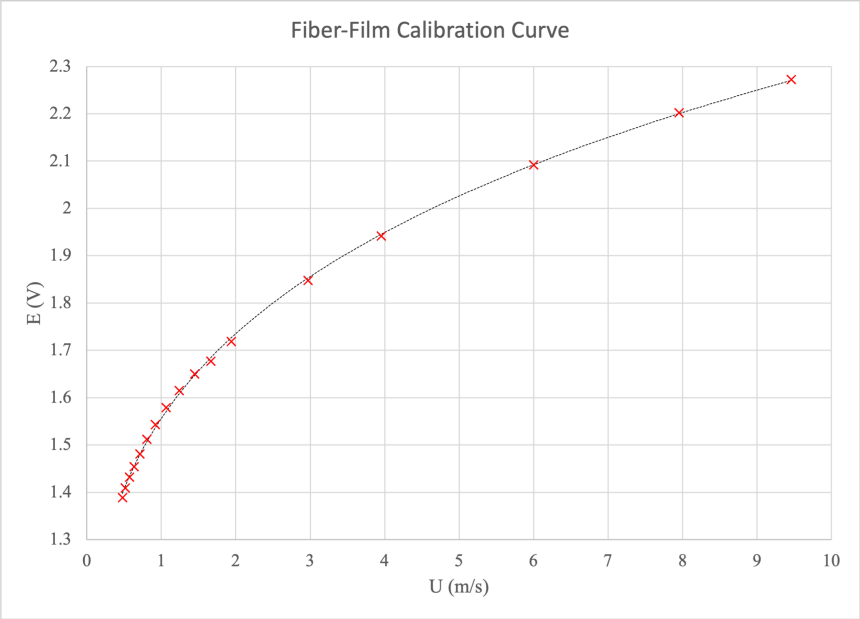

Figure 3.6: Fiber-film Calibration Curve

Table 3.4: Fiber-film Probe Calibration Constants

A	B	C
0.656	1.765	0.416

3.3.1 Slit-Jet

The slit-jet was utilized for the calibration of the fiber-film probe. This instrument was used due to the known velocity variation, $u(x)/U_0$, related to the slit-width, x/W, position from the plenum, for both into and out from the plane of the plenum. The variable $u(x)$ is the flow velocity as a function of x and U_0 is the maximum flow velocity measured at the vena contracta. This relationship can be seen in Figure 3.7 and described in Azar (1997) [1].

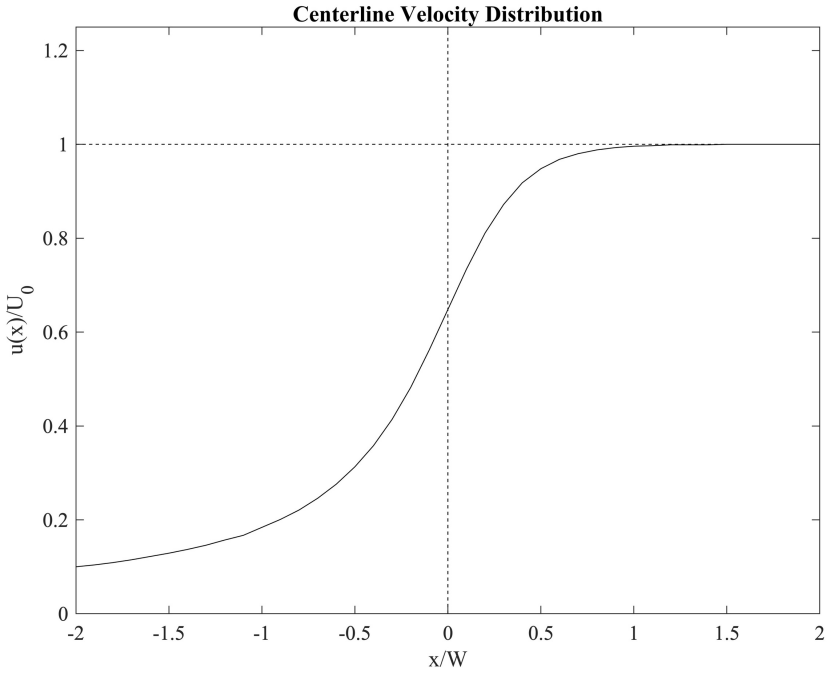

Figure 3.7: Slit-Jet Centerline Velocity Distribution

Due to this relationship, lower velocities are able to be achieved by traversing the probe into the slit-jet. This was important due to the sensitivity of the pressure transducer used to determine the flow velocity of the slit-jet, which would not be able to accurately measure the lower velocities needed for the analysis done in the experiments. Therefore, a higher flow velocity could be set, knowing that the velocity inside of the plenum would be lower as the probe is moved inward. The fiber-film probe can be seen in relation to the slit-jet plenum in Figure 3.8.

Figure 3.8: Slit-Jet Configuration for Fiber-film probe Calibration

4 Numerical Results

A numerical analysis was conducted for both the stock shroud and modified shroud geometries. First, the stock shroud was analyzed to determine the current performance of the shroud configuration to serve as a baseline for the modified shroud. Following, the shroud was redesigned to create the modified shroud's geometry with the goal of improving the flow by relieving the restriction through the radiator caused downstream by the shroud. Once the modified shroud was modeled, the geometry was analyzed in the same way as the stock shroud to demonstrate an increased performance of the flow through the system. Following the numerical analysis, the redesign of the shroud was 3D printed for experimental testing and is described further in the experimental results section.

For the purposes of this research, the numerical analysis was conducted to substantiate that flow improvements have been made with the redesigned geometry of the stock shroud in order to create the modified shroud. This numerical analysis was not done in order to draw reliable conclusions about the performance of either shroud geometries. Therefore, many simplifications and default software options were utilized for the set up and solution of the analysis in order to get a proof of concept for the modifications that were made.

4.1 Numerical Method

ANSYS Fluent was used as the Computational Fluid Dynamics (CFD) software for the numerical computations. This software utilizes a Finite Volume Method (FVM) to solve the governing equations of the system. The shroud simulations were done using the modeled geometries of the stock shroud and the modified shroud. The CFD geometries were prepared in SolidWorks by creating a volume in which the fluid would be modeled. This process consisted of taking the original shroud geometry, which was provided for the stock shroud, and surrounding it with the potential fluid field. The volume of the shroud geometry was then subtracted from the fluid field and the region that would remain inside of the shroud was kept. This region served as a negative image of the shroud, allowing for the volume to represent the area that would come into contact with the shroud surfaces. This area began at the rectangular inlet of the shroud and moved to the circular outlet. An example of the fluid volume with the surfaces of the stock shroud subtracted can be seen in Figure 4.1.

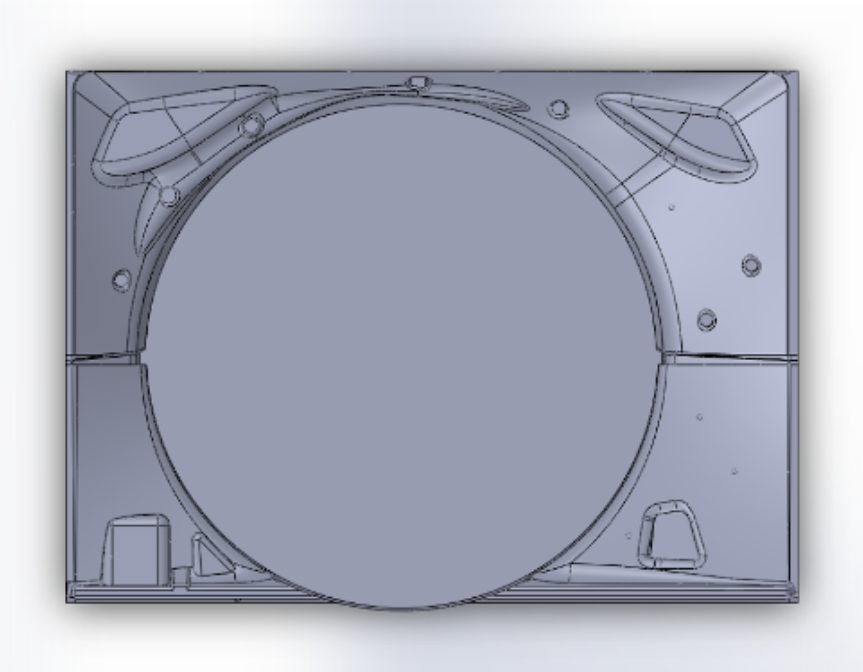

Figure 4.1: Stock Shroud CFD Volume

4.1.1 Set Up and Boundary Conditions

The shroud simulations were set up with identical boundary conditions to keep consistency when comparing the geometries. A distributed velocity inlet condition was used to simulate the distributed outlet velocity from the radiator as it enters the inlet of the shroud. This velocity was measured from a previously recorded experiment consisting of the radiator without a shroud attached. A uniform pressure outlet condition was used to simulate the pressure difference from the inlet of the radiator to the upper receiver in the AFRD facility, which was also determined from previous measurements. For the remaining area between the simulated TTA cells, the average measured velocity was implemented as a velocity inlet condition. All other boundaries, composed of the sides of the simulated TTA cell pattern and the surfaces of the shrouds, were set to solid wall no-slip boundary condition. This was done to remove the effects of the material surfaces and measure the effects due to the geometry only.

For the inlet velocity condition, a grid of twenty-four TTA cell sized rectangles were positioned to form a distributed inlet flow that would be imposed based on TTA measurements from the radiator, this geometry can be seen in Figure 4.2. These rectangular surfaces were raised 2 cm from the surface of the shrouds inlet such that the flows had time to develop. The cell walls parallel with the inlet plane of the shroud were assigned a velocity value corresponding to previous measurements, displayed in Figure 4.3. These measurements were recorded from a previous

radiator only velocity recording at a pressure difference of $\Delta P = 57.04$ Pa.

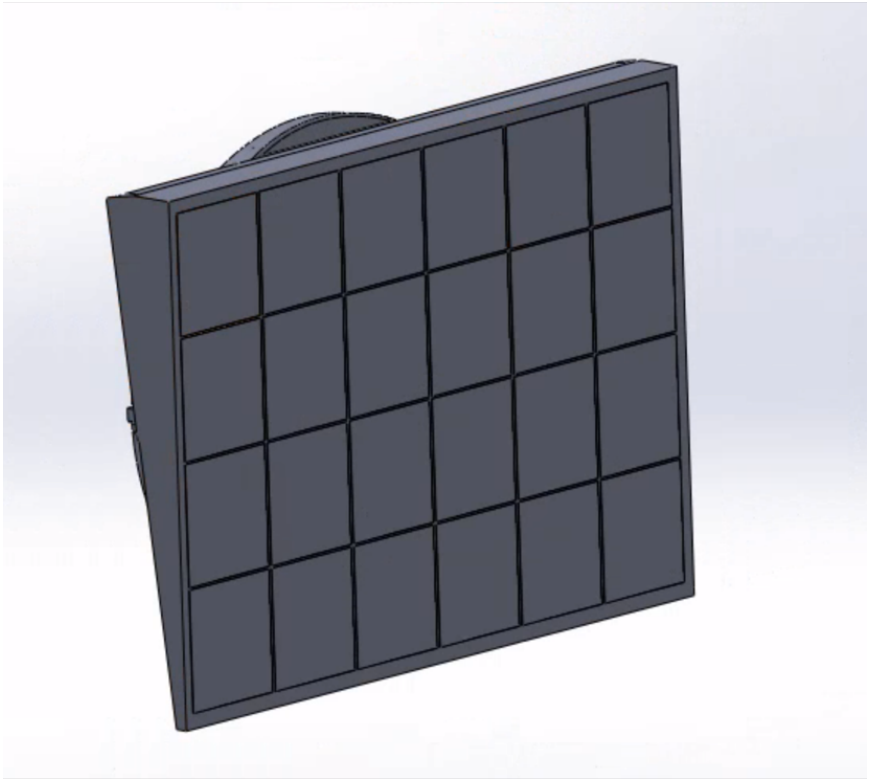

Figure 4.2: Inlet View of Shroud CFD Geometry

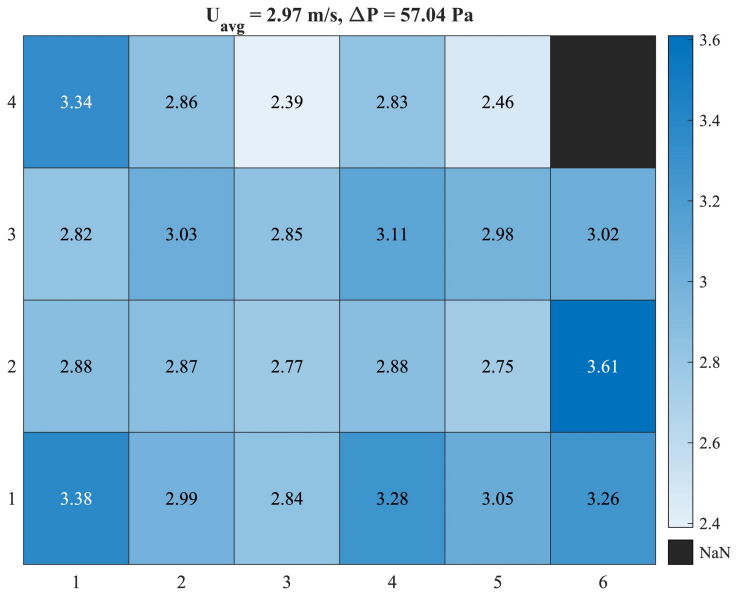

Figure 4.3: Inlet Velocity Boundary Condition Distribution

More information regarding specifics of the mesh sizing parameters, solution procedure, and convergence criteria can be found in the Numerical Results section of the Appendix.

4.1.2 Mesh Convergence

To determine if the mesh size was sufficient, a mesh convergence check was done for the stock shroud geometry. This consisted of running the simulation with a relatively coarse and a relatively fine mesh, then comparing the results following the simulations to ensure that the changes to the mesh size did not significantly impact the solutions.

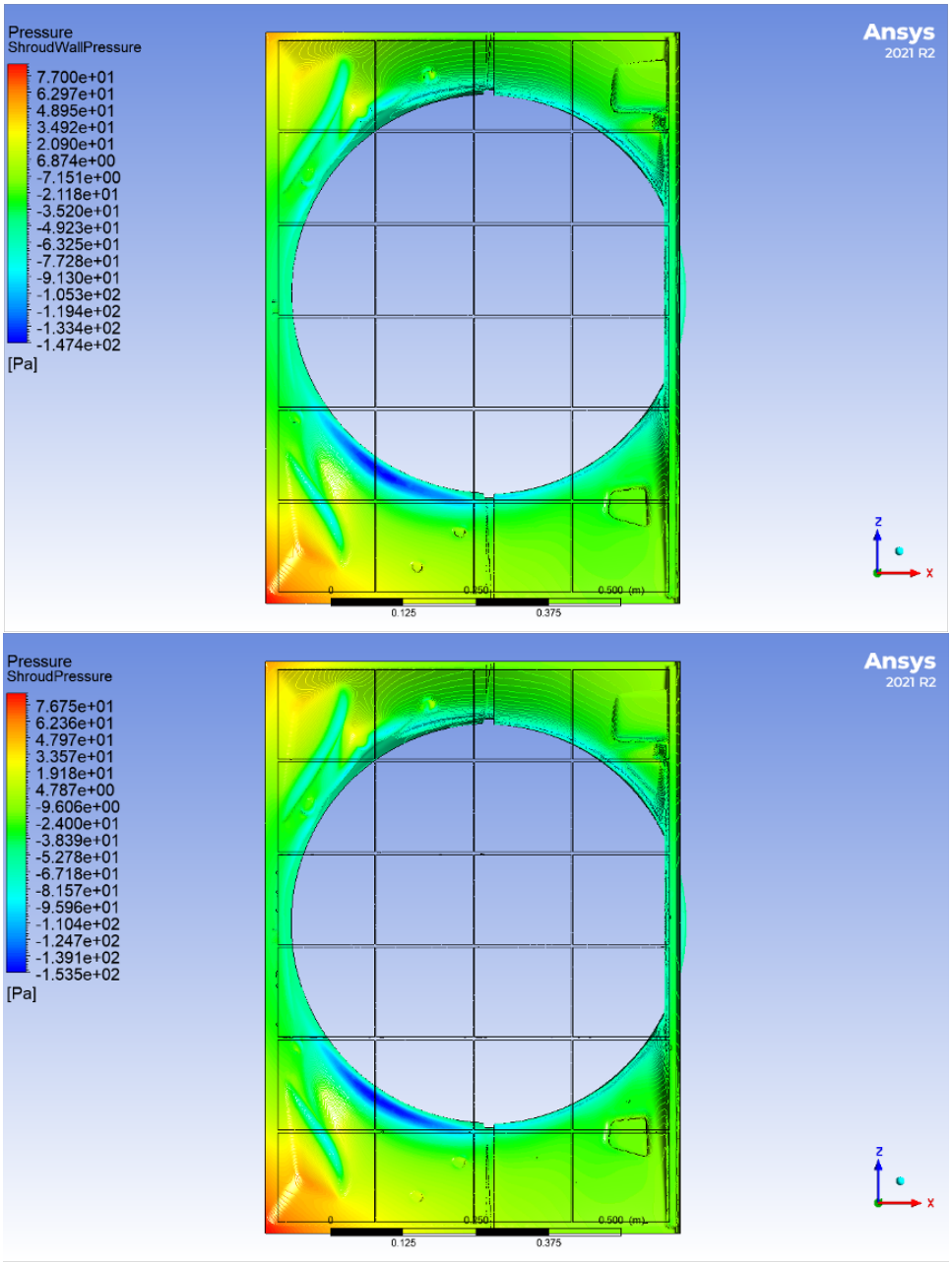

Figure 4.4: Pressure Contour Mesh Comparison
(Above: Default Mesh, Below: Fine Mesh)

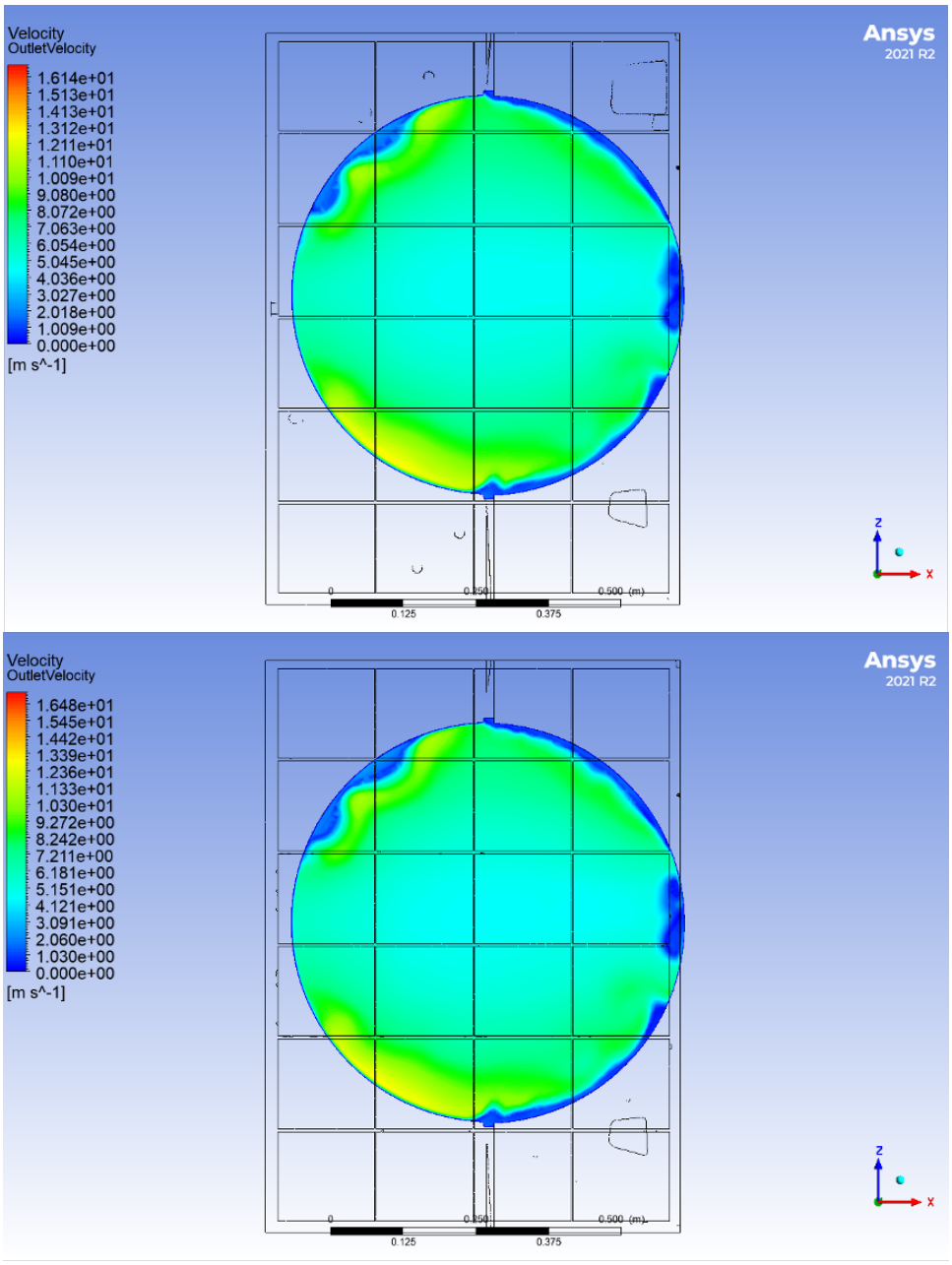

Figure 4.5: Outlet Velocity Contour Mesh Comparison
(Above: Default Mesh, Below: Fine Mesh)

The contours for both the shroud wall pressure and the outlet velocity appeared to be nearly identical. The shape of the contours appeared to remain unchanged when increasing the mesh. The maximum and minimum pressures modeled on the shroud surface remained within 5% of the default mesh, with the majority of the values that are on the surface inferred to be even more similar than the extremes. Similarly, the maximum outlet velocity increased by approximately 2% and the minimum remained at 0 m/s. This step confirmed that the mesh process used was adequate in sizing for this analysis.

4.2 Results

4.2.1 Stock Shroud Analysis

The geometry of the stock shroud was provided for the use of numerical simulation and can be seen in Figure 4.6. This geometry needed to be altered slightly by removing miscellaneous holes and geometries that caused issues when preparing for the CFD simulation.

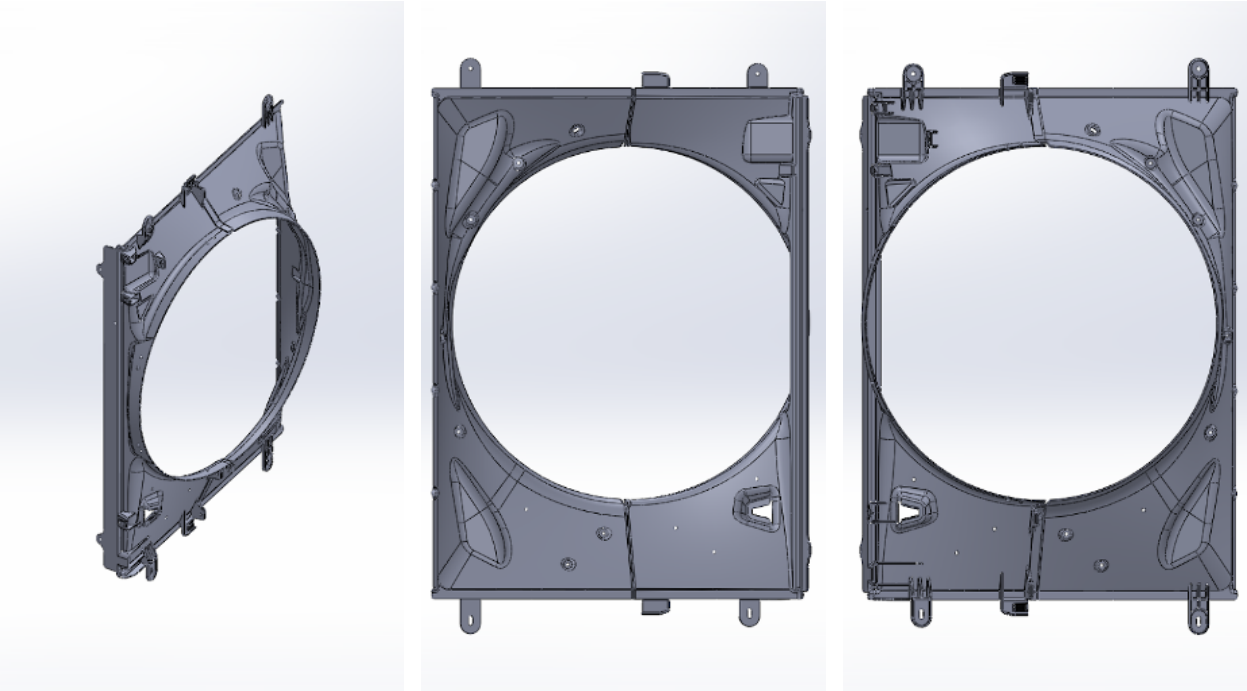

Figure 4.6: Stock Shroud CAD Model
(Left: Angled View, Middle: Inlet View, Right: Outlet View)

A mesh was applied to the volume of the fluid domain, with more details in the Appendix, and was used to solve the modeled fluid volume for the simulation. The statistics of the mesh used can be seen in Table 4.1.

Table 4.1: Stock Shroud CFD Mesh Statistics

	Nodes	Faces	Cells
Boundary	1,228,487	330,104	-
Interior	6,971,362	10,489,797	1,971,575

Utilizing the imposed boundary conditions described previously, the CFD simulation was solved. The modeled pressure contours on the shroud and the velocity contour of the outlet can be seen in Figure 4.7.

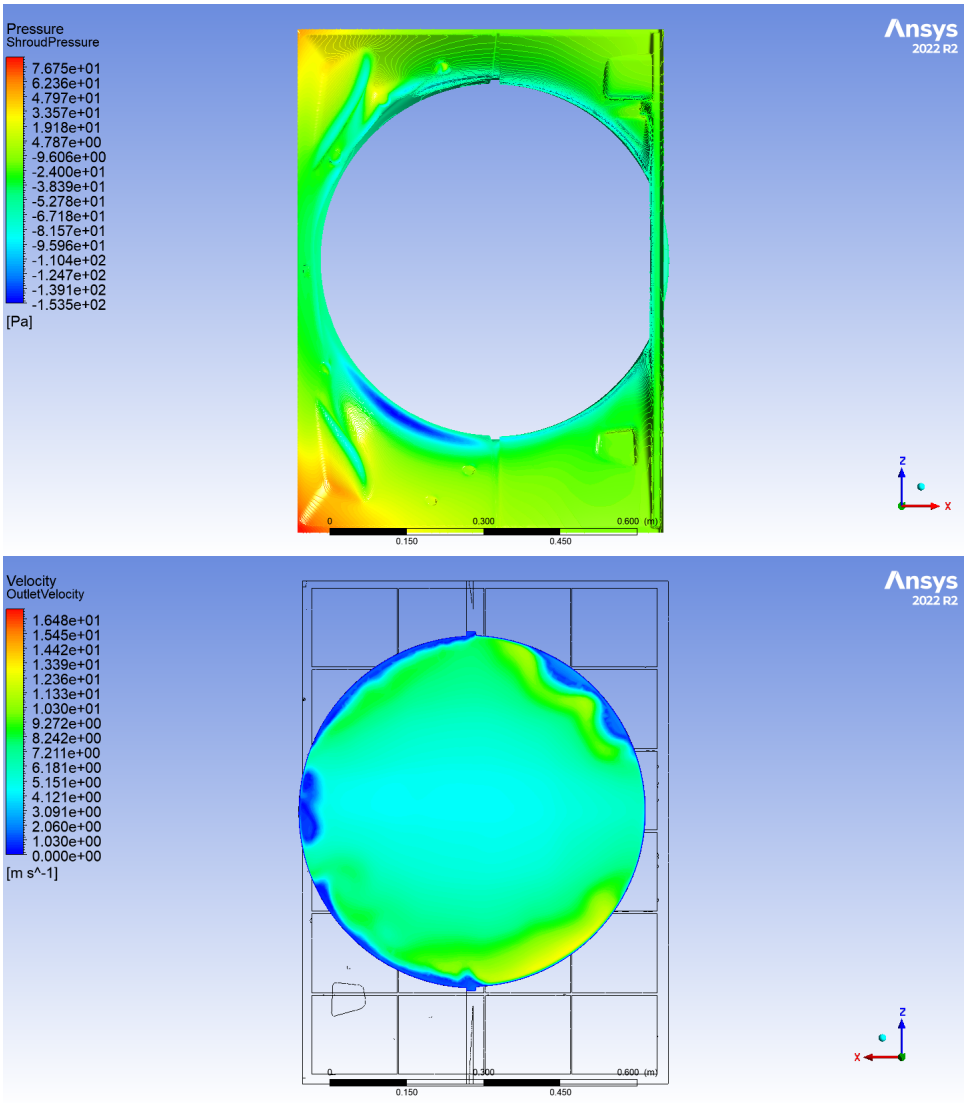

Figure 4.7: Stock Shroud CFD Results
(Above: Shroud Wall Pressure Contour, Below: Outlet Velocity Contour)

4.2.2 Modified Shroud Analysis

The geometry of the modified shroud was modeled based on the inlet and outlet dimensions of the current stock geometry. To attempt to create a more uniform flow and to reduce the effect of the shroud on the radiator, some other design considerations were imposed. This included smoothing the walls such that there were no areas with protruding geometries. Another consideration involved adding additional space from where the contours begin to change restrict the flow backwards towards the outlet. This was accomplished by adding an additional 20 mm of depth before the shroud begins to converge towards the outlet. The resulted geometry is shown in Figure 4.8.

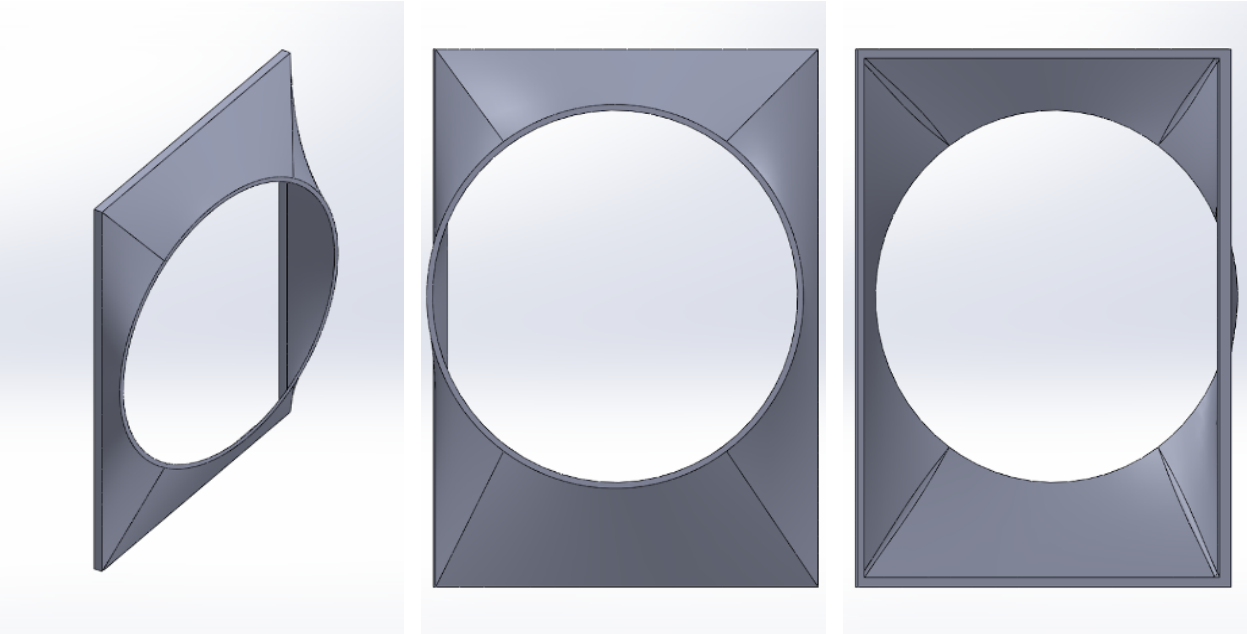

Figure 4.8: Modified Shroud CAD Model
(Left: Angled View, Middle: Inlet View, Right: Outlet View)

Following the same mesh process used previously the volume of the fluid domain could be modeled. The statistics of the mesh that was used for the modified shroud analysis can be seen in Table 4.2.

Table 4.2: Modified Shroud CFD Mesh Statistics

	Nodes	Faces	Cells
Boundary	218,504	70,184	-
Interior	1,031,570	1,514,640	274,339

Utilizing the imposed boundary conditions described previously, the CFD simulation was solved. The modeled pressure contours on the shroud and the velocity contour of the outlet can be seen in Figure 4.9.

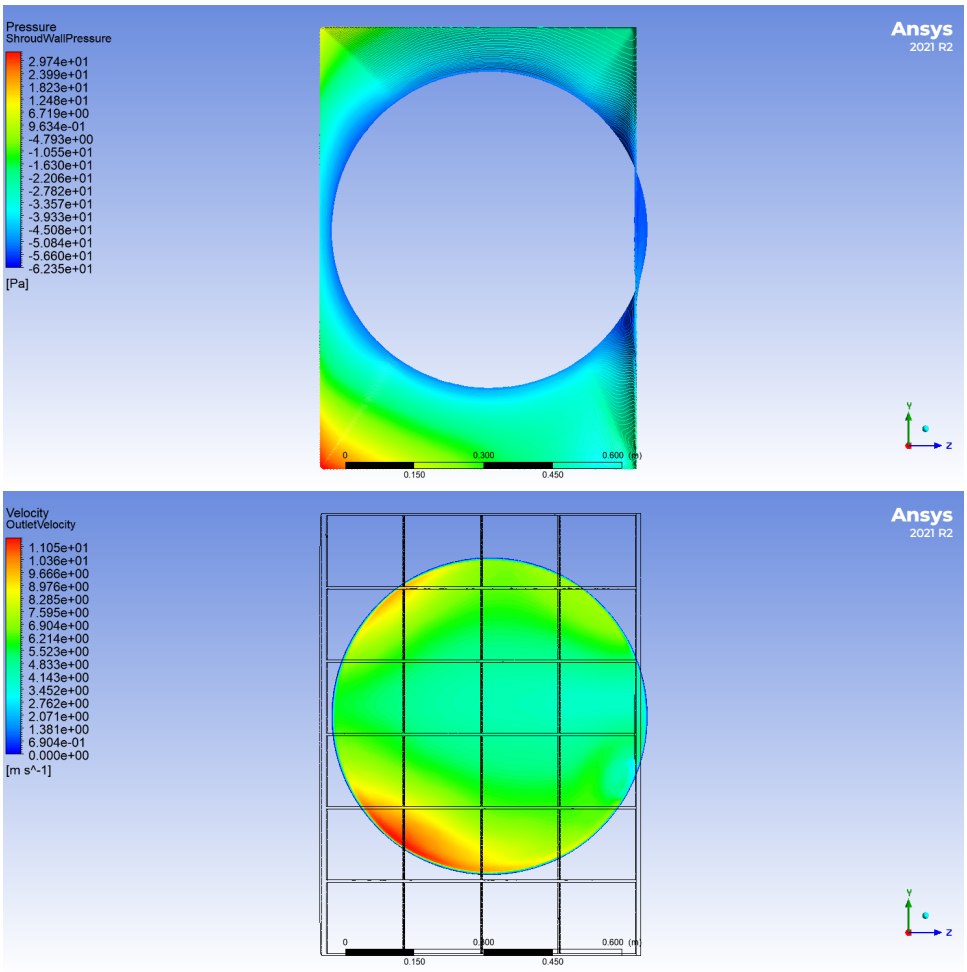

Figure 4.9: Modified Shroud CFD Results
(Above: Shroud Wall Pressure Contour, Below: Outlet Velocity Contour)

4.2.3 Shroud Comparison

The results of the two shroud geometries were compared to determine if the changes made to the modified shroud resulted in an improved performance. When comparing Figure 4.7 (above) and Figure 4.9 (above), the stock shroud can be seen to have an overall higher maximum pressure on the surface of the shroud. The modified shroud also appears to have a more gradual change of pressure when moving from the inlet towards the outlet of the shroud. The lower pressure on the surface of the modified shroud indicates that there is less restriction of the flow, suggesting the flow would pass through more easily relative to the stock shroud.

Looking at the velocity outlet contours of Figure 4.7 (below) and Figure 4.9 (below), the stock shroud is displayed to have an overall faster maximum measured velocity. However, when comparing the contours, the area of the modified shroud appeared to have more relatively high-velocity contours displayed in the outlet than that of the stock shroud. The stock shroud also shows relatively low-velocity contours around the edges of the circular outlet, where the opposite effect is seen in the modified shroud.

With a more, well-distributed wall pressure and outlet velocity, as well as a relatively lower wall pressure and relatively increased outlet velocity contours, the modified shroud appeared to perform as anticipated. The geometry of the redesigned modified shroud accomplished the objective of allowing for a less restricted airflow caused by the geometry of the shroud and was used to manufacture the shroud to be tested in the AFRD facility. This shroud was 3D printed with the material PA 2200, a white powder based polyamide.

5 Experimental Results

The TTA was utilized to record data in several experimental analyses. These experiments consisted of analyzing the flow through the radiator in three separate configurations: (i) radiator only, (ii) radiator with the stock shroud, and (iii) radiator with the modified shroud. All experiments were able to be accomplished utilizing the AFRD facility. This section examines the effects on the flow in all three configurations. Further, the analysis of how the modified shroud compared to the stock shroud is examined.

5.1 Experimental Set Up

The experiments were carried out with the use of the AFRD facility. Following the calibration of the TTA, the instrument was attached directly to the outlet face of the radiator with four bolts. This position, displayed in Figure 5.1 (Upper Right), allows for the TTA to measure the flow as it is exiting from the radiator. The radiator was mounted in the housing configuration and any remaining gaps or areas of concern were sealed using tape or foam to prevent air from entering the AFRD around the radiator or radiator housing. To ensure uniform inlet flow into the radiator, quarter-rounds were placed around the boundary of the inlet of the housing device to straighten the flow as it entered the radiator. This can be seen in the top view of the setup in Figure 5.1 (Upper Left).

The configuration described above details the experimental setup for measurements consisting of the radiator without a shroud attached. For the measurements consisting of either the stock shroud or modified shroud, the same experimental set up is utilized and the shroud would be fixed onto the outlet face of the radiator. The TTA remained between the radiator and shroud for measurements with minimal interference to the placement of the shroud. For both shrouds, any areas of potential air leakage are sealed with tape. The stock shroud is attached using bolts around the perimeter of the radiator and can be seen in Figure 5.1 (Lower Left). For the modified shroud, the shroud is supported on the exterior side of the shroud instead of the bolt holes to keep good contact with the radiator as seen in Figure 5.1 (Lower Right).

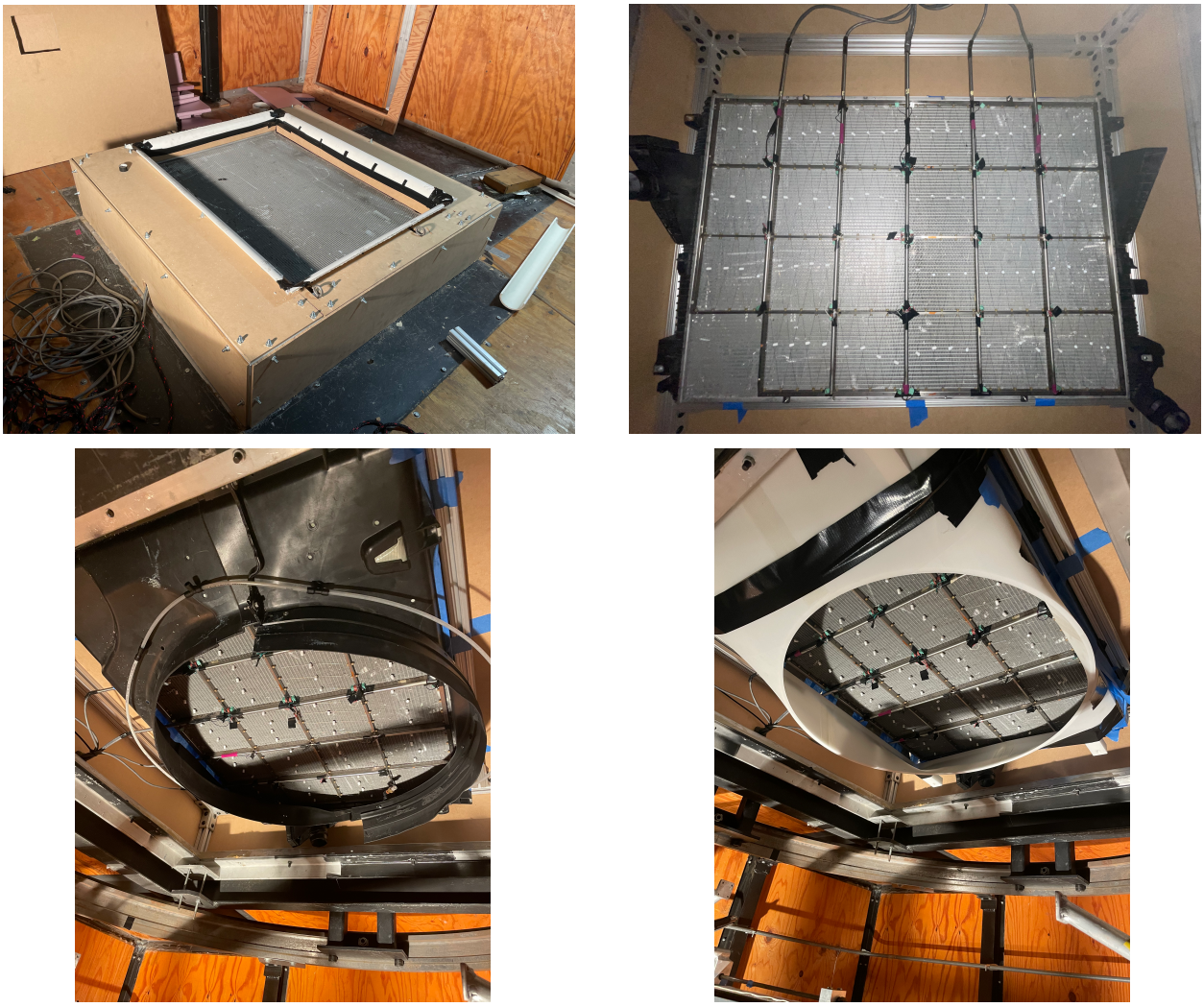

Figure 5.1: Experimental Set Up Configurations
(Upper Left: Top View for All Configurations, Upper Right: Radiator Only Configuration, Lower Left: Stock Shroud Configuration, Lower Right: Modified Shroud Configuration)

5.2 Radiator Analysis

The radiator was analyzed independently to evaluate the effect of the radiator on the flow through the system. The average recorded outlet velocity of the radiator ranged from 0.37 m/s - 7.00 m/s in fifteen velocity steps. However, due to the calibration range of the TTA at the time of the measurements, the velocities below 1.33 m/s could not be kept as these values are being extrapolated past the calibration range. This resulted in a total of thirteen velocity steps with an average recorded outlet velocity of 2.26 m/s - 7.00 m/s. These velocities were measured using the calibration constants located in Table A.1.

The areas of interest for the radiator analysis consisted of the flow distribution through the radiator and the loss coefficients of the radiator. The flow distribution of the radiator sets a

benchmark of how the radiator independently distributes the flow across the face of the radiator without the influence of a shroud. The causes of flow distribution can be caused by internal configurations in the radiator. Another source of flow distribution can come from possible damaged fins blocking passages through the radiator. Determining this benchmark allowed for analysis of how the shroud effects the radiator's independent flow distribution. Knowing the radiator's flow distribution and relationship between the pressure drop across the radiator versus the velocity exiting the radiator allows for the loss coefficients to be determined for each cell. The loss coefficients of the radiator are important to understanding the pressure drops across the face of the radiator. These pressure drops correlate to lower flow rates in the regions of the radiator.

5.2.1 Flow Distribution

The flow distribution was measured using the TTA placed at the outlet face of the radiator. The measurements resulted in thirteen velocity steps, with the average outlet velocity ranging from 2.26 m/s - 7.00 m/s as mentioned previously. Each velocity step recorded approximately sixteen measurements per cell. The equation used to determine percent difference of the velocity (5.1) is displayed below,

$$\%U_{cell} = \frac{U_{cell} - U_{avg}}{U_{avg}} \cdot 100\% \qquad (5.1)$$

where U is the measure of the fluid velocity and subscripts $cell$ and avg correspond to an individual cell measurement and the average velocity of all cells of the TTA in that velocity step, respectively. This calculation allows for the areas of the radiator that have relatively slower or faster flow to be visualized and compared to the overall average flow velocity.

For the measured velocity range, the velocity flow distribution and the velocity percent difference for the minimum, median, and maximum velocity steps can be seen in Figure 5.2, Figure 5.3, and Figure 5.4, respectively. The average velocity percent difference distribution across all velocity ranges can be seen in Figure 5.5. The complete set of measurements and full sized figures can be referred to in Appendix C, Figures C.1 – C.13.

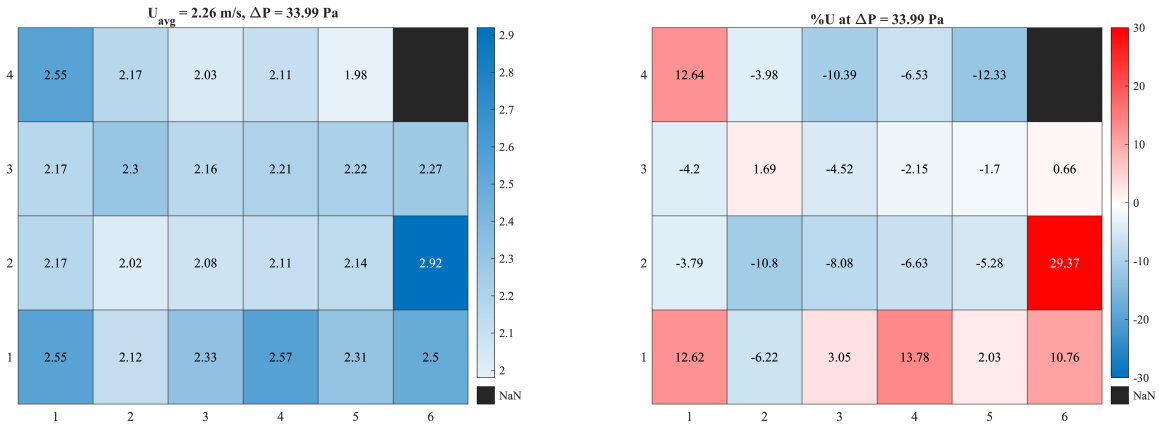

Figure 5.2: Radiator Flow Distribution at ΔP = 33.99 Pa

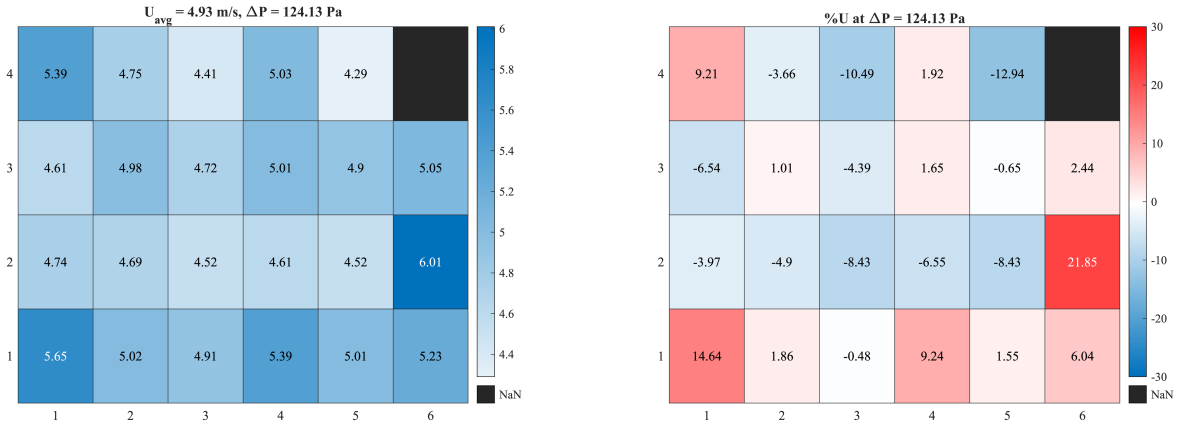

Figure 5.3: Radiator Flow Distribution at ΔP = 124.13 Pa

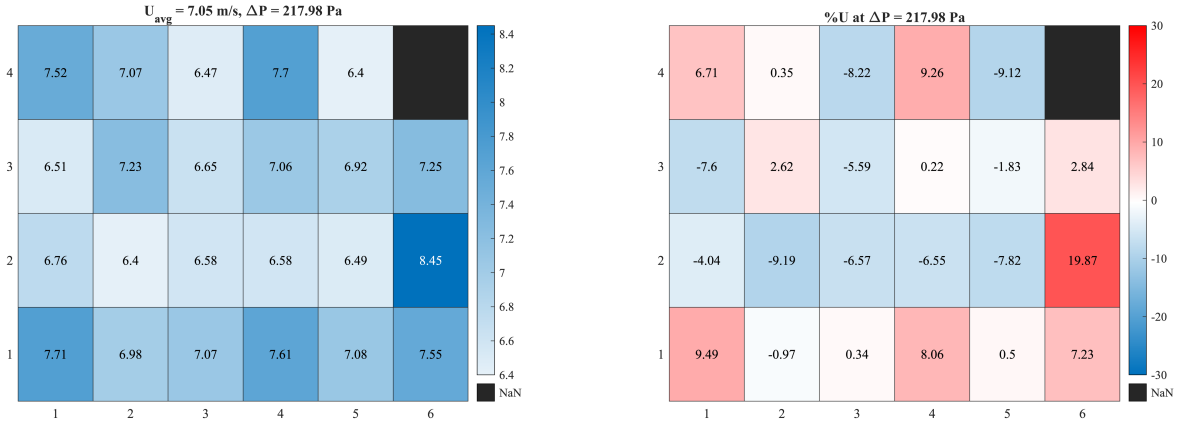

Figure 5.4: Radiator Flow Distribution at ΔP = 217.98 Pa

Figure 5.5: Average Velocity Percent Difference Distribution of Radiator

The flow distribution of the radiator began to become more homogeneous as the pressure difference and flow velocity increased. However, the areas of relatively higher and lower flow concentrations appeared to have remained consistent for all velocity steps. This indicates that the velocity profile exiting the radiator is likely unique to the performance of the radiator distributing the flow itself, not attributed to the changes of the flow velocity entering the radiator.

5.2.2 Loss Coefficients

The loss coefficients were calculated for each region of the radiator relating to the TTA

cells. The passages in which the air flows through the radiator are defined by the spaces between the fins, which can be seen in Figure 5.6. A closer view of the triangular cross-sectional geometry of the passages, as well as how the dimensions of the passages were measured, can be seen in Figure 5.6 (Below).

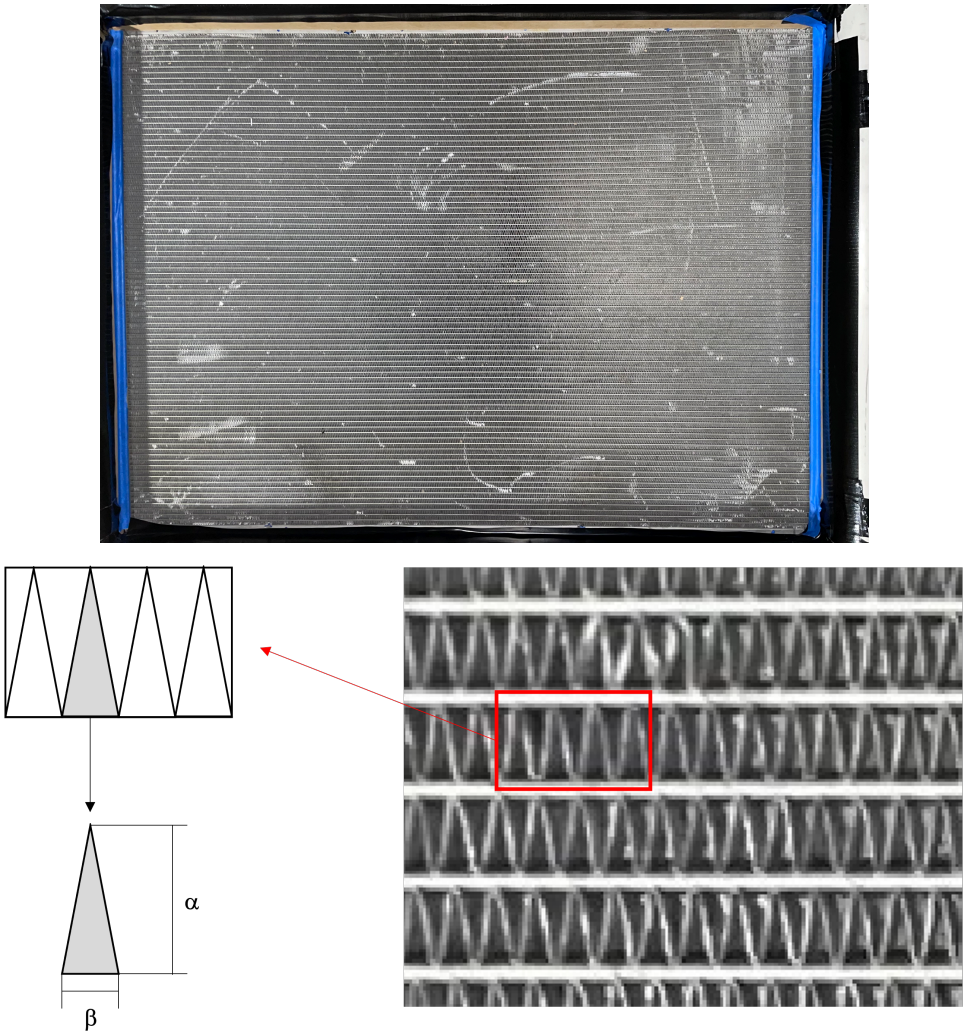

Figure 5.6: Radiator Fin Geometry
(Above: Radiator Face, Below: Fin Geometry)

A sample of ten fins were measured to determine the average passage dimensions, resulting an average height (α) of 6.06 mm and base (β) of 2.55 mm. These dimensions resulted in an average area of 7.72 mm^2 and perimeter of 14.93 mm.

To determine the loss coefficients through the radiator and shroud system, the measured flow velocity (TTA) and pressure differential (atmosphere to the upper receiver) are related. It is clear that pressure losses are present in the system due to the relatively lower flow velocity

measured by the TTA in the presence of the measured pressure differential. Additionally, it can be predicted that in the cross section of the radiator fins the flow would increase in Reynolds number when moving from the top of the triangle towards the wider portion of the triangle. It is known that the lower Reynolds number area is dominated by viscous shearing effects and scales by the flow velocity (U) and the relatively higher Reynolds number region is dominated by inertial effects (turbulent) and scales by the flow velocity squared (U^2). Therefore, the experimental data for the loss coefficients of each cell are represented as:

$$P_{atm} - P_{UR} = K_1 + K_2 U + K_3 U^2. \tag{5.2}$$

The dimensional homogeneity is ensured by the dimensions of the coefficients K_1, K_2, and K_3. The coefficient K_1 is non-physical and is used to smooth the fit of the experimental data.

The loss coefficients (K_2 and K_3) and zero-offset coefficient (K_1) are determined by fitting a curve to the recorded pressure differential and flow velocity data. This curve fitting technique used the least squares method. The coefficients that resulted from the fitted curve can be seen in Figure 5.7. These coefficients can be used to estimate the pressure drop across each cell of the TTA for a known velocity.

4	-12.91	-27.49	-21.03	-24.46	-32.99	
3	-19.02	-21.4	-15.64	-11.51	-13.14	-16.95
2	-16.6	12.42	-24.19	-23.25	-26.01	-19.86
1	2.052	-4.101	-30.44	-20.47	-15.1	-27.37
	1	2	3	4	5	6

4	73.86	156.1	138.3	163.1	192.2	
3	115.5	121	104	89.78	91.36	105.8
2	107	14.31	144.6	136.2	143.7	81.7
1	22.24	72.97	145.2	97.01	94.85	127.9
	1	2	3	4	5	6

4	4.234	2.335	3.948	1.104	2.2	
3	4.604	3.2	4.645	4.246	4.547	3.595
2	4.427	7.796	3.486	3.726	3.718	3.013
1	5.334	4.719	2.825	3.459	4.254	2.698
	1	2	3	4	5	6

Figure 5.7: Coefficients for the Radiator Pressure Losses
(Top: K1 zero-offset coefficient, Middle: K2 loss coefficient, Bottom: K3 loss coefficient)

5.3 Shroud Analysis

The TTA was utilized to determine the effect the shroud had on the flow through the radiator. The configuration of the shroud causes airflow to be restricted downstream and slows the through flow in certain regions of the the radiator. The analysis done on the shroud effects consisted of: (i) the effects both shrouds had relative to a radiator-only configuration and (ii) how the change in the geometry of the modified shroud can improve the flow through the radiator relative to the stock shroud.

To determine the effect the shroud has compared to a radiator-only configuration, the results of each shroud were compared independently to the radiator-only baseline results. The distribution of the velocity percent difference was determined for each configuration. This allowed for a comparison to the baseline of the radiator-only configuration. The stock shroud and the modified shroud were also statistically compared to each other to determine the effect of the geometry has on the flow.

The experimental measurements were recorded in a similar manner as the radiator analysis was done, with an attempt at remaining close to the pressure differences to mimic similar conditions as recorded with the radiator-only configuration for a more representative comparison.

5.3.1 Stock Shroud

Fifteen velocity steps were recorded for the stock shroud analysis. However, due to the calibration range of the TTA, fourteen velocity steps were able to be used for the analysis. These velocities ranged from 0.78 m/s - 3.04 m/s. The velocity steps and pressure differences recorded at each step are displayed in Table D.1. These velocities were measured using TTA with the calibration constants displayed in Table A.1.

The velocity percent difference distribution (as introduced for Figure 5.2Figure 5.4) for the minimum and maximum velocity steps recorded can be seen in Figure 5.8. The average velocity percent difference distribution can be seen in Figure 5.9. The entire results (and full sized figures) of the velocity percent difference for the stock shroud configuration can be seen in Figures D.1 – D.13.

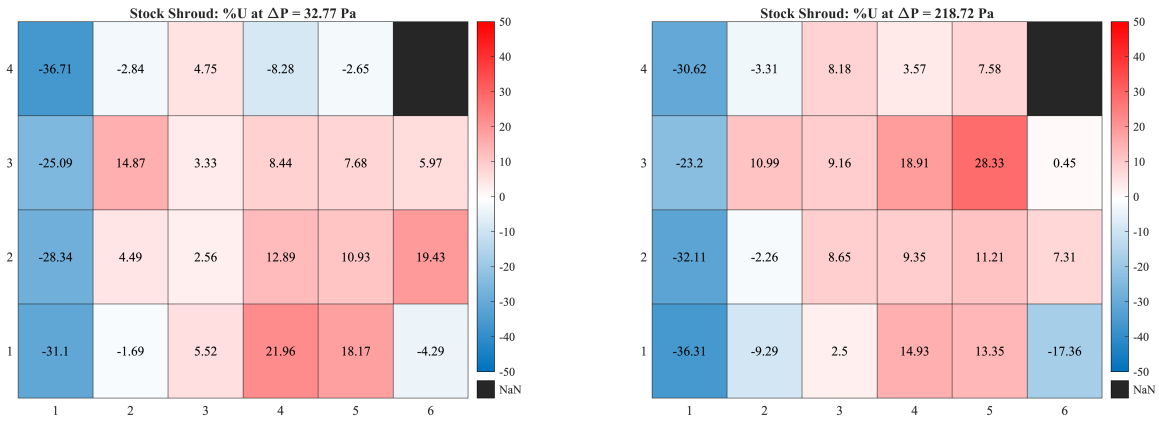

Figure 5.8: Stock Shroud Velocity Percent Difference
(Left: Minimum ΔP, Right: Maximum ΔP)

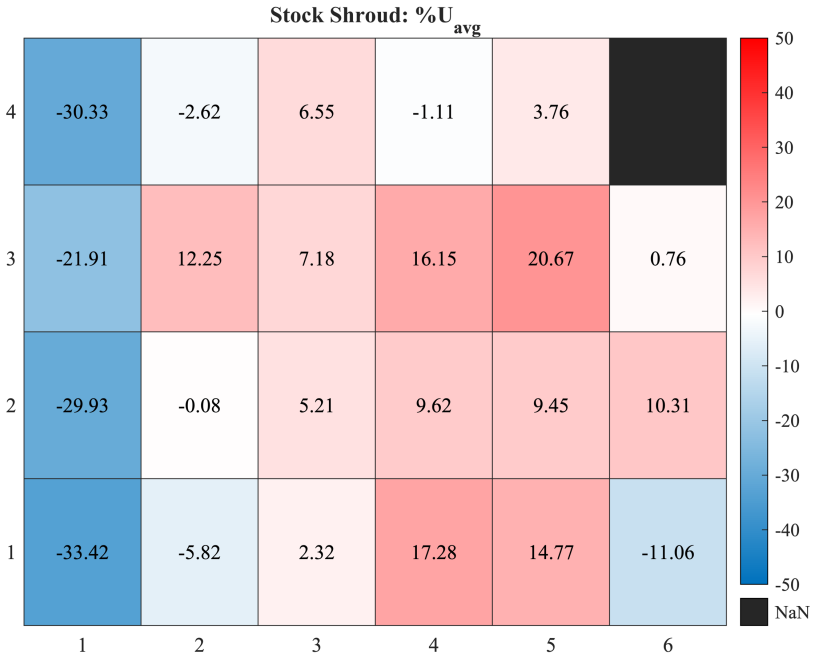

Figure 5.9: Average Velocity Percent Difference for Stock Shroud

The distribution of the flow with the stock shroud attached to the radiator displayed a relatively slower and more restricted region along the perimeter, specifically cells 1 through 4. This would be expected as that region of the shroud's geometry is closer to the outlet plane of the radiator, therefore restricting the flow and forcing the air to turn towards the center. The center portion of the flow, cells 6, 7, 10, 11, 14, 15, 18 and 19, flows relatively faster. This was also expected as the opening of the shroud's outlet overlaps this region, allowing air flow to pass more freely through the configuration. Although the severity of the percent differences fluctuate as the pressure

difference increases, the pattern of which cells are relatively slower and faster than the average flow velocity remains consistent.

5.3.2 Modified Shroud

Fifteen velocity steps were also recorded for the modified shroud analysis. Similarly to the stock shroud, only fourteen velocities were within the range of the TTA calibration. These velocities ranged from 0.77 - 2.98 m/s and are displayed in Table E.1 along with the recorded pressure differences. These velocities were measured using TTA with the calibration constants displayed in Table A.2. An issue with the TTA caused cells 9 through 12 to be unable to record data. This did not affect the other cells which could still be used for the analysis.

The velocity percent difference distribution for the minimum and maximum velocity steps recorded can be seen in Figure 5.10. The average velocity percent difference distribution can be seen in Figure 5.11. The entire results (and full sized figures) of the velocity percent difference for the stock shroud configuration can be seen in Figures E.1 – E.13.

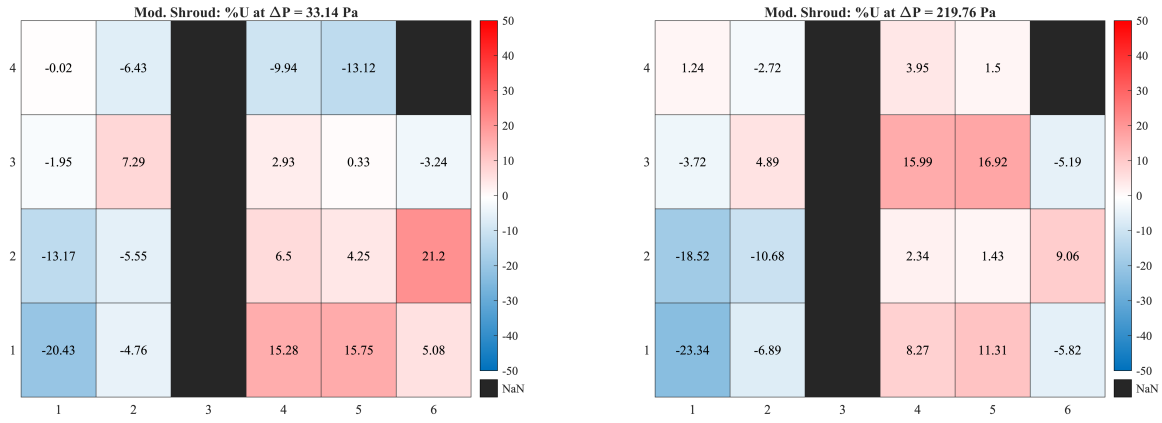

Figure 5.10: Modified Shroud Velocity Percent Difference
(Left: Minimum ΔP, Right: Maximum ΔP)

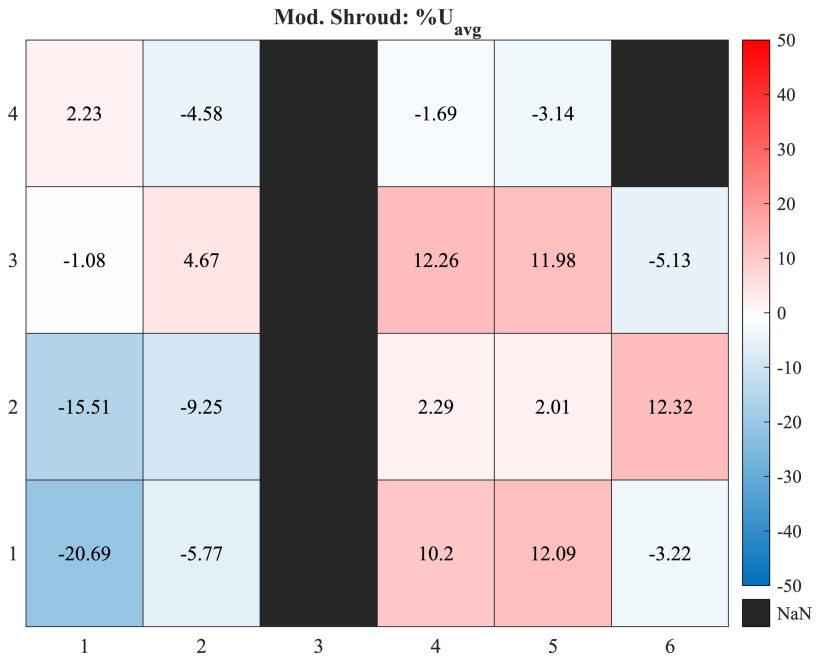

Figure 5.11: Average Velocity Percent Difference for Modified Shroud

Similarly to the stock shroud, the modified shroud experienced relatively slower flow in the first row of cells. However, the severity of the velocity percent differences appeared to lessen when moving to the modified shroud from the stock shroud. Specifically cells 3 and 4 appeared to improve significantly when compared to that of the stock shroud.

5.3.3 Shroud Comparison

The stock shroud and modified shroud had a significant impact on the flow through the radiator. The measurements from the three configurations allow for the impact of the shrouds on flow can be determined and compared. The average velocity percent difference across all pressure steps for the radiator only configuration, the radiator and stock shroud configuration, and the radiator and the modified shroud configuration can be seen in Figure 5.12.

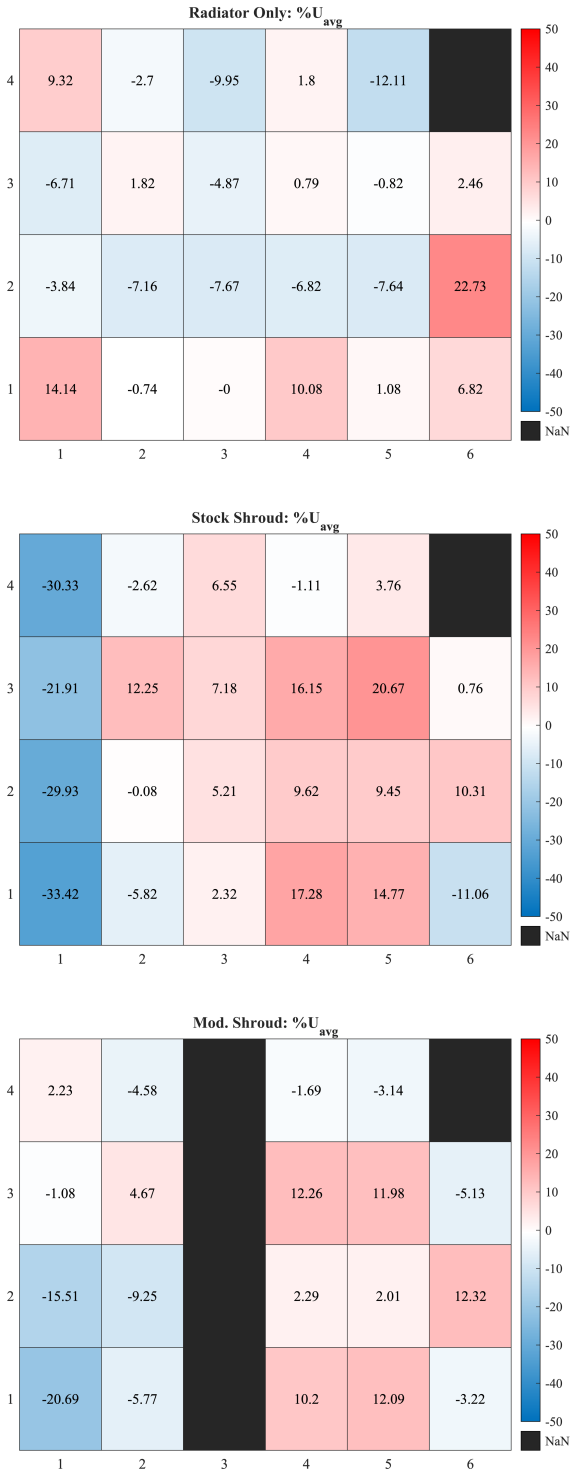

Figure 5.12: Average Velocity Percent Difference for All Configurations (Top: Radiator Only, Middle: Stock Shroud, Bottom: Modified Shroud)

The average velocity percent difference for the radiator only configuration can be seen to have a relatively homogeneous flow distribution, with some perimeter cells above the average velocity and some middle cells below the average velocity. Both the stock shroud and modified shroud displayed a similar pattern in which the perimeter cells, specifically cells 1, 2, 3, and 4, experience below average velocity. Also, the middle cells, without being able to definitively confirm for the modified shroud, experienced a relatively higher velocity than the average.

The change in the velocity percent difference from the radiator to either to stock or modified shroud can be seen in Figure *5.13* and Figure 5.14, which are at the minimum and maximum pressure differences. This was calculated as shown in equation (5.3).

$$\Delta\%U = \%U_{Shroud} - \%U_{Rad} \quad (5.3)$$

The average change in velocity percent difference for all velocity steps can be seen in Figure 5.15.

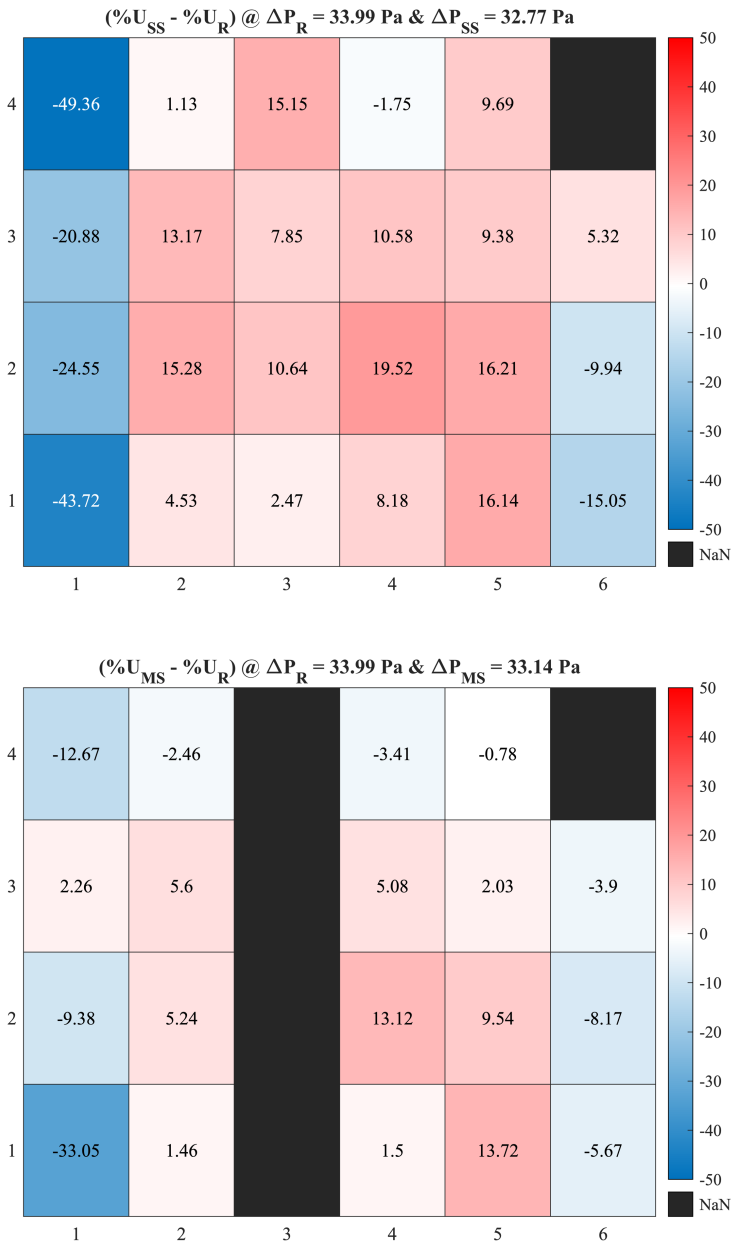

Figure 5.13: Shroud Velocity Percent Difference from Radiator at minimum ΔP
(Above: Stock Shroud Difference from Radiator, Below: Modified Shroud Difference from Radiator)

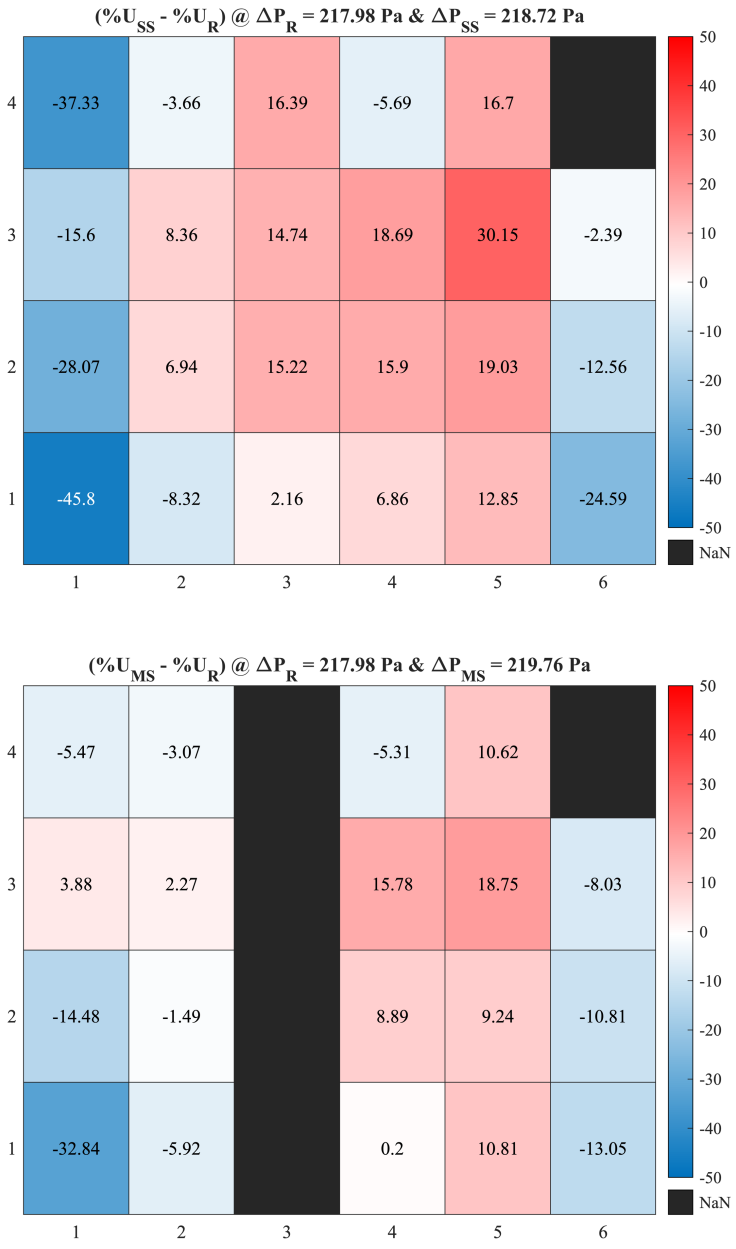

Figure 5.14: Shroud Velocity Percent Difference from Radiator at Maximum ΔP
(Above: Stock Shroud Difference from Radiator, Below: Modified Shroud Difference from Radiator)

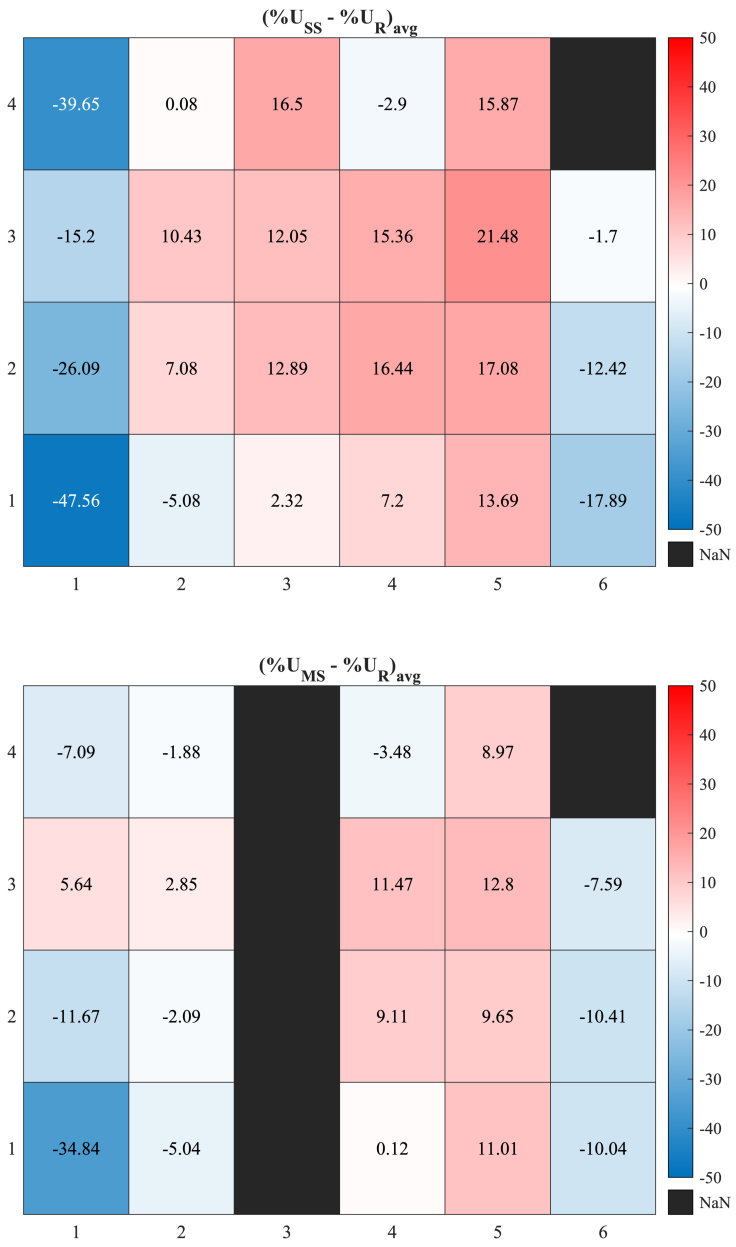

Figure 5.15: Shroud Average Velocity Percent Difference from Radiator
(Above: Stock Shroud Difference from Radiator, Below: Modified Shroud Difference from Radiator)

The stock shroud and modified shroud behaved in a similar manner as far as most of the perimeter cells decreasing the flow and the inner core cells increasing the flow. However, the severity of the changes decrease in the modified shroud compared to the stock shroud. This results in a more homogeneous flow distribution in the modified shroud than the stock shroud. To compare the difference of homogeneity of the flow distribution between the stock and modified shroud, the

standard deviation of the absolute values of the velocity percent difference for all cells at each velocity step was calculated. The absolute value was chosen such that the deviation from the mean did not benefit for the deviation being both negative and positive. This standard deviation for each shroud is displayed in Figure 5.16.

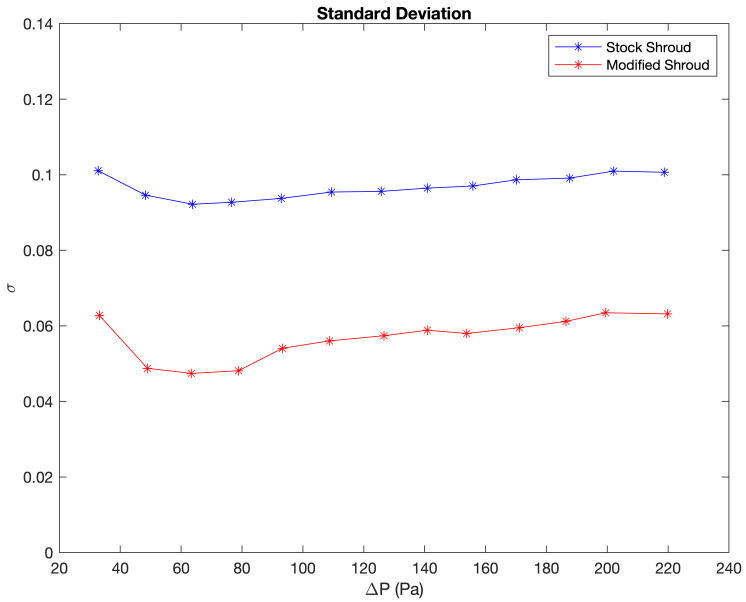

Figure 5.16: Absolute Value of the Standard Deviation of Velocity Percent Difference

The stock shroud has a higher amount of deviation from the mean flow velocity throughout the range of pressure differences which results in a high velocity flow regions through the radiator. This indicated that the modified shroud performs better at allowing the flow to become more homogeneous than the stock shroud.

Another flow characteristic that was explored was the flow rate difference between the two shroud geometries. The flow rate is determined by (5.4),

$$Q = U \cdot A, \tag{5.4}$$

where U is the velocity of the fluid flow and A is the area in which the flow is passing through. For these experimental analyses, the area remains constant for all three configurations. Due to the fixed area, the flow rate can be directly represented by the velocity and equation (5.4) is modified and becomes equation (5.5).

$$Q" = \frac{Q}{A} = \frac{U \cdot A}{A} = U$$

(5.5)

The flow rate of the stock shroud and modified shroud relative to the radiator only configuration can be seen in Figure 5.17, where the flow rate of the radiator only configuration is plotted as reference.

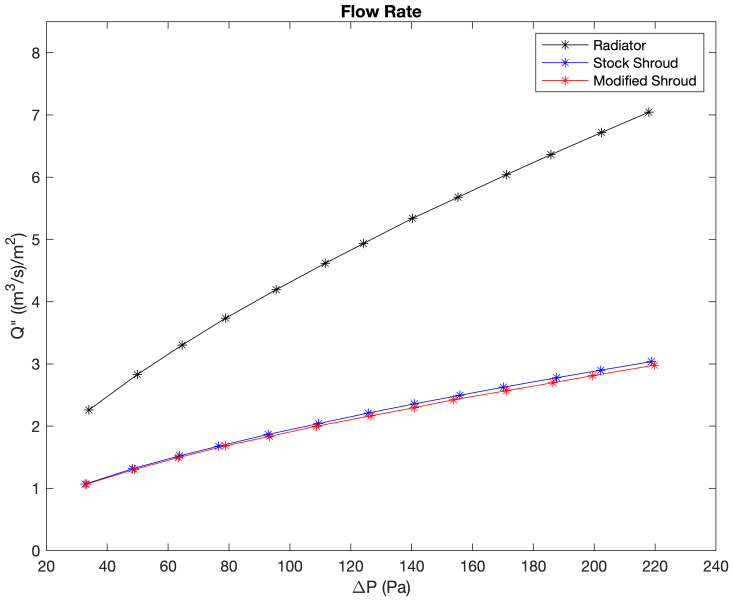

Figure 5.17: Flow Rate of Radiator, Stock Shroud, and Modified Shroud

This plot shows that both shrouds significantly impact the flow rate through the radiator. Both shrouds have a similar overall impact relative to the radiator only configuration. A closer look at only the shrouds can be seen in Figure 5.18.

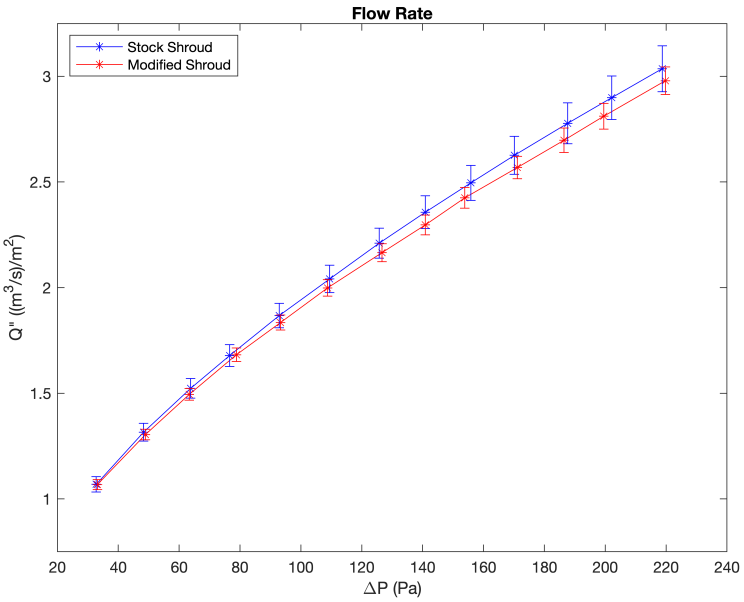

Figure 5.18: Flow Rate of Stock and Modified Shroud

The plot in Figure 5.18 shows the calculated standard error as well, showing that the flow rate for both shrouds tend to overlap each other with the error bars present. The standard error was determined using the following equation (5.6),

$$SE = \frac{\sigma}{\sqrt{n}}, \tag{5.6}$$

where SE is the standard error, σ is the standard deviation, and n is the sample size. With this being determined, the more efficient shroud design in terms of flow rate between the shrouds cannot be definitively determined as they perform in such a similar behavior.

Lastly, a statistical approach was taken in order to further look into the flow distribution between the stock shroud and modified shroud. The skewness and kurtosis of the velocity percent difference data was analyzed. The skewness represents if the data tends to be on the higher or lower side of the distribution, where a value of zero is symmetrically distributed, above zero is more data on the higher side, and below zero is more data on the lower side. For the use of skewness in this analysis, a positive value of skewness shows the velocity percent difference tends to be higher values or a negative value shows the data tends to be lower. The kurtosis represents if the data is grouped together around the mean or is more distributed, where the value of three

matches that of a normal distribution kurtosis value. For the use of kurtosis in this analysis, a higher value could suggest a more homogeneous flow and a lower value could suggest the opposite.

The skewness and kurtosis of the velocity percent differences for both the stock shroud and modified shroud can be seen in Figure 5.19 and Figure 5.20, respectively.

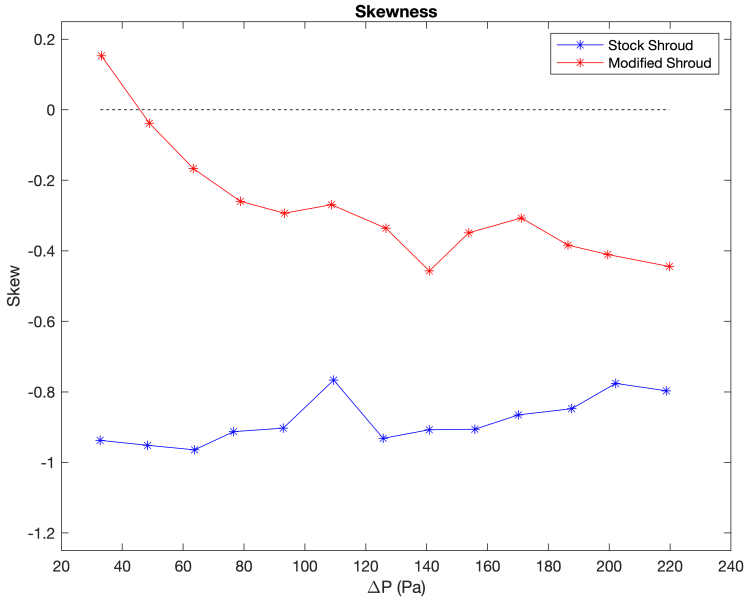

Figure 5.19: Skewness of Stock and Modified Shroud

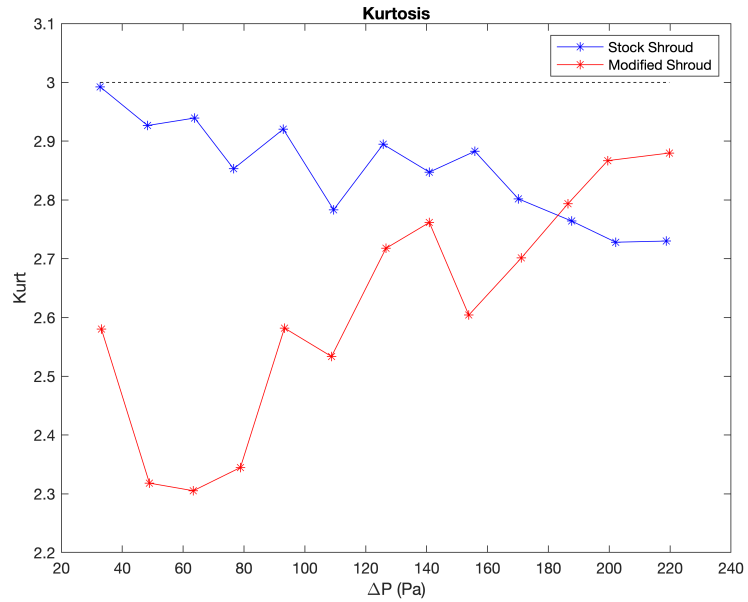

Figure 5.20: Kurtosis of Stock and Modified Shroud

The skewness of both shrouds can be seen relative to a value of zero, the dashed line in

Figure 5.19. For reference, Figure 5.21 displays the difference of negative (right), zero, and positive (left) skewness. As can be inferred, the amount of skew in the stock shroud remains consistently right skewed. The modified shroud begins relatively close to no skew, then trends to a right skew behavior similar to the stock shroud. However, the modified shroud remains significantly less, roughly 50%, than that of the stock shroud as the pressure difference and flow velocity steps increased. These skewness values indicate that mean of the data is lower than that of the median for both shrouds.

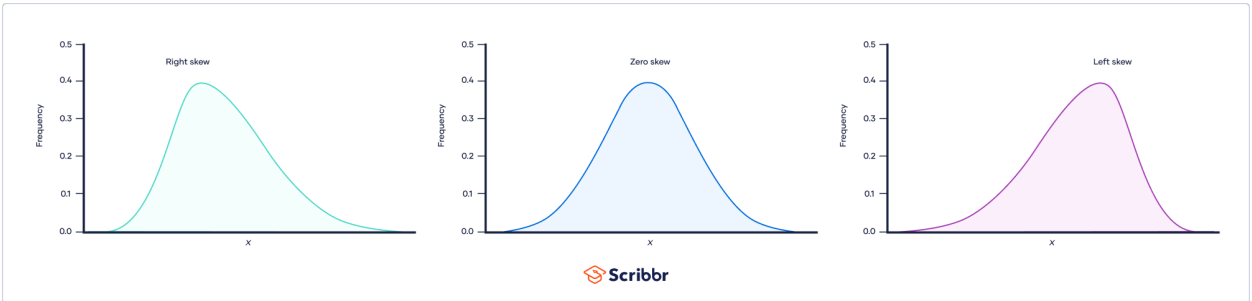

Figure 5.21: Skewness Reference (www.scribber.com)

The kurtosis of both shrouds can be seen relative to a value of three, the dashed line in Figure 5.20 which indicates no excess kurtosis, similarly to a normally distributed data set. For reference, Figure 5.22 displays the difference between high (leptokurtic), moderate (mesokurtic), and low (platykurtic) kurtosis data sets. The stock shroud's kurtosis measurements decrease as the pressure difference and flow velocity increases. This indicates that the data moves more towards a lower trend meaning the data set is more grouped around the mean value with less outliers. The modified shroud acts in the opposite manner, starting a relatively low kurtosis value and increases with the increased pressure difference and flow velocity steps.

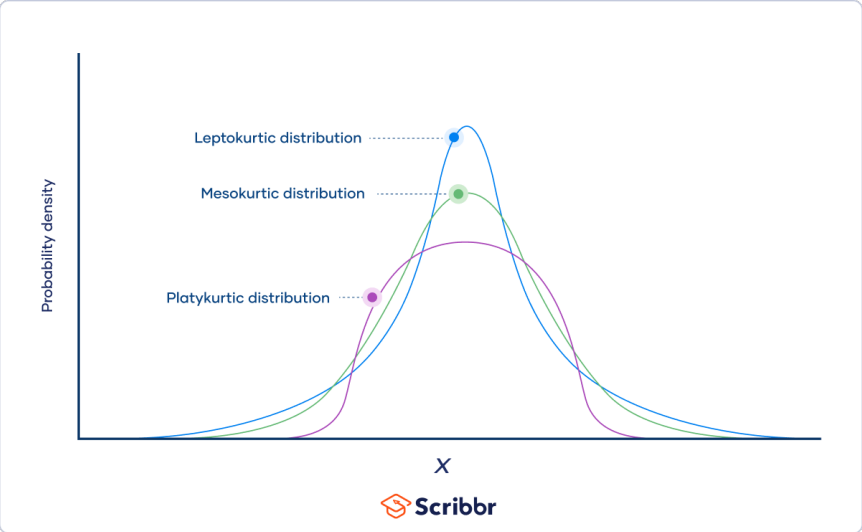

Figure 5.22: Kurtosis Reference (www.scribbr.com)

6 Conclusion

The TTA was utilized in determining and testing the effects of a shroud's geometry on the flow through the vehicular radiator system. This effort was built off of previous works that introduced the concept of the TTA, fabricated the present day TTA configuration, and demonstrated the use of the TTA in similar experimental environments.

A redesigned shroud for objective of pursuing an improved thermal energy management system in automotive applications was explored with the use of the TTA. The design of the shroud was able to be achieved through the use of numerical modelling of the system to confirm a preliminary design. The numerical model applied a measured velocity distribution previously measured in order to simulate the incoming flow to the shroud design. The currently used stock shroud design was compared to the modified shroud design. The results inferred that the modified shroud allows for a better flow distribution to occur through the shroud and relieve pressure on the shroud's surface, indicating an ease of flow. This effort allowed for the modified shroud to be manufactured utilizing a 3D printer.

To perform the analysis of newly designed shroud, the TTA was first applied to determine the velocity distribution of the radiator independent of an attached shroud. This distribution was measured for an average flow velocity range of 2.26 - 7.00 m/s. These distribution measurements provided a baseline to compare how the shroud effects the flow independently of how the radiator may affect the flow. Further, the analysis of the radiator-only configuration allowed for loss coefficients to be determined for the radiator which can be useful when looking at specific areas of cooling to improve on for the radiator.

Following the experiments consisting of the radiator-only configuration, the stock shroud and modified shrouds were able to be analyzed for their effects to the flow through the system. The stock shroud was measured at an average flow velocity range of 0.78 - 3.04 m/s. The stock shroud displayed a consistent pattern of restricting flow of cells 1 - 4 and an increased velocity in the cells in the core of the grid. The modified shroud was tested similarly, with an average flow velocity range of 0.77 - 2.98 m/s. It is important to note that the third row, cells 9 - 12, were unable to record measurements for the modified shroud testing. The modified shroud displayed a similar pattern to that of the stock shroud, however the severity in which the distribution deviated from the mean velocity of each step decreased significantly. A further look determined that no definitive conclusions could be drawn from the flow rate of the two shroud geometries. However, the

deviation of the flow can be determined to become more homogeneous with the modified shroud when compared to the stock shroud.

This research has shown that the geometry of the shroud has a significant effect on the flow through the radiator. The effort to improve the shroud's geometry (keeping the inlet and outlet dimensions the same) involves: i) adding more space for flow to enter the shroud and ii) smoothing of the contours of the shroud from inlet to outlet to improve the distribution of the airflow through the radiator. Future improvements could potentially lead to an improvement of flow rate and other important characteristics of the thermal energy management design. These improvements may consist of a further increase in allowing the flow to enter the shroud unobstructed. Another improvement may look to improve the geometry of the shroud's contours further.

BIBLIOGRAPHY

[1] Azar, Kaveh. *Thermal measurements in electronics cooling*. CRC press, 1997.

[2] JF Foss, JA Peabody, MJ Norconk, and AR Lawrenz. Ambient temperature and free stream turbulence effects on the thermal transient anemometer. *Measurements Science and Technology,* 13(9):2519, 2006.

[3] JF Foss, JK Schwannecke, AR Lawrenz, MW Mets, SC Treat, and MD Dusel. The thermal transient anemometer. *Measurements Science and Technology*, 15(11):2248, 2004.

[4] James Leung, *Nonuniform Flow over a Thermal Transient Anemometer*. Michigan State University, 2018.

[5] Sarah Plant. *The Performance of a Thermal Transient Anemometer (TTA) for Nonuniform Velocity Measurements*. Michigan State University, 2020.

APPENDIX A: Calibration Results

A.1 Calibration with Pressure Transducer

Table A.1: Calibration Constants of TTA with Pressure Transducer

Cell No.	**4**	**8**	**12**	**16**	**20**	**NaN**
A	0.5717	1.1074	1.1494	2.8585	1.9813	X
B	0.7183	0.5137	0.5162	0.2458	0.3508	X
C	1.3298	0.7212	0.6741	-1.0503	-0.1822	X
R^2	0.9989	0.9996	0.9977	0.998	0.9998	X
Cell No.	**3**	**7**	**11**	**15**	**19**	**23**
A	0.8697	0.7154	0.8964	0.7504	0.8549	0.9881
B	0.5868	0.6328	0.5728	0.6213	0.5789	0.5436
C	1.0257	1.1606	1.0044	1.1585	1.0253	0.8413
R^2	0.9996	0.9986	0.9997	0.9999	0.9997	0.9996
Cell No.	**2**	**6**	**10**	**14**	**18**	**22**
A	0.813	0.4777	0.931	1.0714	1.1648	0.816
B	0.6065	0.7582	0.5647	0.5214	0.4982	0.5662
C	1.1127	1.4826	0.9517	0.7745	0.6726	0.9892
R^2	0.9997	0.9966	0.9995	0.9997	0.9986	0.9995
Cell No.	**1**	**5**	**9**	**13**	**17**	**21**
A	0.562	1.0038	1.2179	0.9542	0.8715	1.0158
B	0.7193	0.5032	0.4794	0.5431	0.5801	0.5247
C	1.3544	0.8221	0.519	0.7927	0.9856	0.9892
R^2	0.9984	0.9975	0.9975	0.9979	0.999	0.9996

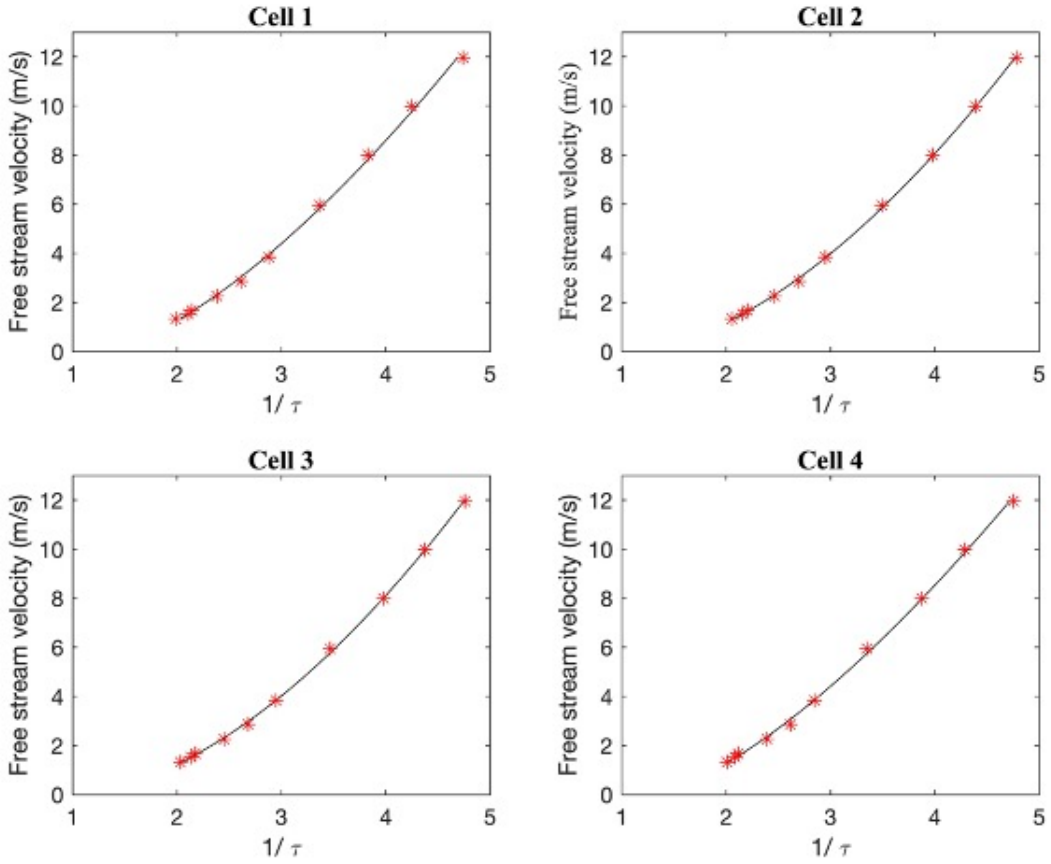

Figure A.1: Cell 1 - 4 Calibration Curves - Pressure Transducer

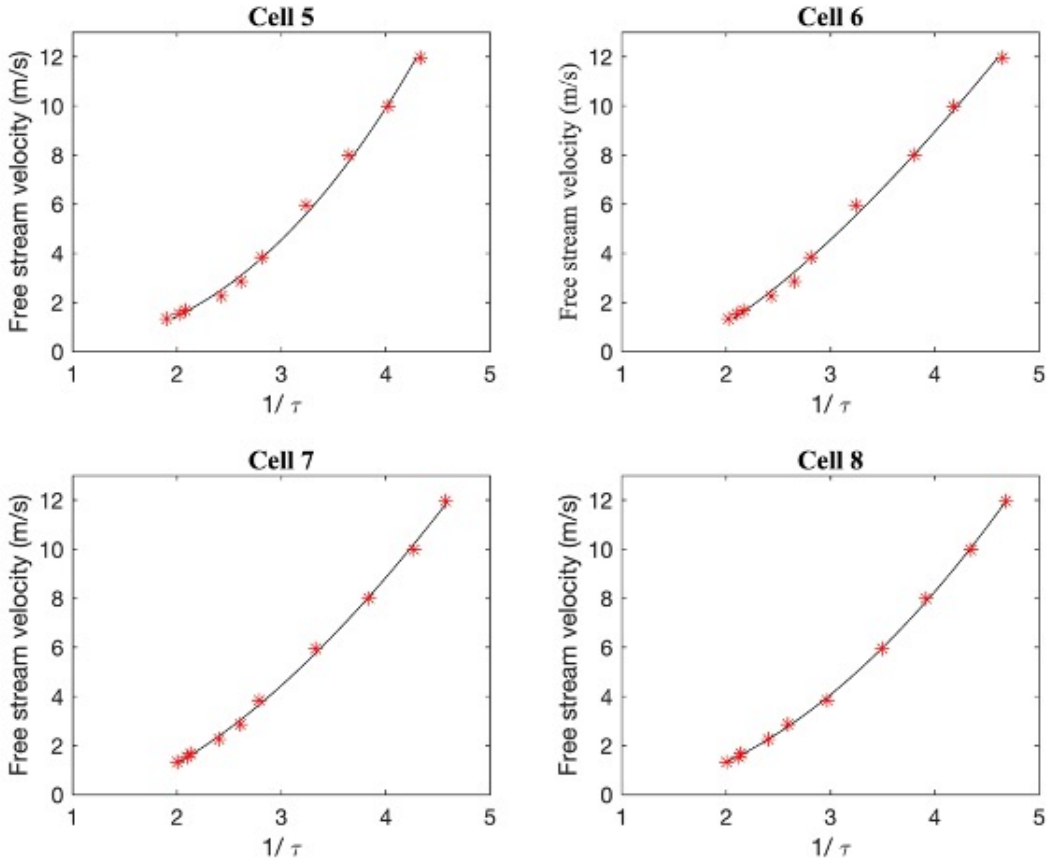

Figure A.2: Cell 5 - 9 Calibration Curves - Pressure Transducer

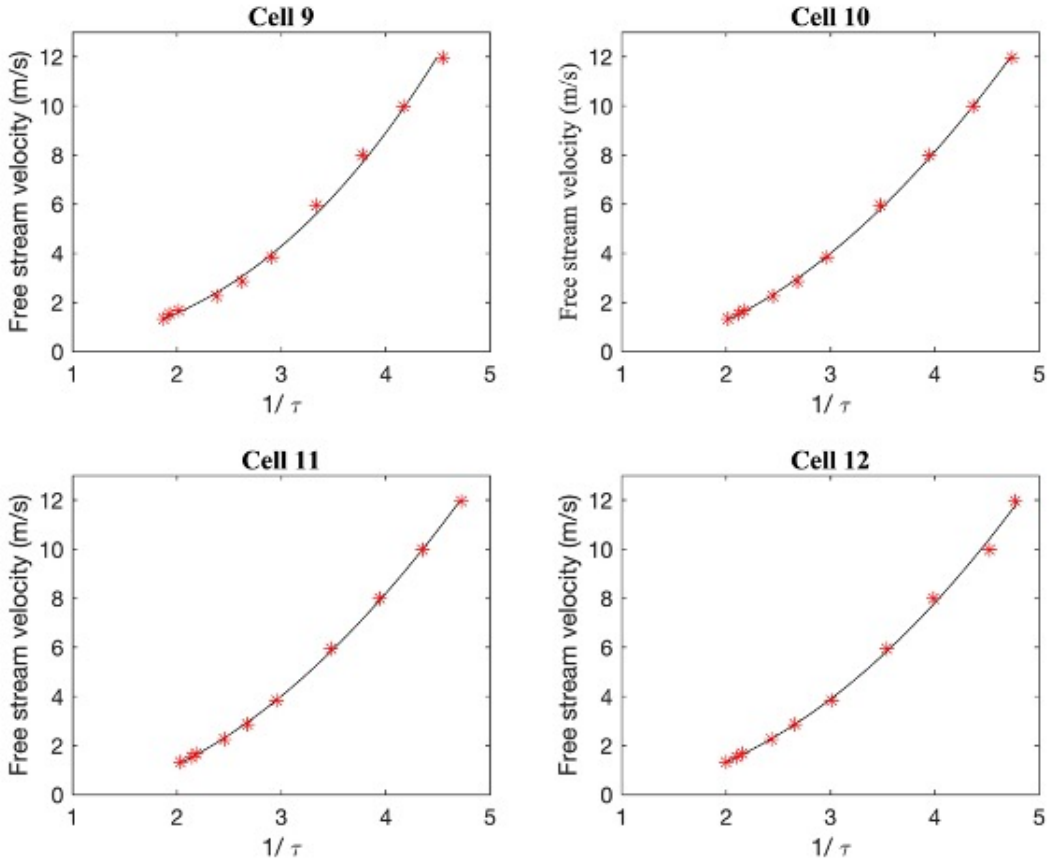

Figure A.3: Cell 9 - 12 Calibration Curves - Pressure Transducer

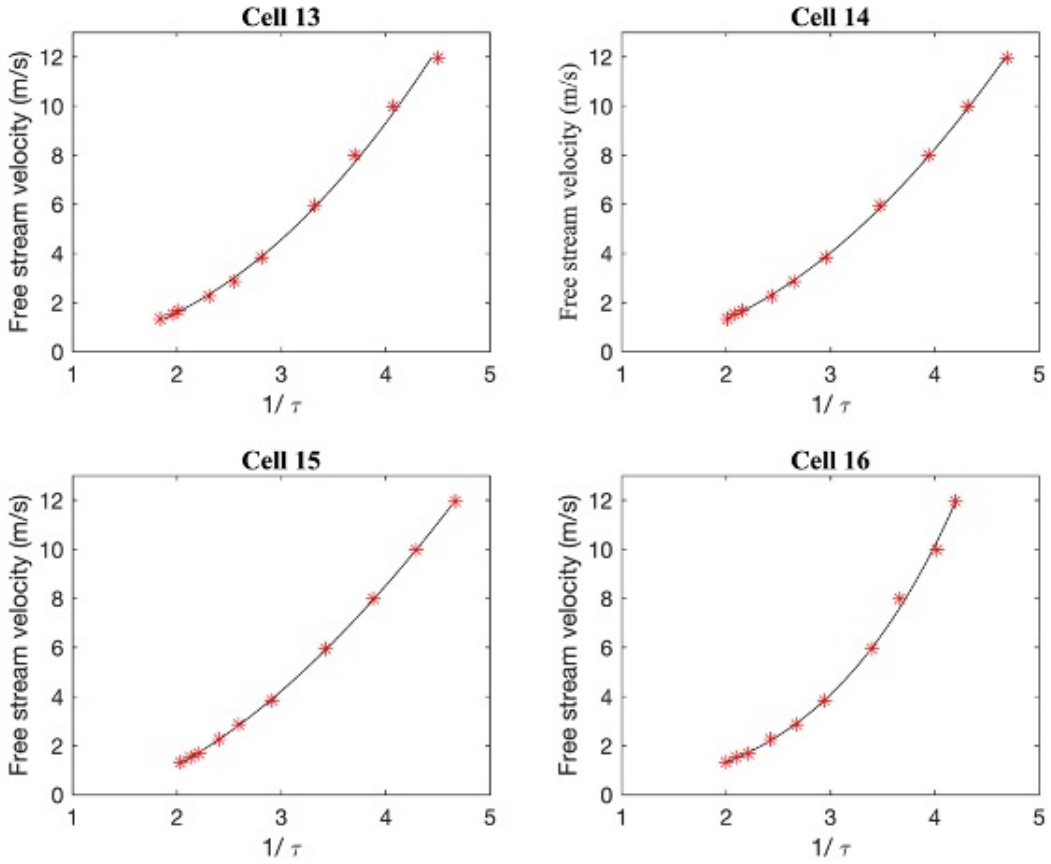

Figure A.4: Cell 13 - 16 Calibration Curves - Pressure Transducer

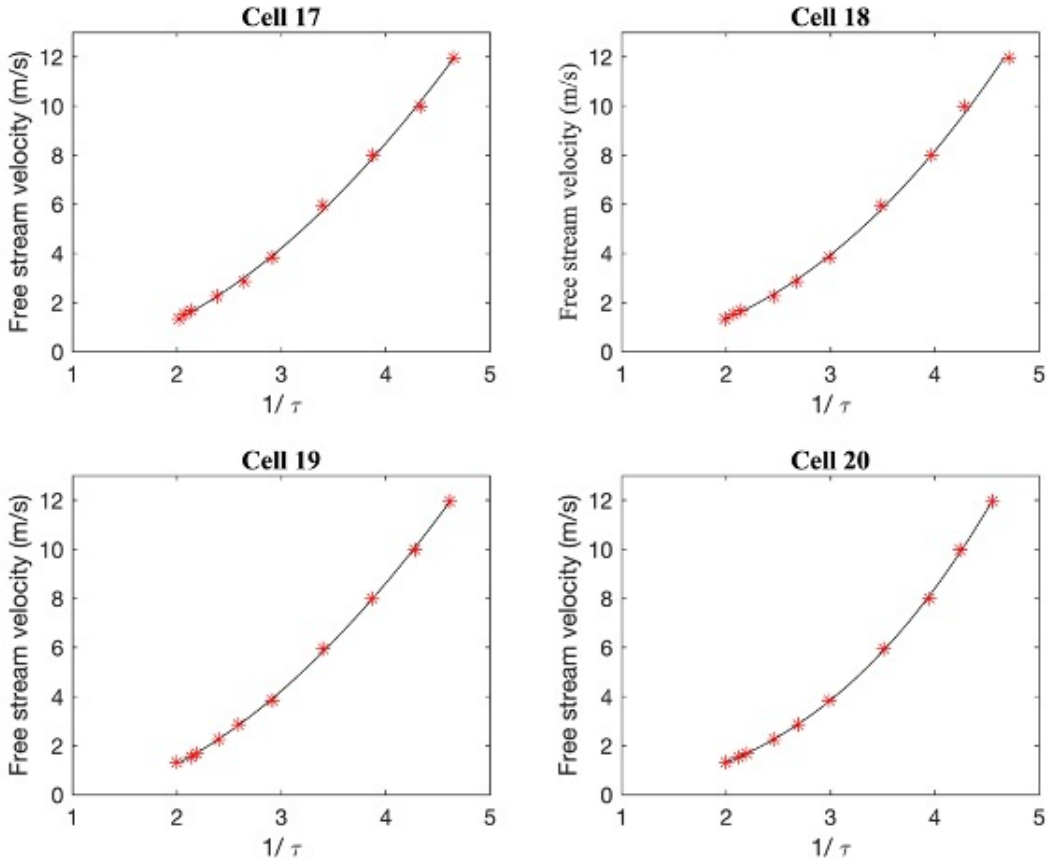

Figure A.5: Cell 17 - 20 Calibration Curves - Pressure Transducer

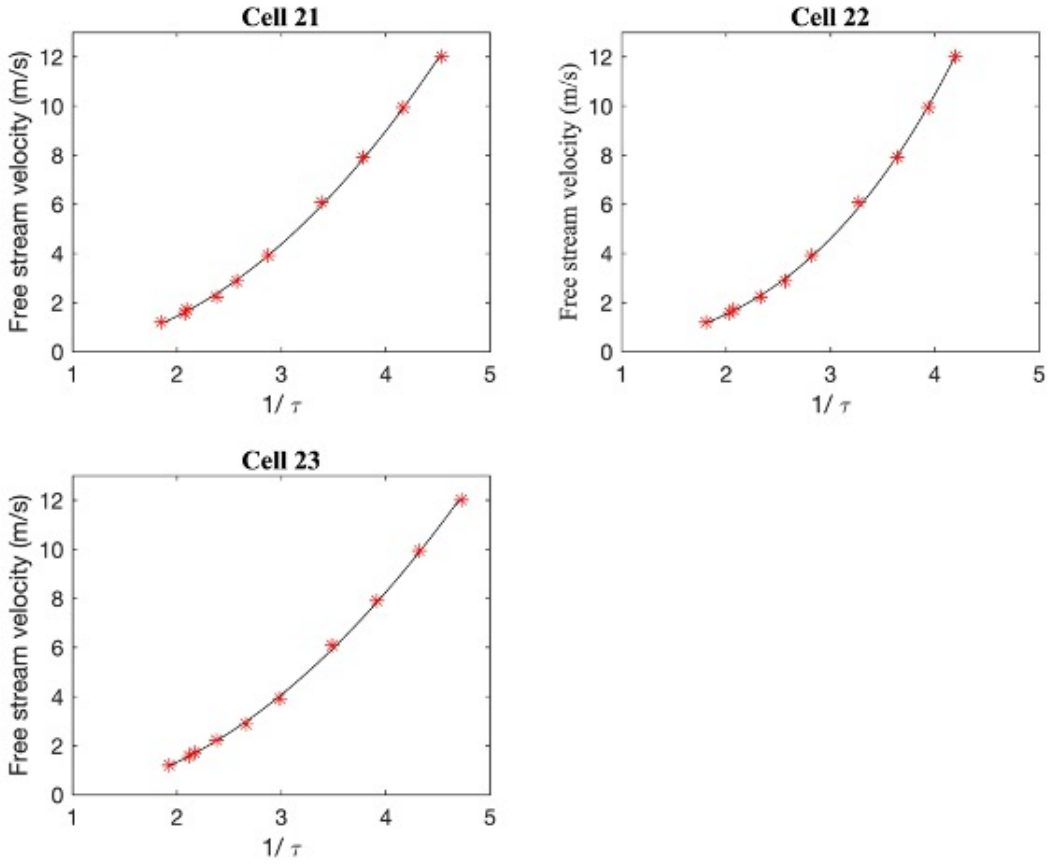

Figure A.6: Cell 21 - 23 Calibration Curves - Pressure Transducer

A.2 Calibration with Pressure Transducer

Table A.2 Calibration Constants of TTA with Fiber-film Probe

Cell No.	**4**	**8**	**12**	**16**	**20**	**NaN**
A	1.0633	1.5051	1.6586	1.4697	1.3623	X
B	0.6099	0.5254	0.5046	0.5384	0.5533	X
C	1.1096	0.7679	0.639	0.856	0.9523	X
R^2	0.9995	0.9992	0.9998	0.9996	0.9981	X
Cell	**3**	**7**	**11**	**15**	**19**	**23**
A	1.1542	1.6682	1.5991	1.1546	1.0702	1.464
B	0.5861	0.4625	0.499	0.5972	0.6106	0.5347
C	1.0109	0.5138	0.678	1.0991	1.1612	0.7549
R^2	0.9999	0.9968	0.9997	0.999	0.9993	0.9999
Cell	**2**	**6**	**10**	**14**	**18**	**22**
A	1.6091	1.6377	1.6303	1.7177	1.6548	1.6009
B	0.4909	0.4815	0.4958	0.4822	0.4935	0.4844
C	0.6235	0.5684	0.5949	0.4707	0.512	0.4926
R^2	0.9998	0.9997	0.9997	0.9993	0.9997	0.9998
Cell	**1**	**5**	**9**	**13**	**17**	**21**
A	1.7967	1.6183	1.6252	1.3985	1.314	1.7385
B	0.4706	0.481	0.4954	0.5589	0.5536	0.4631
C	0.4827	0.5405	0.5418	0.6836	0.745	0.3601
R^2	0.9997	0.9997	0.9995	0.9984	0.9994	0.9998

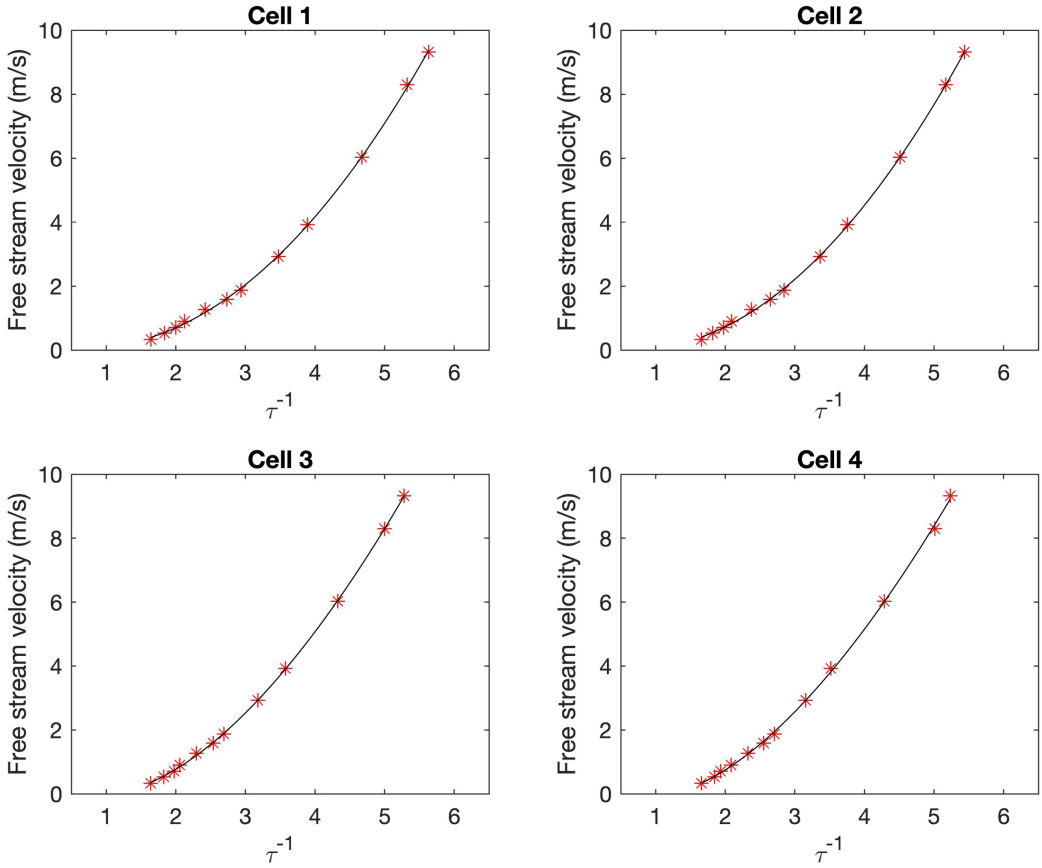

Figure A.7: Cell 1 - 4 Calibration Curves - Fiber-film Probe

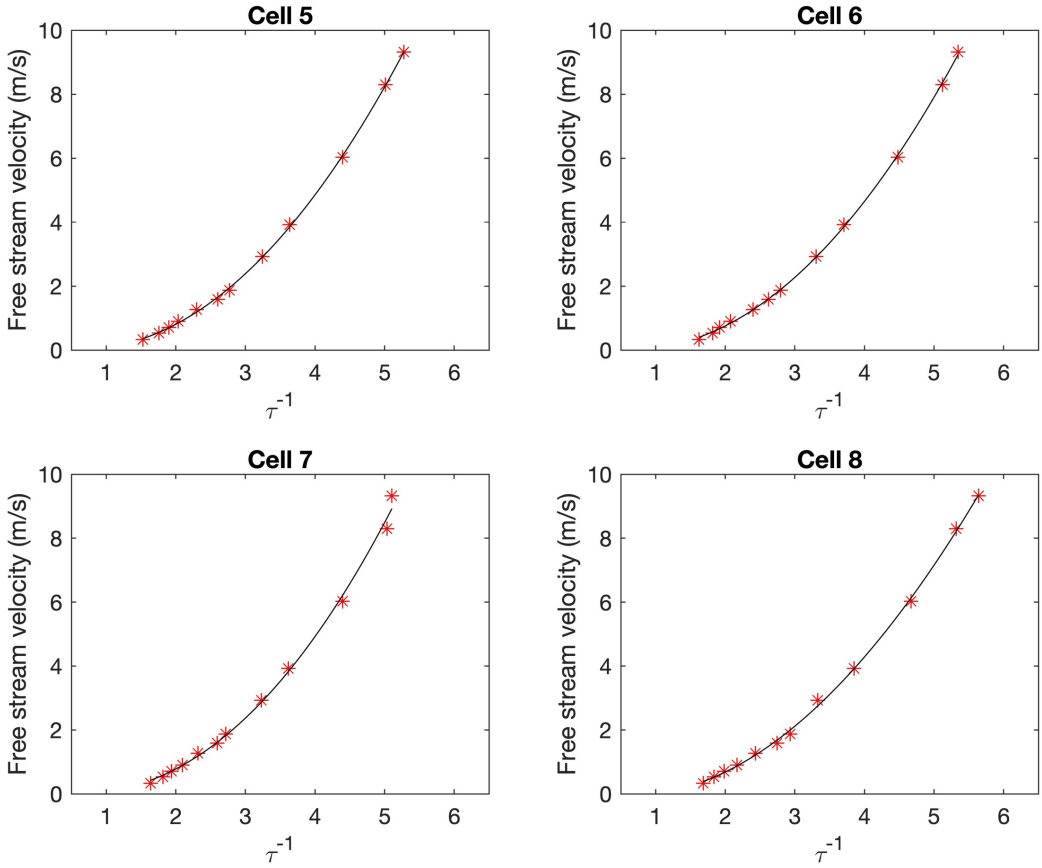

Figure A.8: Cell 5 - 8 Calibration Curves - Fiber-film Probe

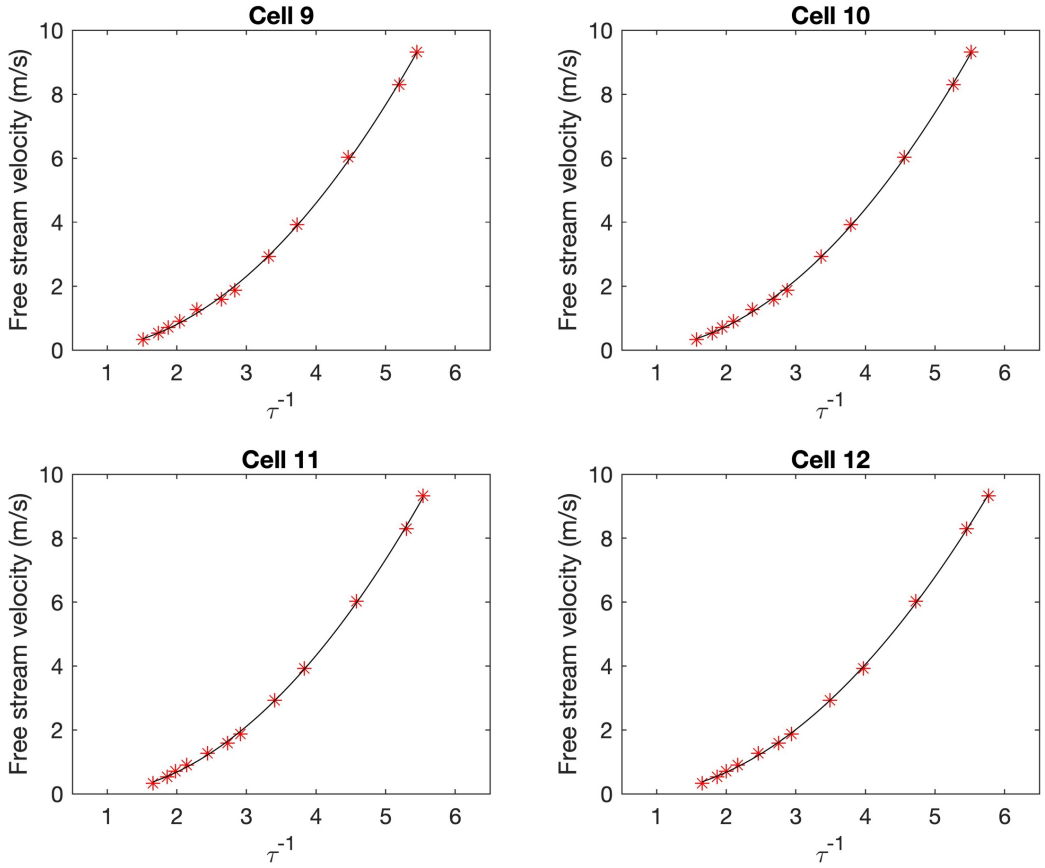

Figure A.9: Cell 9 - 12 Calibration Curves - Fiber-film Probe

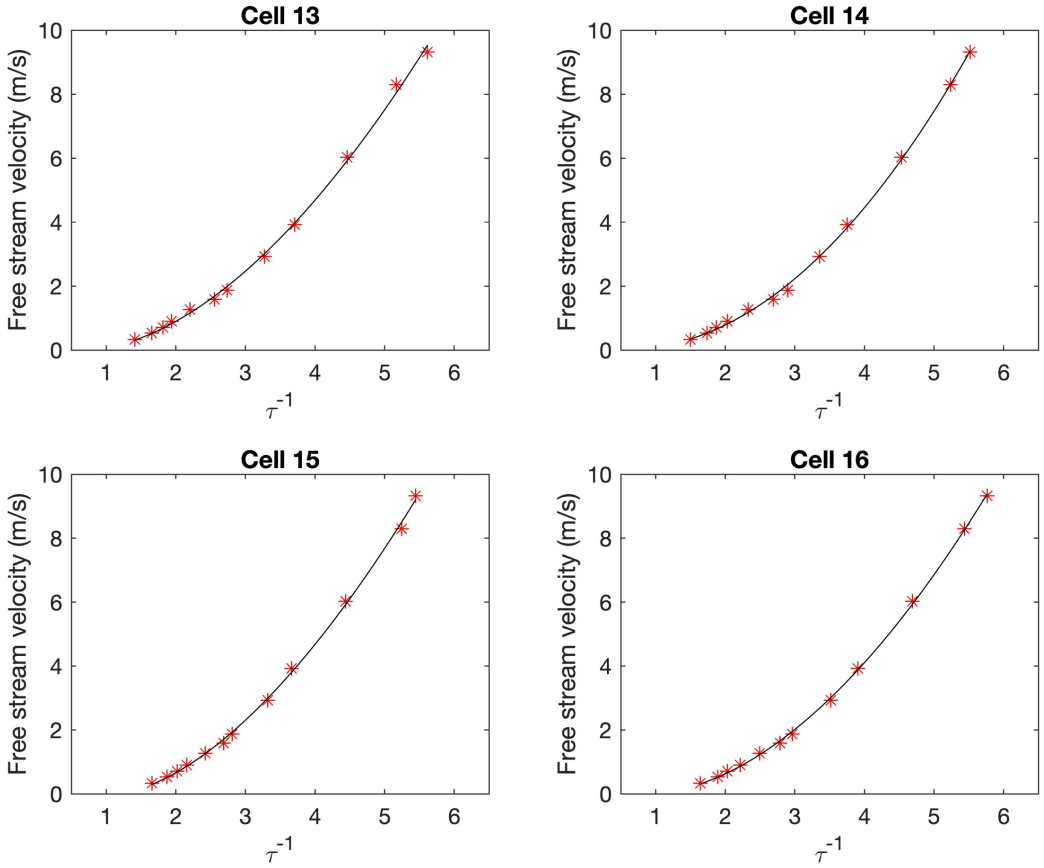

Figure A.10: Cell 13 - 16 Calibration Curves - Fiber-film Probe

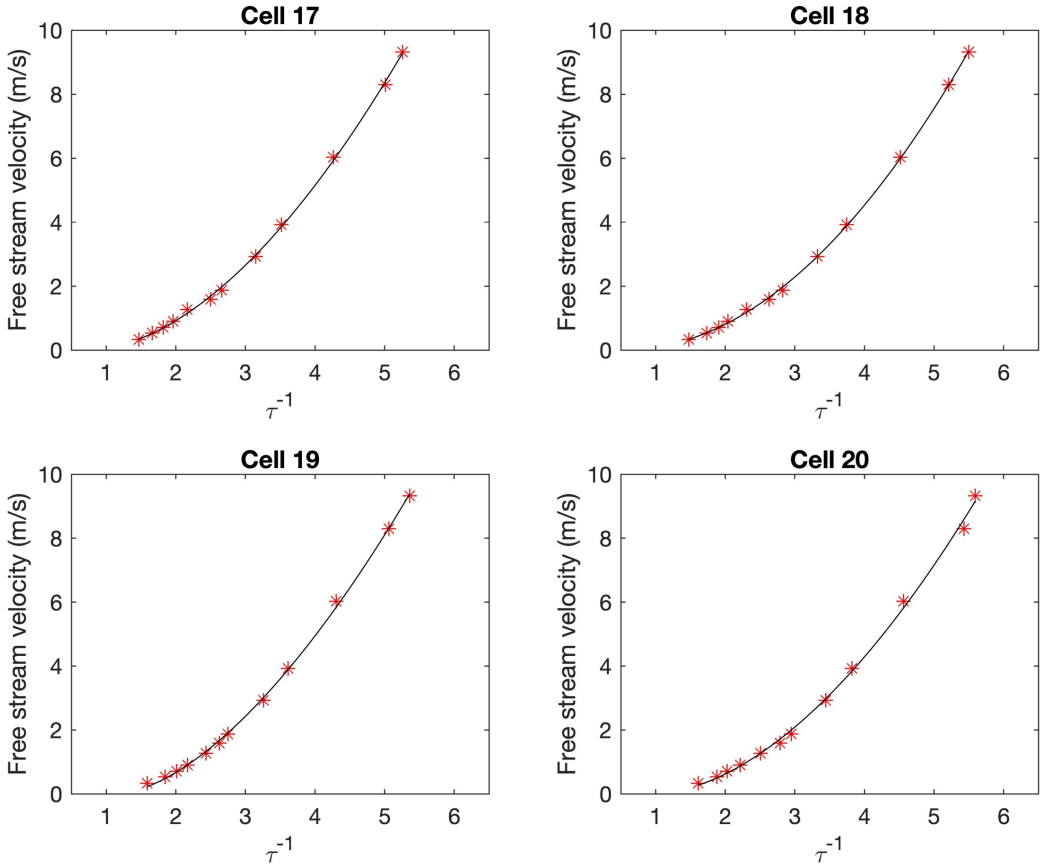

Figure A.11: Cell 17 - 20 Calibration Curves - Fiber-film Probe

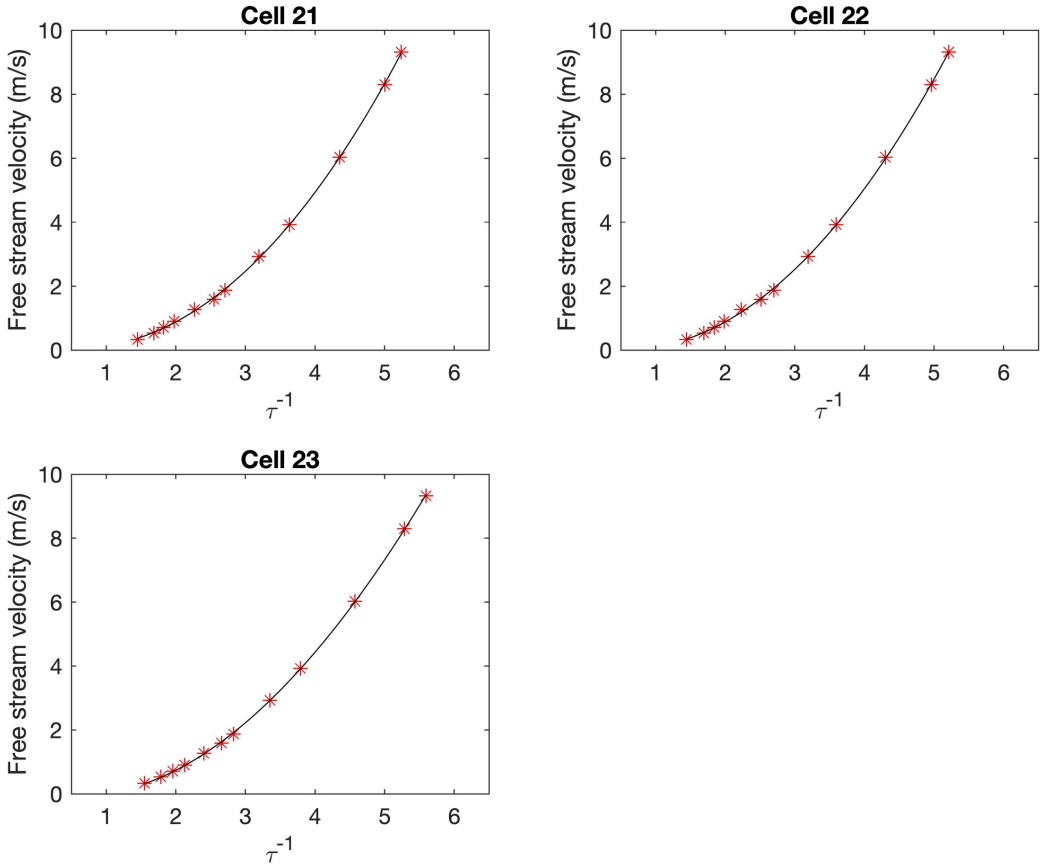

Figure A.12: Cell 21 - 23 Calibration Curves - Fiber-film Probe

APPENDIX B: Numerical Results

B.1 Stock Shroud

B.1.1 Coarse Mesh

The mesh used for the coarse stock shroud simulation has the mesh model parameters that were used in the mesh considerations below (Table B.1).

Table B.1: Stock Shroud - Coarse Mesh Considerations

Surface Mesh Parameters	
Minimum Size	9.5924e-4
Maximum Size	2.45565e-2
Growth Rate	1.2
Size Functions	Curvature and Proximity
Boundary Layers	
Transition	Smooth Transition
Number of Layers	3
Transition Ration	0.272
Growth Rate	1.2
Grown On	Only Walls
Volume Mesh	
Growth Rate	1.2
Maximum Cell Length	3.207809e-2
Boundary Mesh Size	
Nodes	568,347
Faces	160,570
Interior Mesh Size	
Nodes	3,163,889
Faces	4,703,394
Cells	868,883

B.1.2 Fine Mesh

The mesh used for the fine stock shroud simulation has the mesh model parameters that were used in the mesh considerations below (Table B.2).

Table B.2: Stock Shroud - Fine Mesh Considerations

Surface Mesh Parameters	
Minimum Size	6e-5
Maximum Size	1.2e-2
Growth Rate	1.2
Size Functions	Curvature and Proximity
Boundary Layers	
Transition	Smooth Transition
Number of Layers	3
Transition Ration	0.272
Growth Rate	1.2
Grown On	Only Walls
Volume Mesh	
Growth Rate	1.2
Maximum Cell Length	1.596611e-2
Boundary Mesh Size	
Nodes	1,228,487
Faces	330,104
Interior Mesh Size	
Nodes	6,971,362
Faces	10,489,797
Cells	1,971,575

B.2 Modified Shroud

B.2.1 Fine Mesh

The mesh used for the modified shroud simulation, which was a relatively fine mesh, has the mesh model parameters that were used in the mesh considerations below (Table B.3).

Table B.3: Modified Shroud - Fine Mesh Considerations

Surface Mesh Parameters	
Minimum Size	9.5924e-4
Maximum Size	2.45565e-2
Growth Rate	1.2
Size Functions	Curvature and Proximity
Boundary Layers	
Transition	Smooth Transition
Number of Layers	3
Transition Ration	0.272
Growth Rate	1.2
Grown On	Only Walls
Volume Mesh	
Growth Rate	1.2
Maximum Cell Length	3.207809e-2
Boundary Mesh Size	
Nodes	218,504
Faces	70,184
Interior Mesh Size	
Nodes	1,031,570
Faces	1,514,640
Cells	274,339

B.3 Model Set Up

The parameters considerations for the model set up of the stock shroud and modified shroud can be summarized in the following table, Table B.4.

Table B.4: CFD Model Considerations

Set Up Settings	
Solver Settings	
Solver	Pressure-Based and Steady
Fluid Properties	
Density Viscosity	1.225 kg/m^3 1.7894e-5 kg/(m s)
Boundary Conditions	
TTA Cell Inlets	
Velocity Condition Turbulence Intensity Viscosity Ratio	Applied Velocity (see Figure 4.3) 5% 10
TTA Cell Sides	
Velocity Condition	Flow cell slip interface
Inlet (Other)	
Velocity Condition Turbulence Intensity Viscosity Ratio	Average Velocity (see Figure 4.3) 5% 10
Sides of Inlet Flow	
Velocity Condition	Solid walls, no-slip condition
Shroud Walls	
Velocity Condition	Solid walls, no-slip condition
Shroud Outlet	
Pressure Condition	-57.04 Pa
Convergence Criteria	
Maximum Iterations	1500

APPENDIX C: Radiator Only Results

Table C.1: Radiator Velocity Measurement Steps

Velocity Step	U_{avg} (m/s)	ΔP (Pa)
1	2.26	33.99
2	2.83	49.89
3	3.30	64.60
4	3.74	78.90
5	4.19	95.52
6	4.61	111.62
7	4.93	124.13
8	5.34	140.29
9	5.68	155.23
10	6.04	171.20
11	6.36	185.81
12	6.72	202.38
13	7.05	217.98

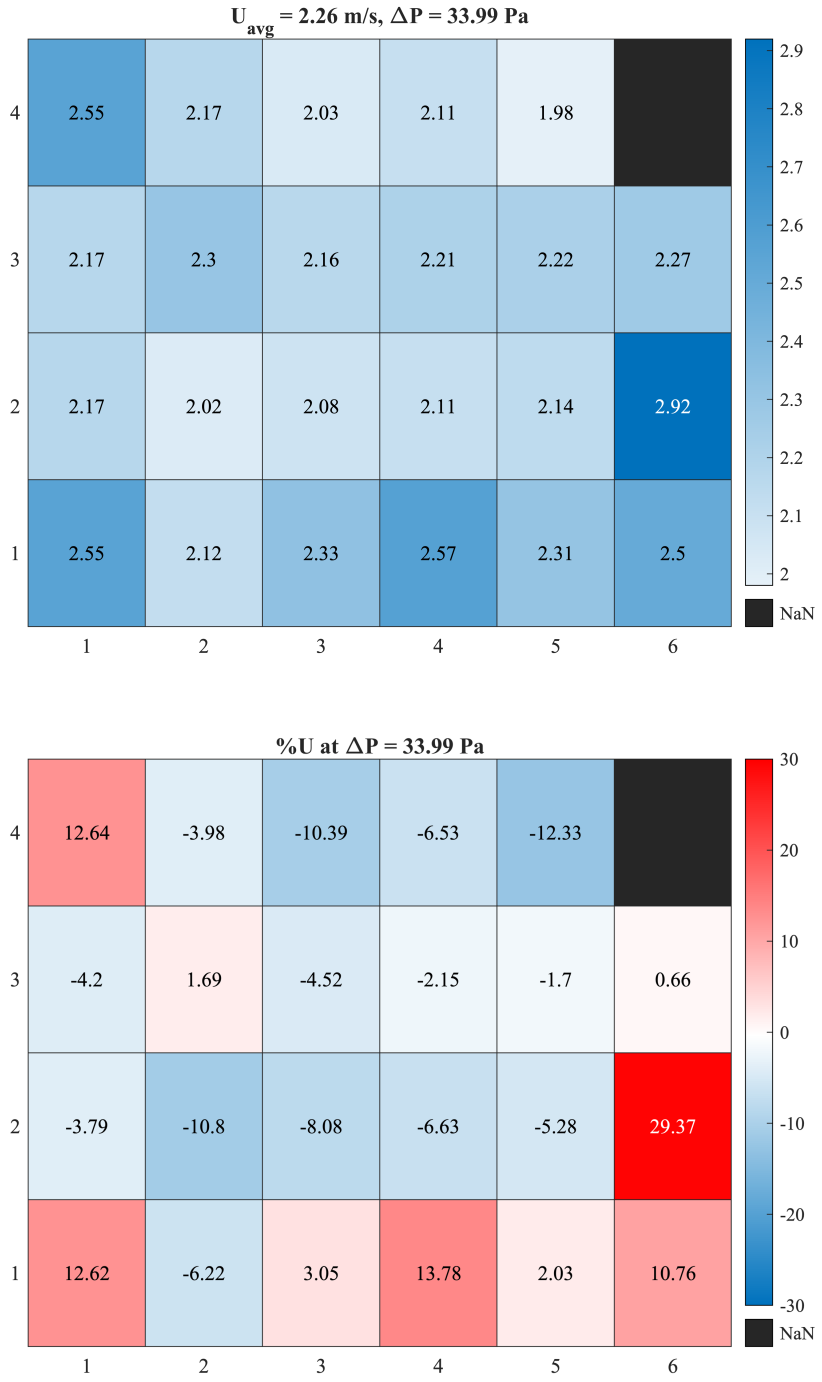

Figure C.1 Radiator Flow Distribution at ΔP = 33.99 Pa

(Above: Velocity Distribution, Below: Velocity Percent Difference Distribution)

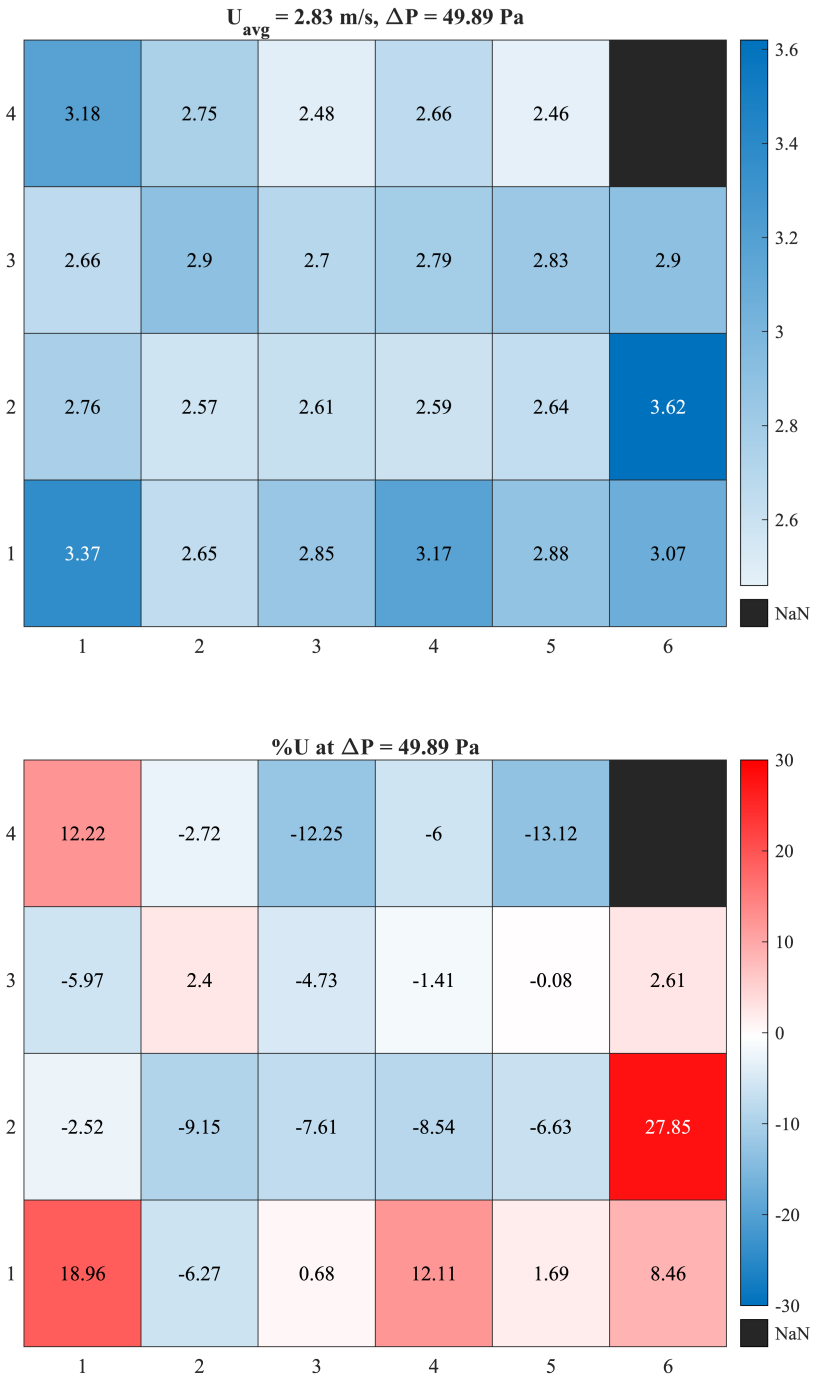

Figure C.2 Radiator Flow Distribution at ΔP = 48.89 Pa

(Above: Velocity Distribution, Below: Velocity Percent Difference Distribution)

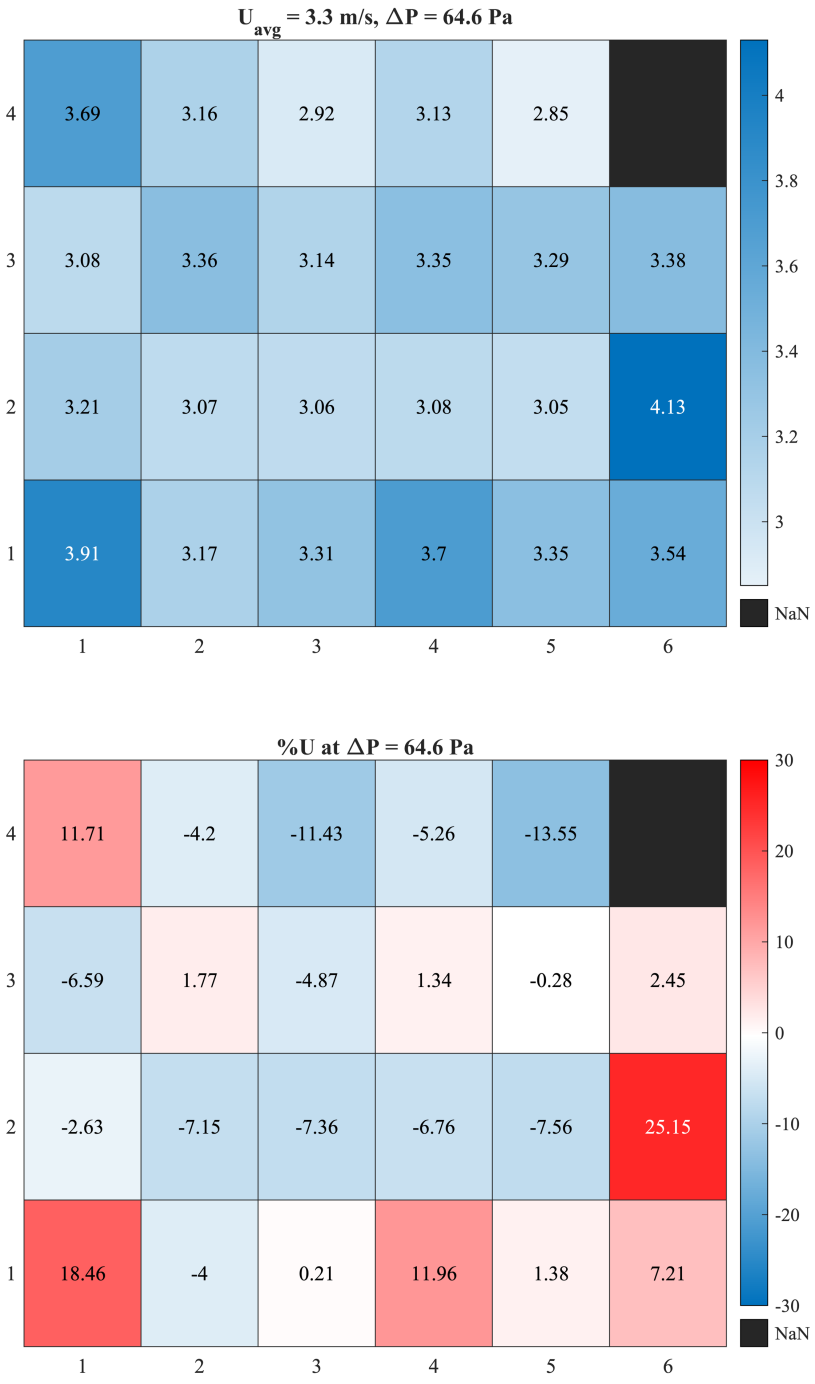

Figure C.3 Radiator Flow Distribution at ΔP = 64.60 Pa

(Above: Velocity Distribution, Below: Velocity Percent Difference Distribution)

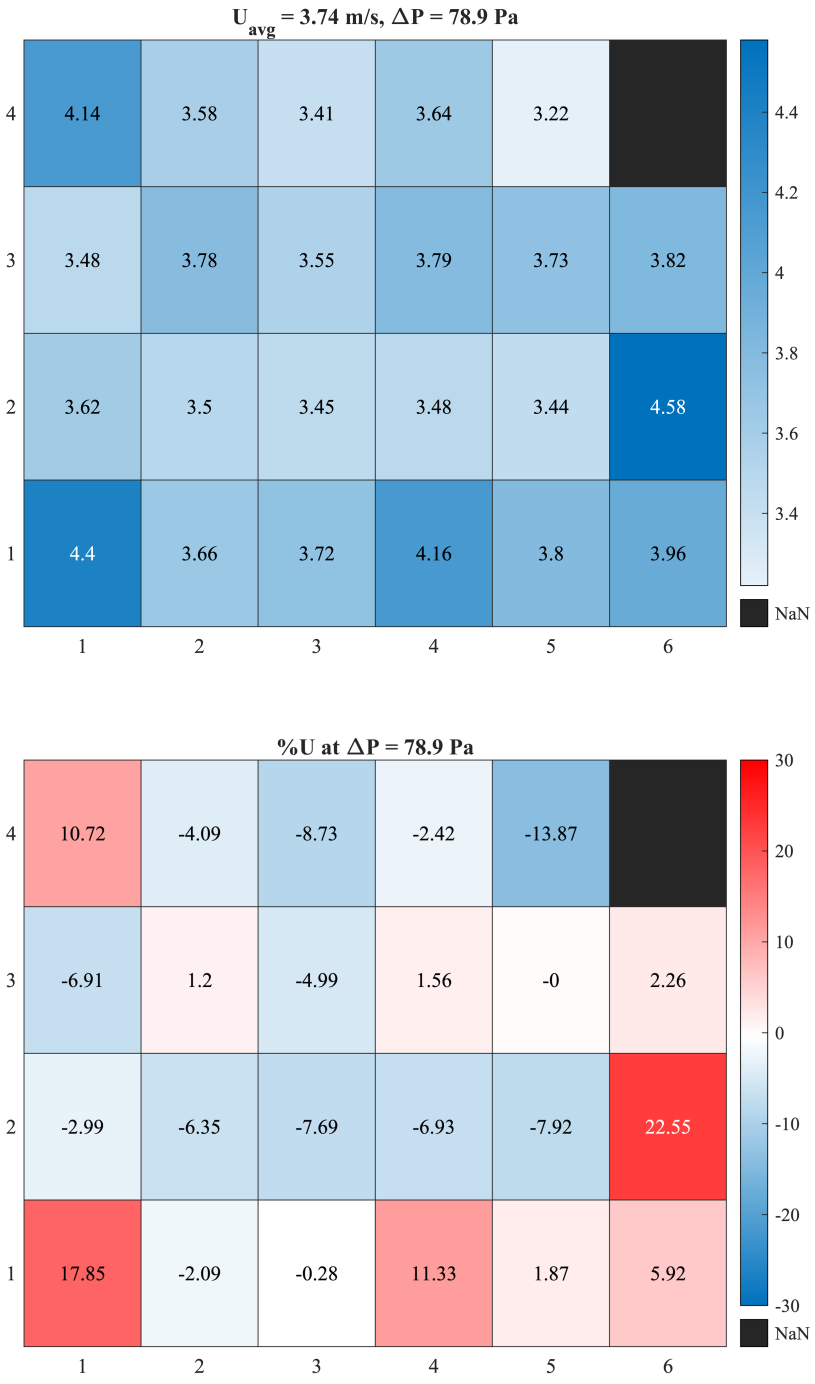

Figure C.4 Radiator Flow Distribution at ΔP = 78.90 Pa

(Above: Velocity Distribution, Below: Velocity Percent Difference Distribution)

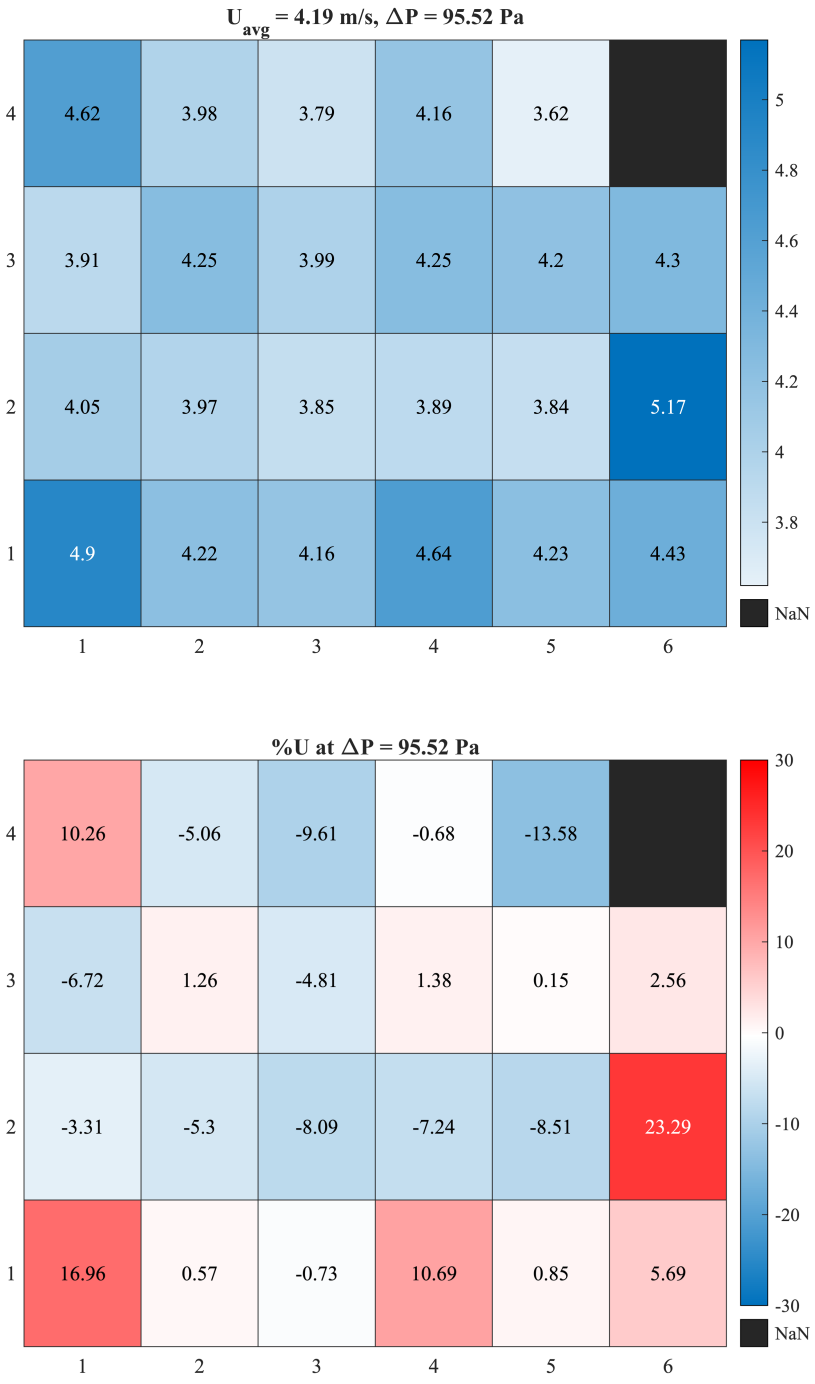

Figure C.5 Radiator Flow Distribution at ΔP = 95.52 Pa

(Above: Velocity Distribution, Below: Velocity Percent Difference Distribution)

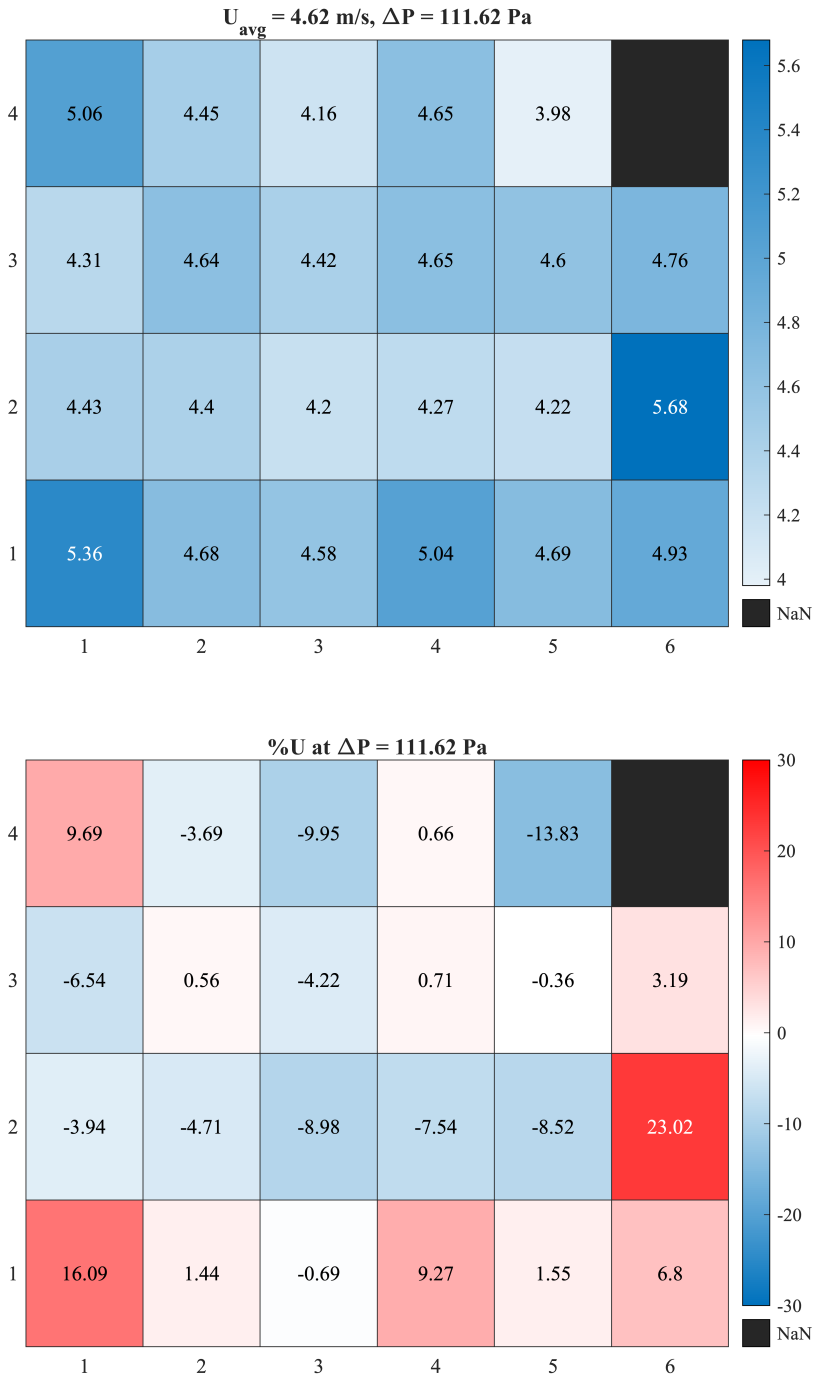

Figure C.6 Radiator Flow Distribution at ΔP = 116.20 Pa

(Above: Velocity Distribution, Below: Velocity Percent Difference Distribution)

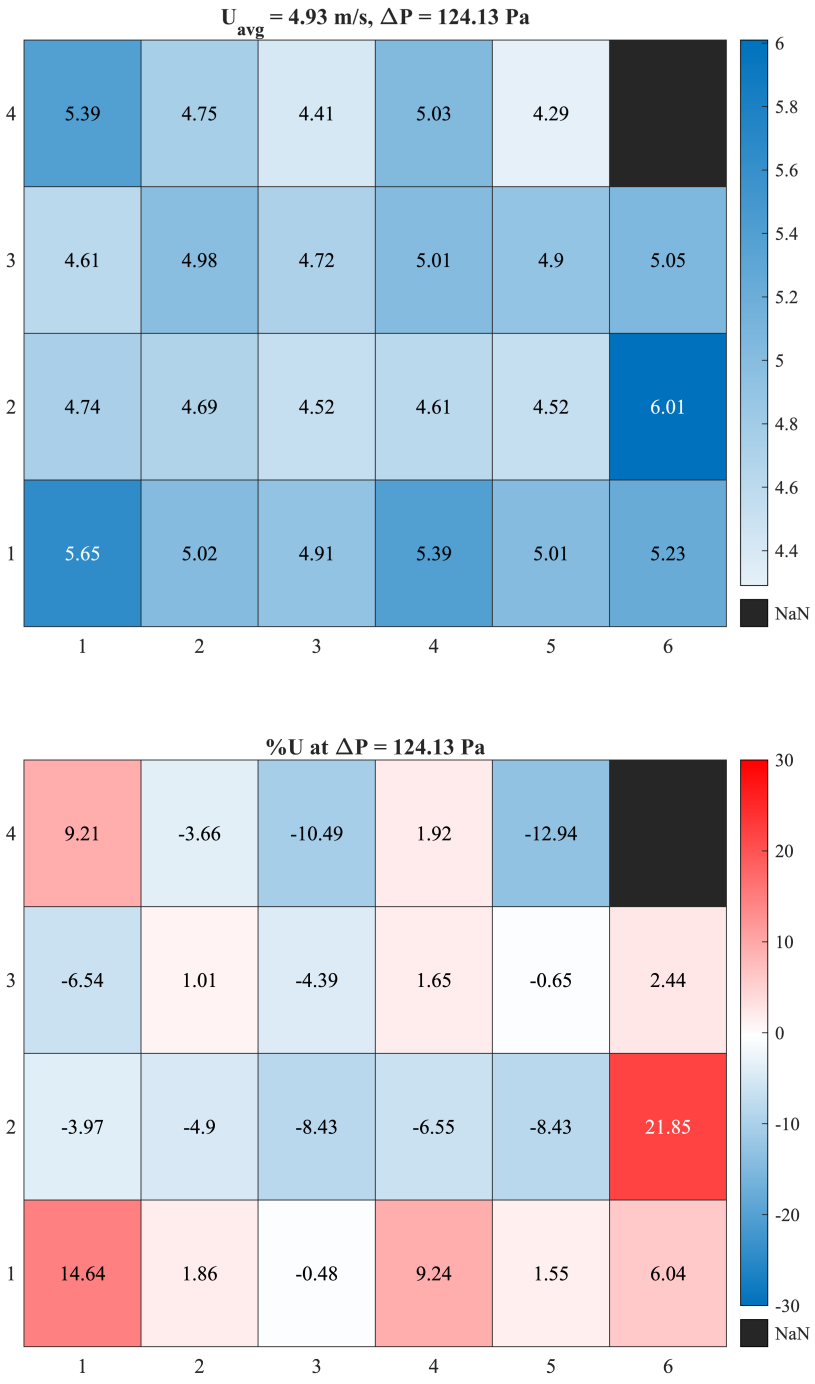

Figure C.7 Radiator Flow Distribution at ΔP = 124.13 Pa

(Above: Velocity Distribution, Below: Velocity Percent Difference Distribution)

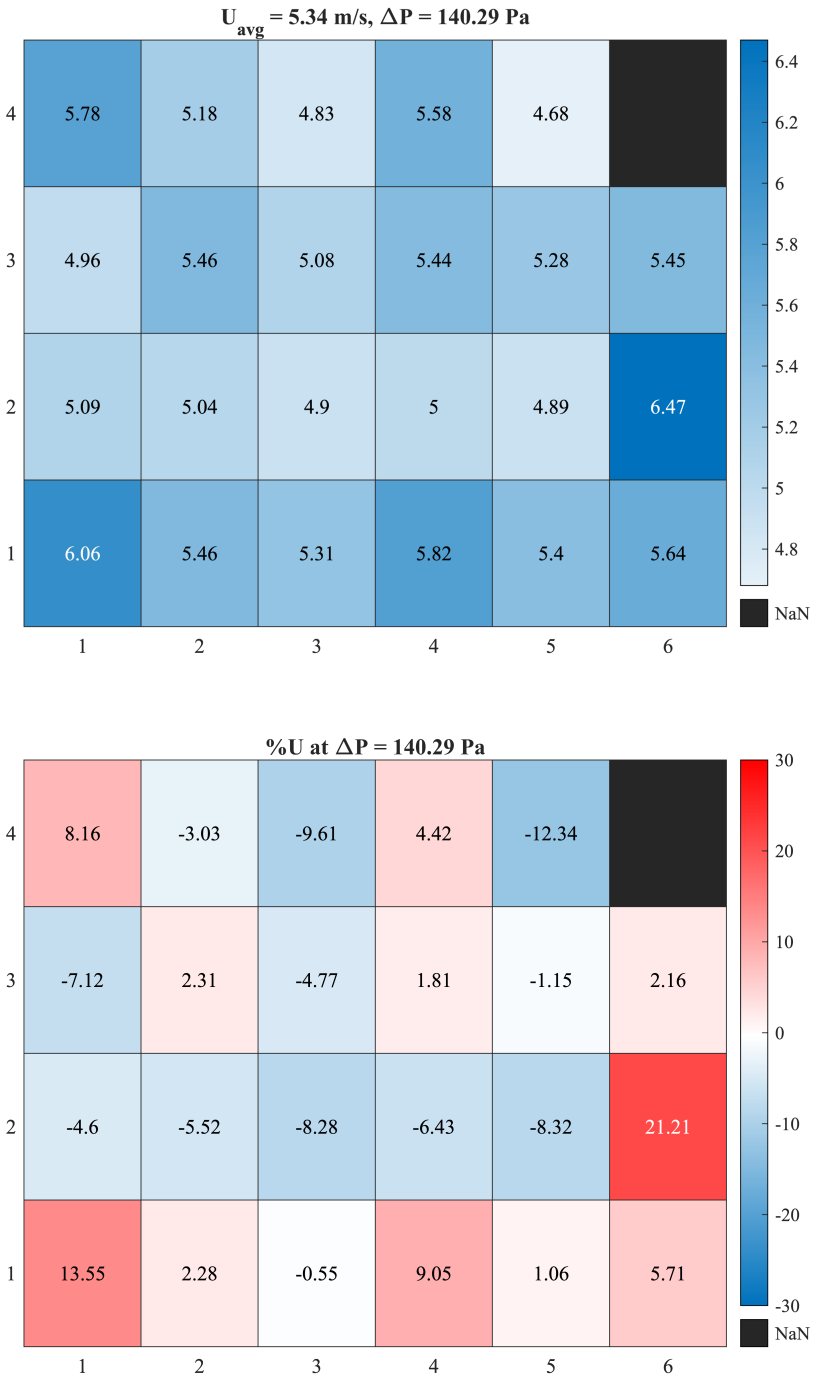

Figure C.8 Radiator Flow Distribution at ΔP = 140.29 Pa

(Above: Velocity Distribution, Below: Velocity Percent Difference Distribution)

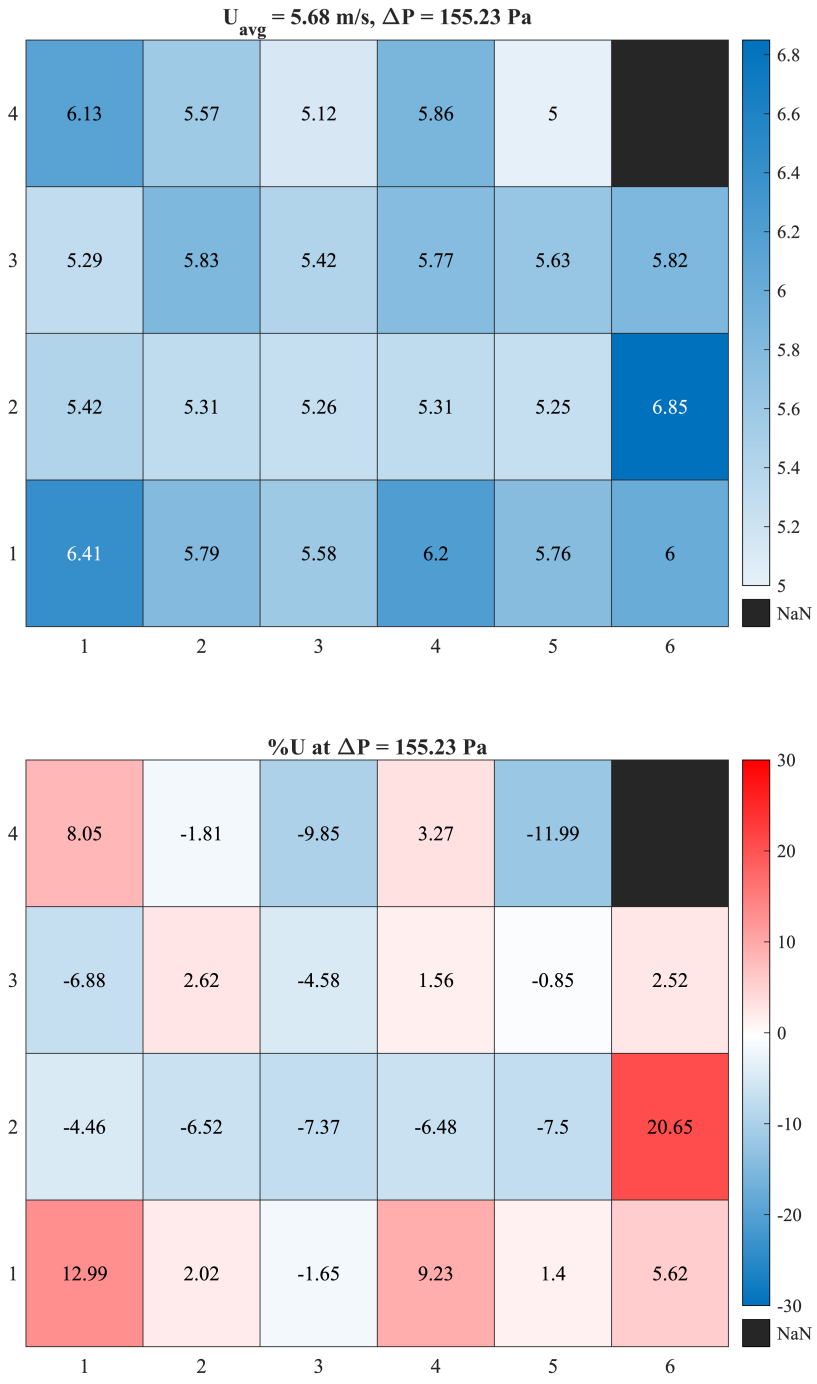

Figure C.9 Radiator Flow Distribution at ΔP = 155.23 Pa

(Above: Velocity Distribution, Below: Velocity Percent Difference Distribution)

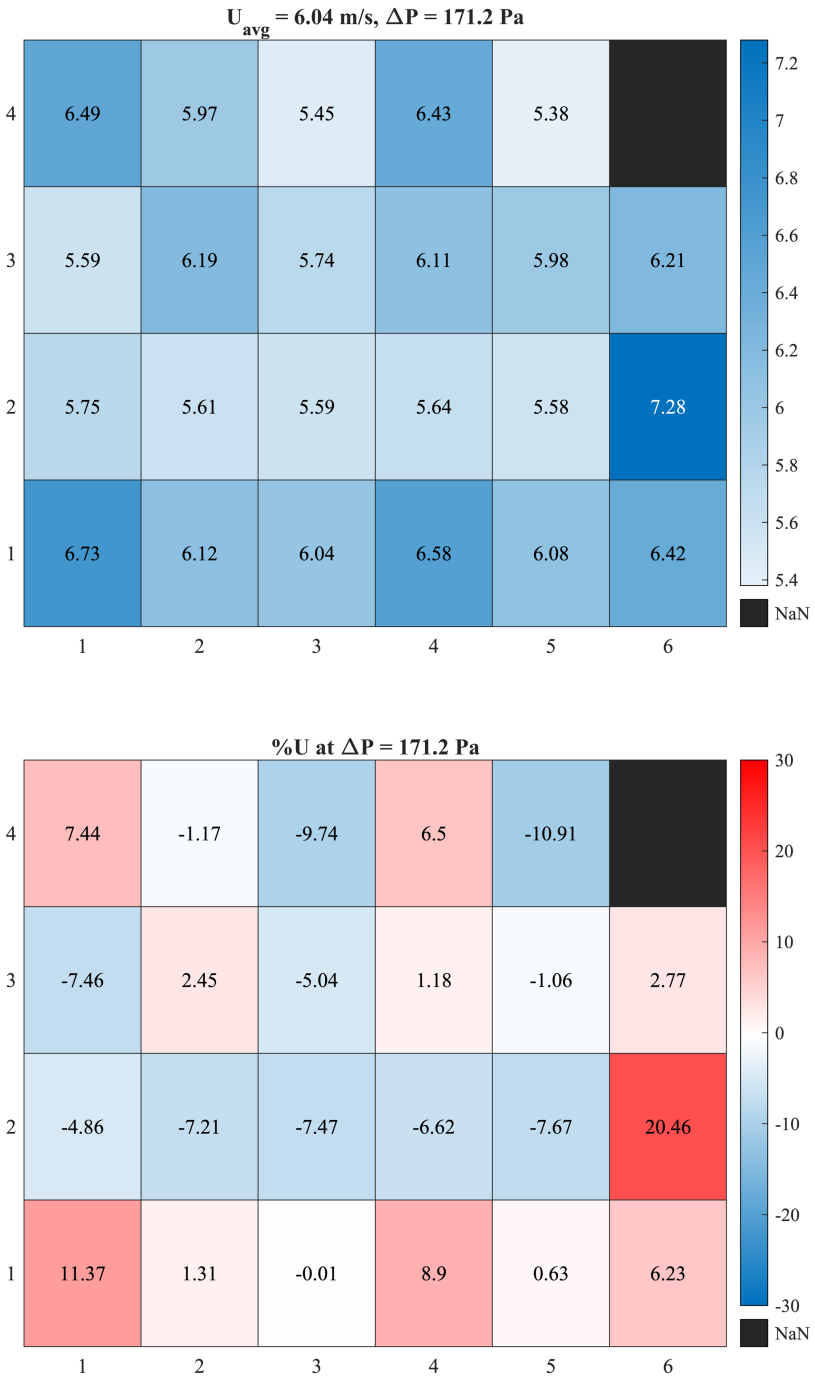

Figure C.10 Radiator Flow Distribution at ΔP = 171.20 Pa

(Above: Velocity Distribution, Below: Velocity Percent Difference Distribution)

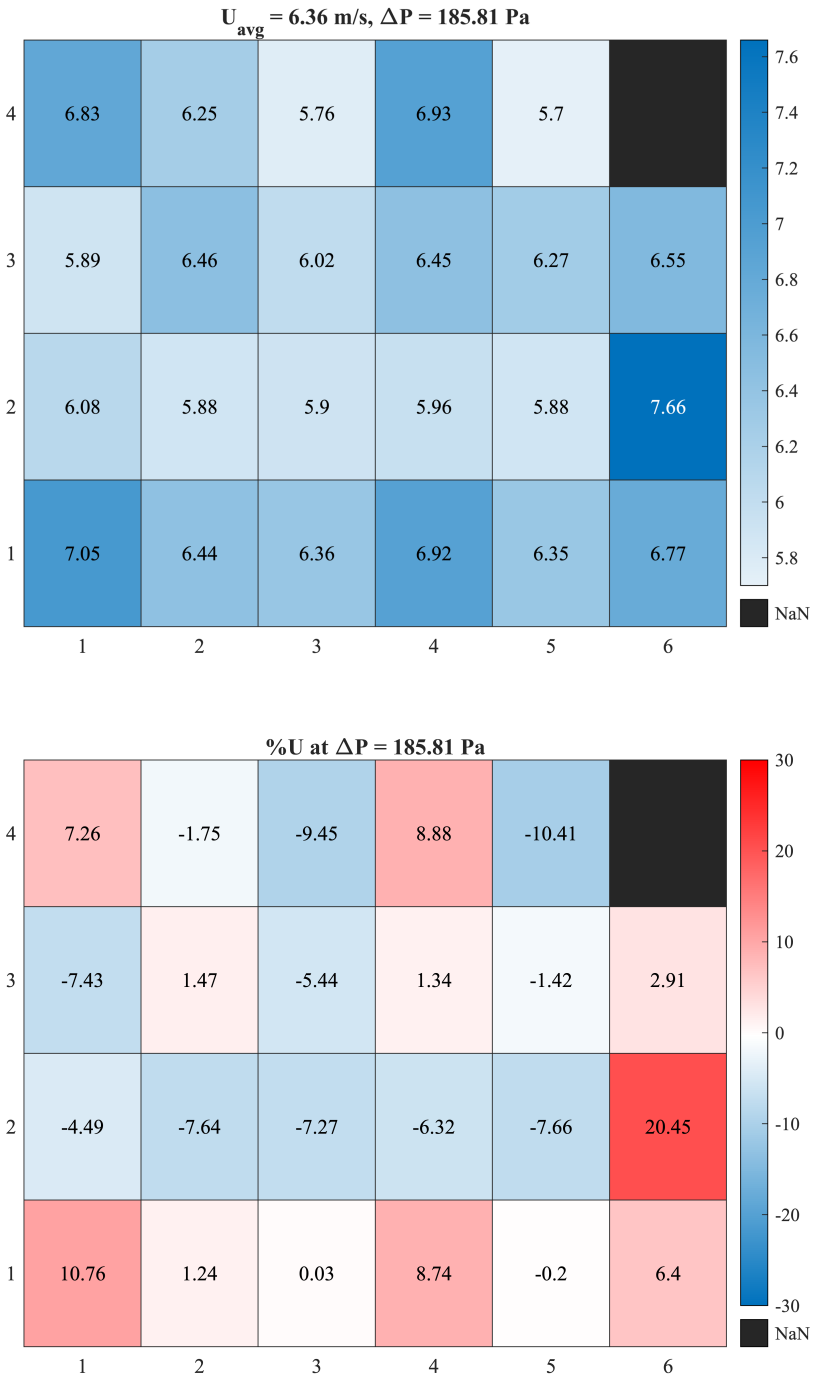

Figure C.11 Radiator Flow Distribution at ΔP = 185.81 Pa

(Above: Velocity Distribution, Below: Velocity Percent Difference Distribution)

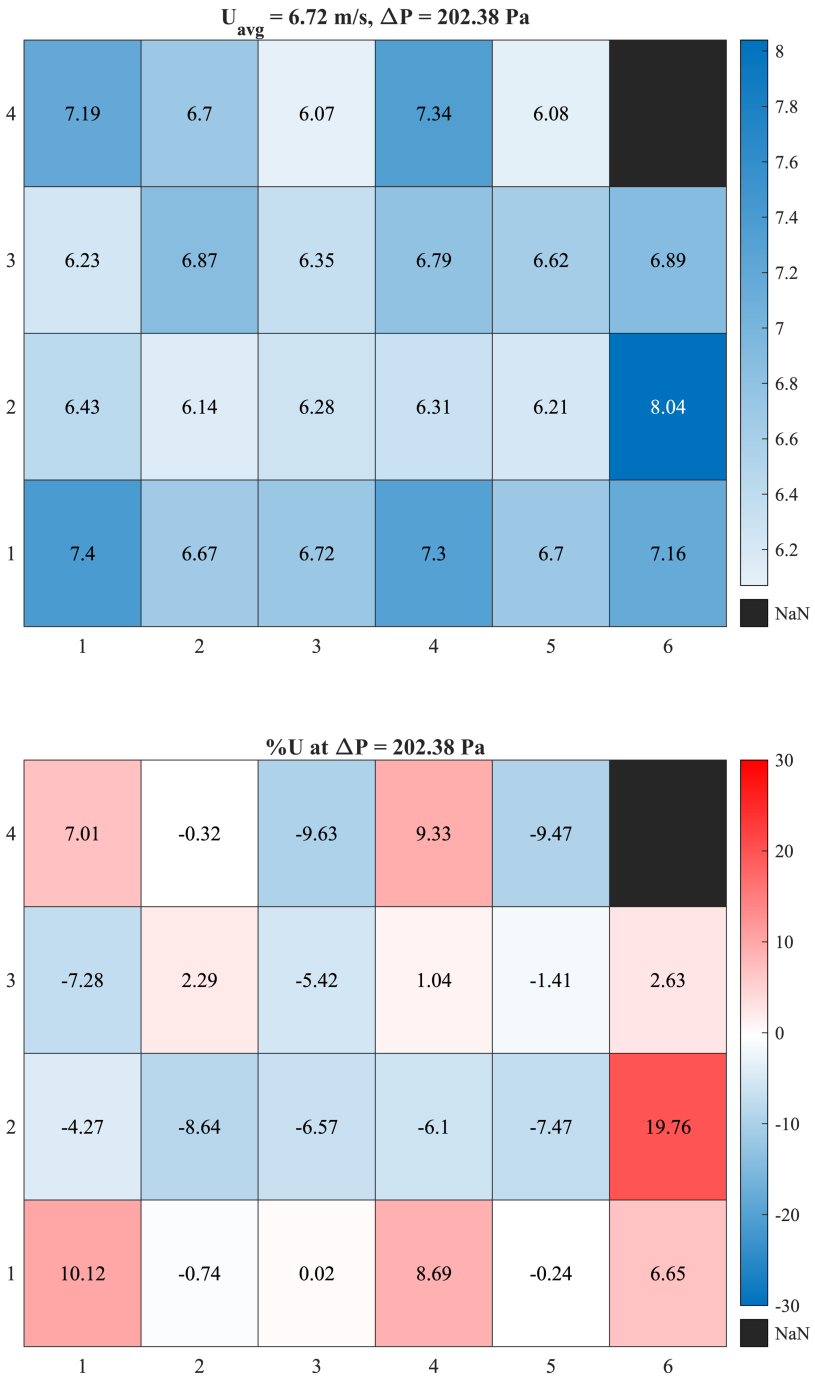

Figure C.12 Radiator Flow Distribution at ΔP = 202.38 Pa

(Above: Velocity Distribution, Below: Velocity Percent Difference Distribution)

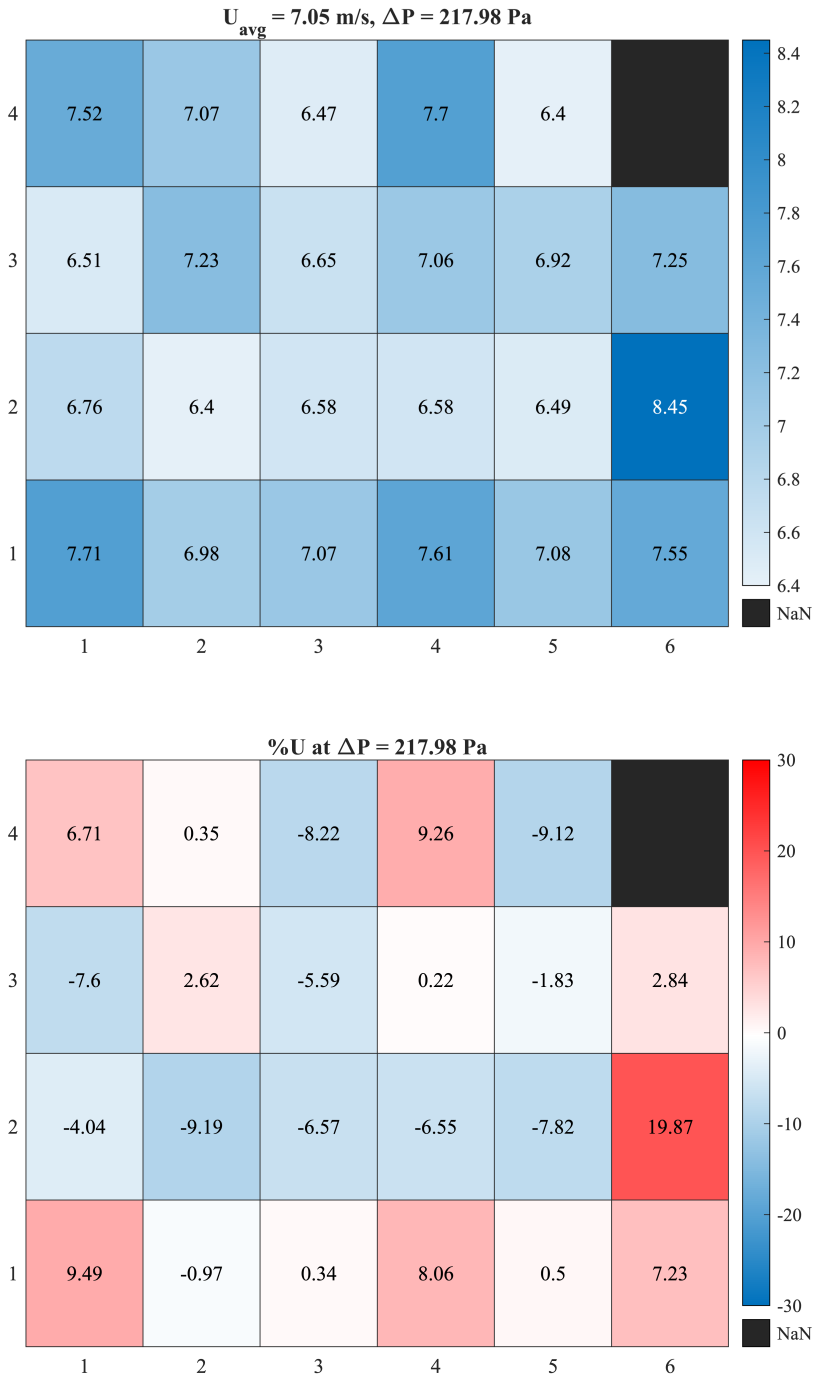

Figure C.13 Radiator Flow Distribution at ΔP = 217.98 Pa

(Above: Velocity Distribution, Below: Velocity Percent Difference Distribution)

APPENDIX D: Stock Results

Table D.1: Stock Shroud Velocity Measurement Steps

Velocity Step	U_{avg} (m/s)	ΔP (Pa)
1	0.78	18.22
2	1.07	32.77
3	1.32	48.32
4	1.52	63.77
5	1.68	76.59
6	1.87	92.91
7	2.04	109.46
8	2.21	125.72
9	2.36	140.89
10	2.50	155.84
11	2.63	170.16
12	2.78	187.64
13	2.90	202.13
14	3.04	218.72

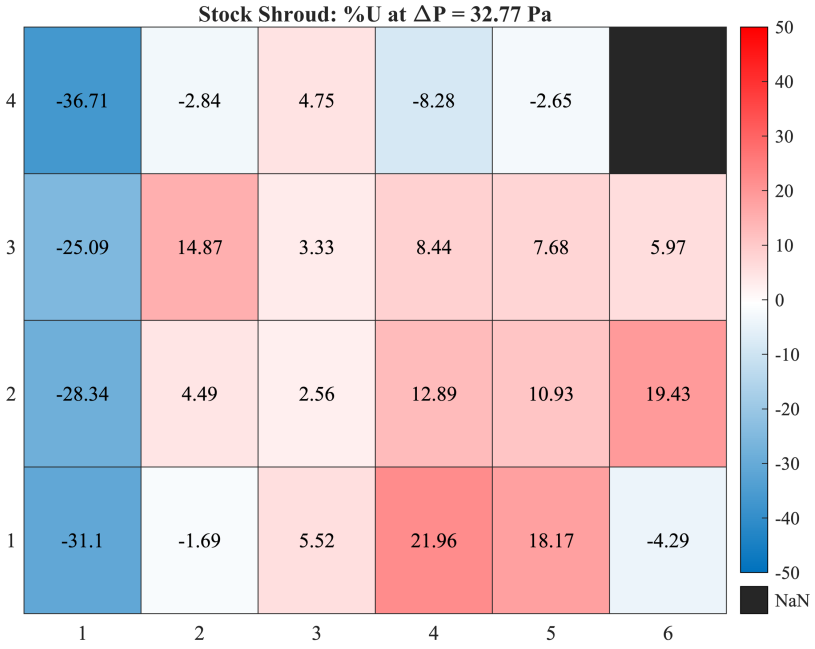

Figure D.1: Velocity Percent Difference at ΔP = 48.32 Pa (U_{avg} = 1.32 m/s)

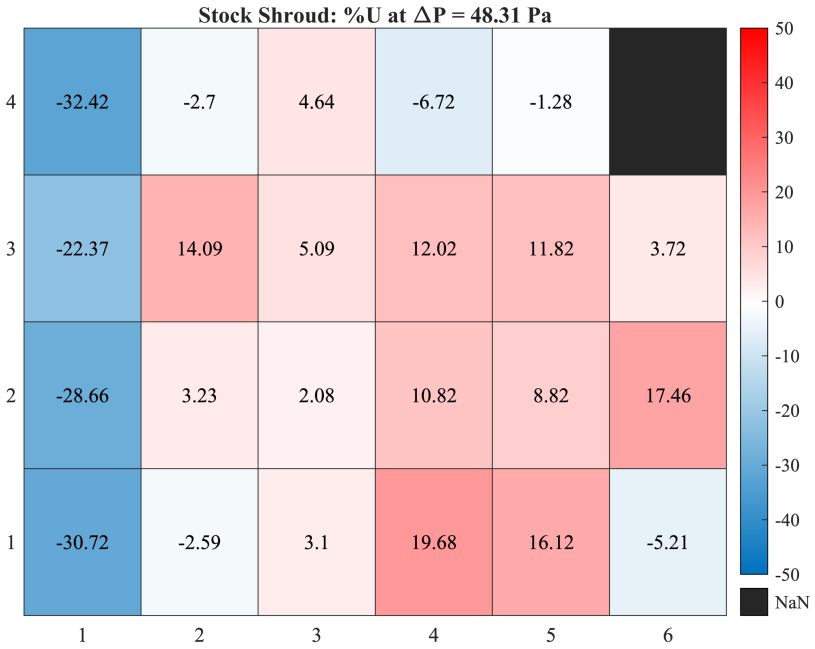

Figure D.2: Velocity Percent Difference at ΔP = 48.31 Pa (U_{avg} = 1.32 m/s)

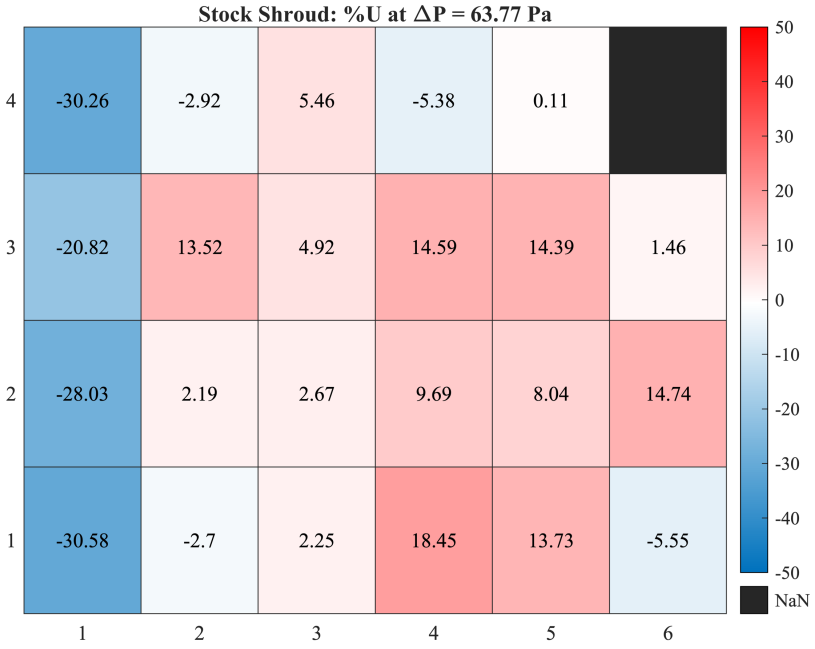

Figure D.3: Velocity Percent Difference at ΔP = 63.77 Pa (U_{avg} = 1.52 m/s)

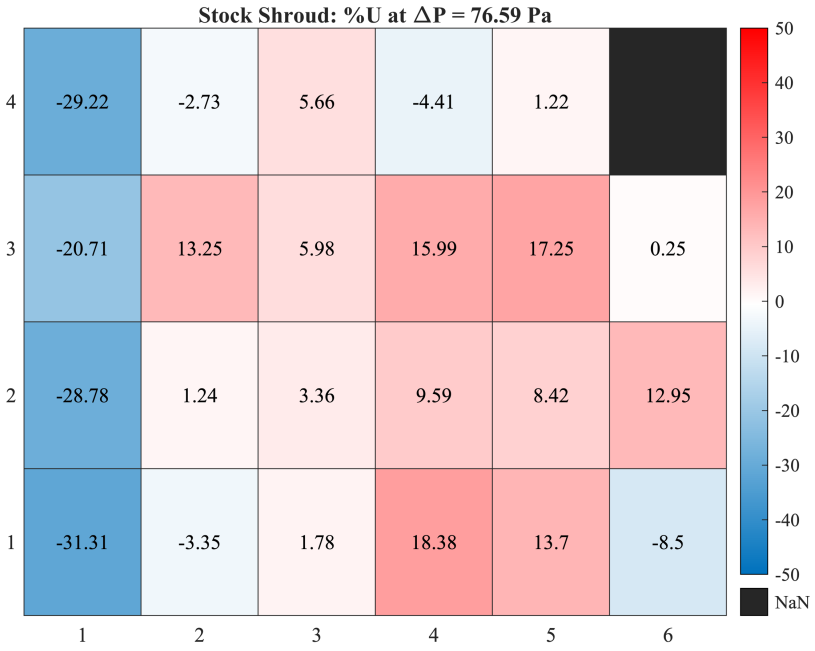

Figure D.4: Velocity Percent Difference at ΔP = 76.59 Pa (U_{avg} = 1.68 m/s)

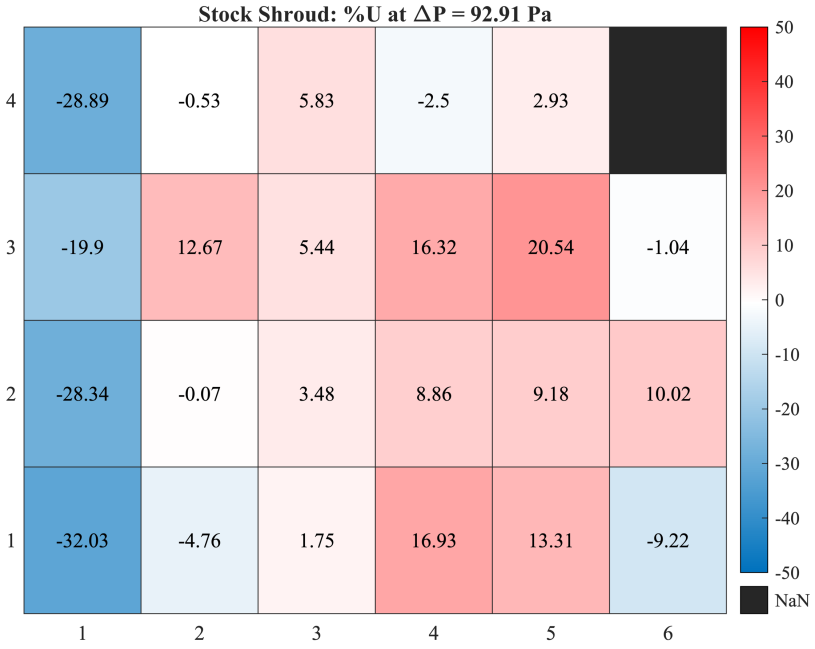

Figure D.5: Velocity Percent Difference at ΔP = 92.91 Pa (U_{avg} = 1.87 m/s)

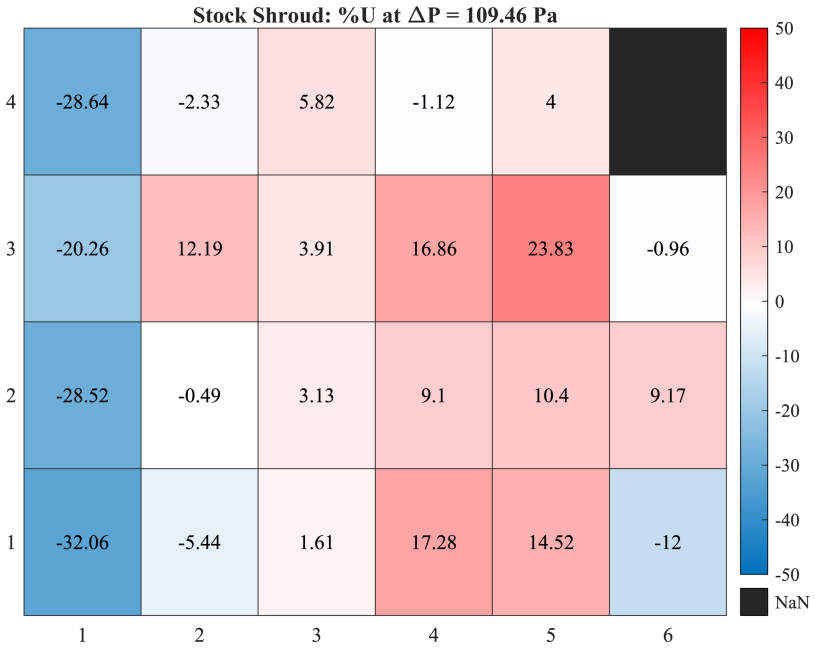

Figure D.6: Velocity Percent Difference at ΔP = 109.46 Pa (U_{avg} = 2.04 m/s)

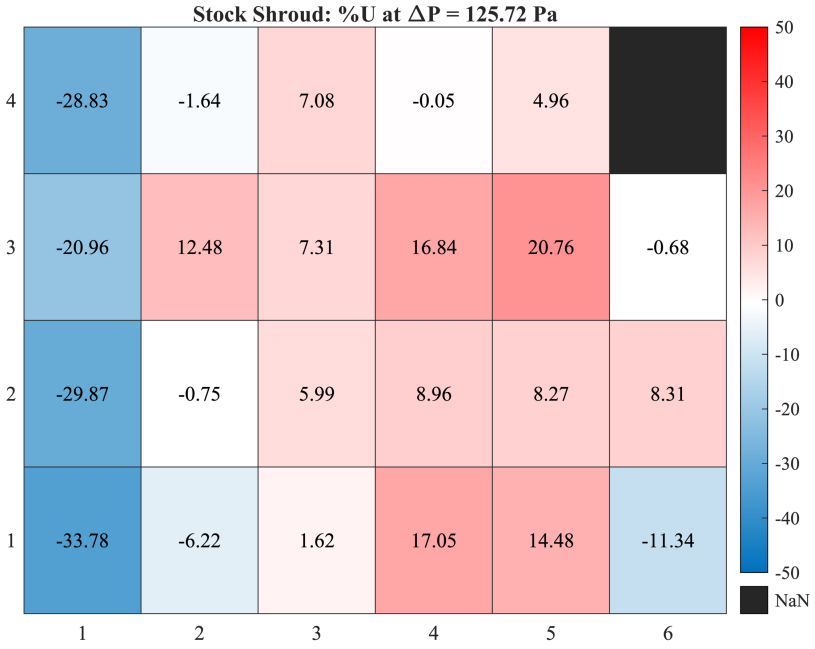

Figure D.7: Velocity Percent Difference at ΔP = 125.72 Pa (U_{avg} = 2.21 m/s)

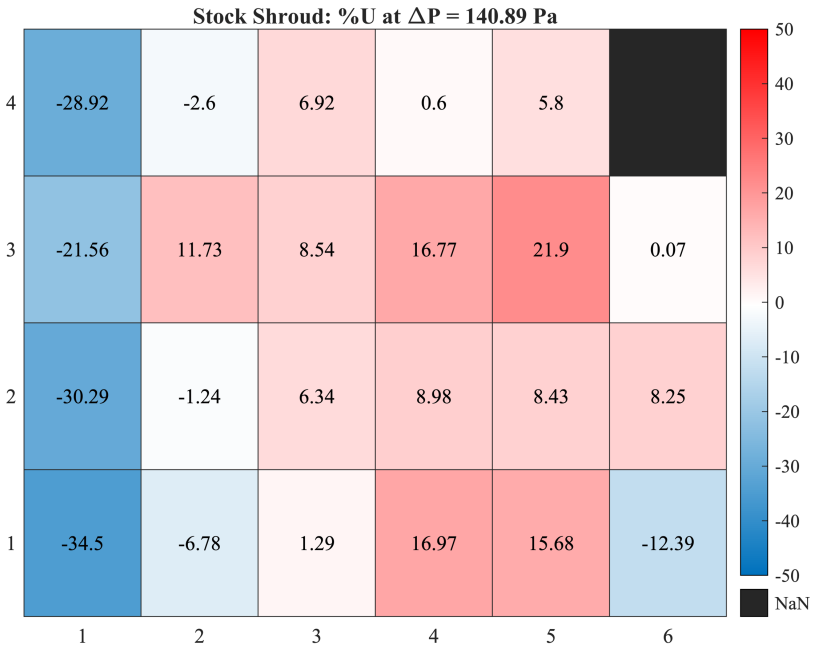

Figure D.8: Velocity Percent Difference at ΔP = 140.89 Pa (U_{avg} = 2.36 m/s)

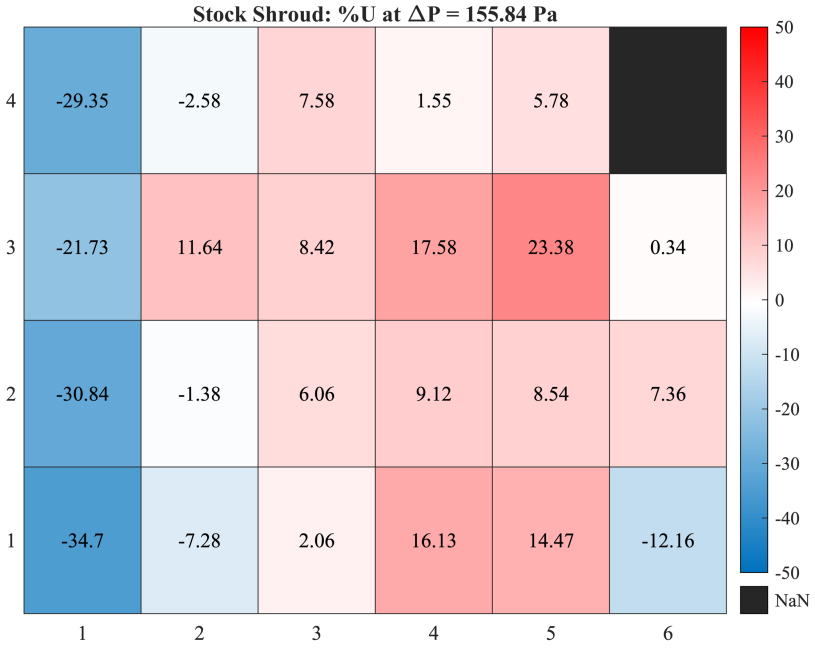

Figure D.9: Velocity Percent Difference at ΔP = 155.84 Pa (U_{avg} = 2.50 m/s)

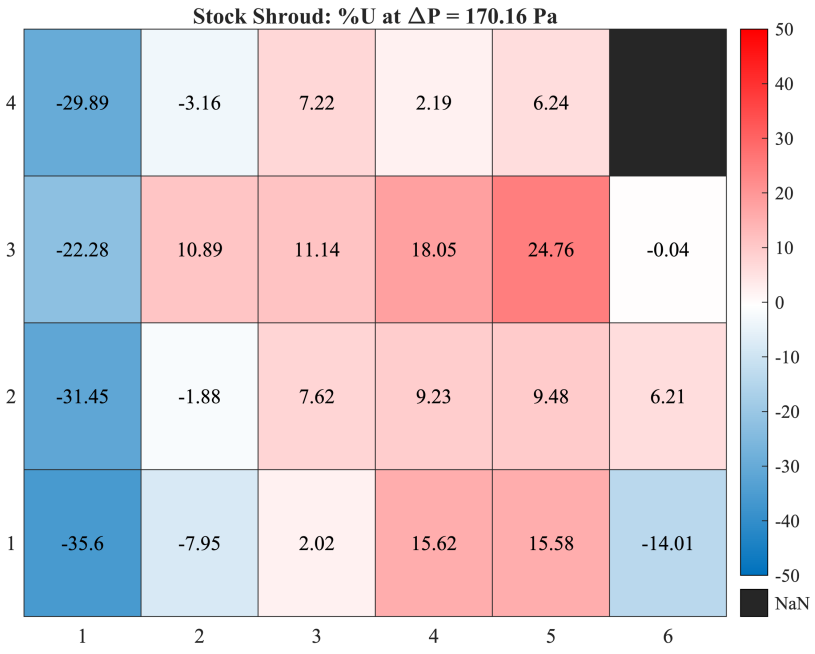

Figure D.10: Velocity Percent Difference at ΔP = 170.16 Pa (U_{avg} = 2.63 m/s)

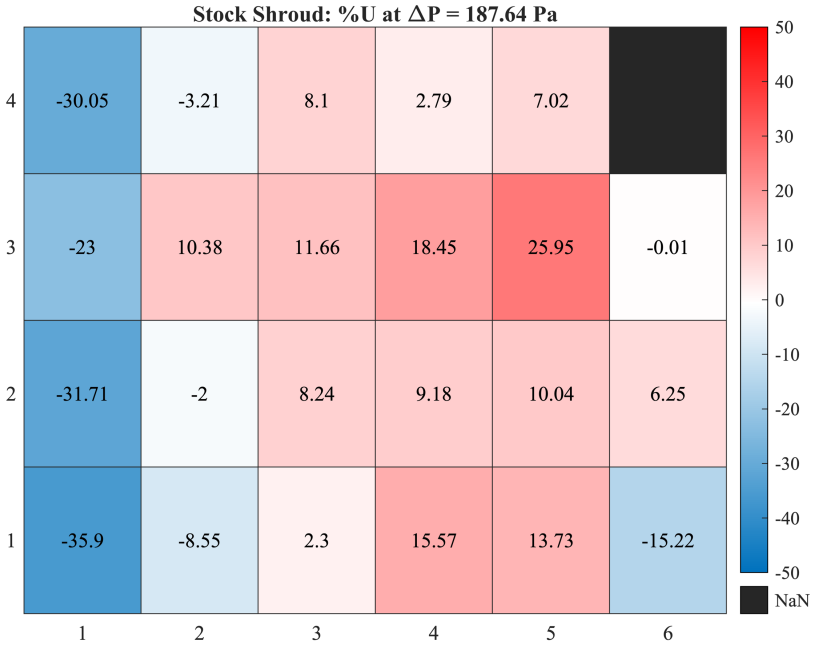

Figure D.11: Velocity Percent Difference at ΔP = 187.64 Pa (U_{avg} = 2.78 m/s)

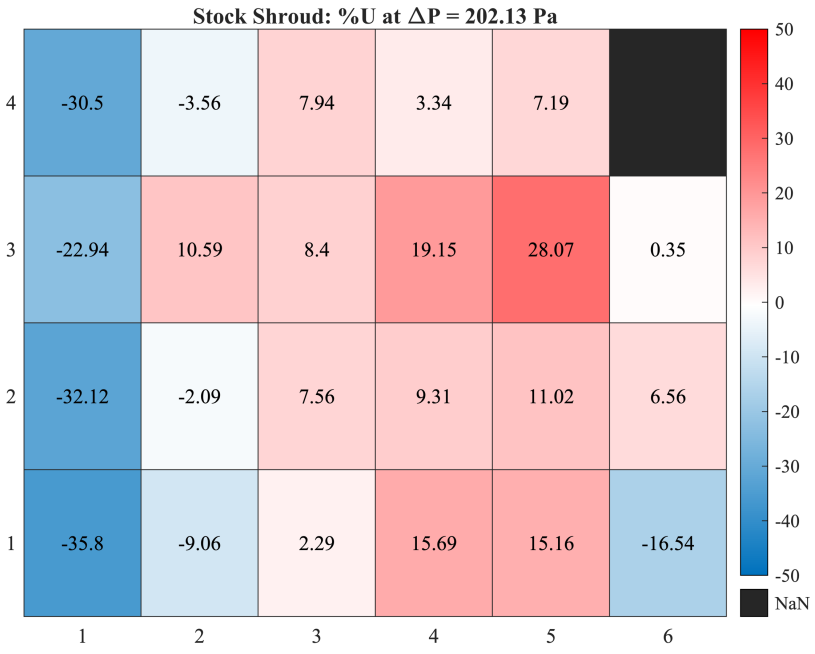

Figure D.12: Velocity Percent Difference at ΔP = 202.13 Pa (U_{avg} = 2.90 m/s)

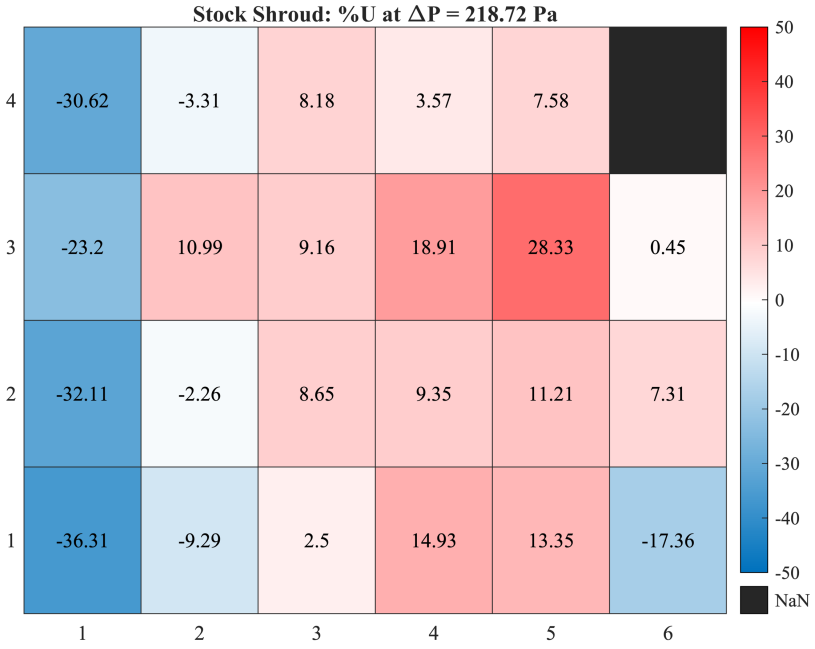

Figure D.13: Velocity Percent Difference at ΔP = 218.72 Pa (U_{avg} = 3.04 m/s)

APPENDIX E: Modified Shroud Results

Table E.1: Modified Shroud Velocity Measurement Steps

Velocity Step	U_{avg} (m/s)	ΔP (Pa)
1	0.77	18.79
2	1.07	33.14
3	1.30	48.94
4	1.49	63.35
5	1.68	78.82
6	1.83	93.30
7	2.00	108.75
8	2.17	126.64
9	2.30	140.89
10	2.42	153.86
11	2.57	171.13
12	2.70	186.45
13	2.81	199.51
14	2.98	219.76

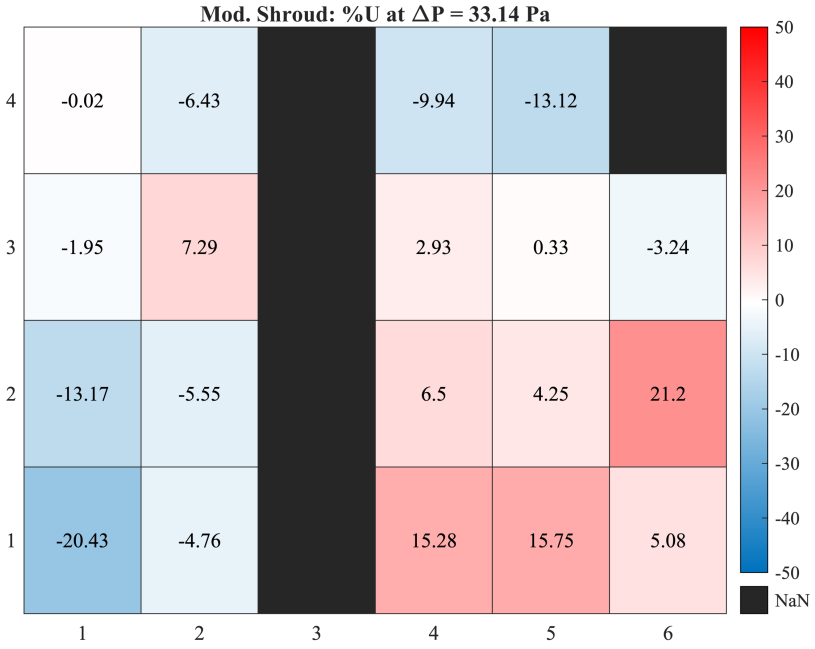

Figure E.1: Velocity Percent Difference at ΔP = 33.14 Pa (U_{avg} = 1.07 m/s)

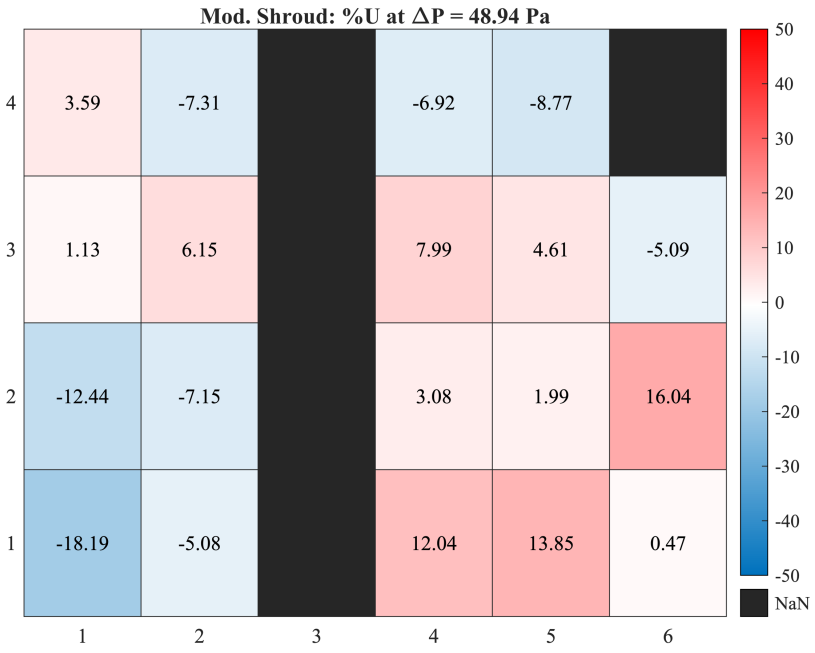

Figure E.2: Velocity Percent Difference at ΔP = 48.94 Pa (U_{avg} = 1.30 m/s)

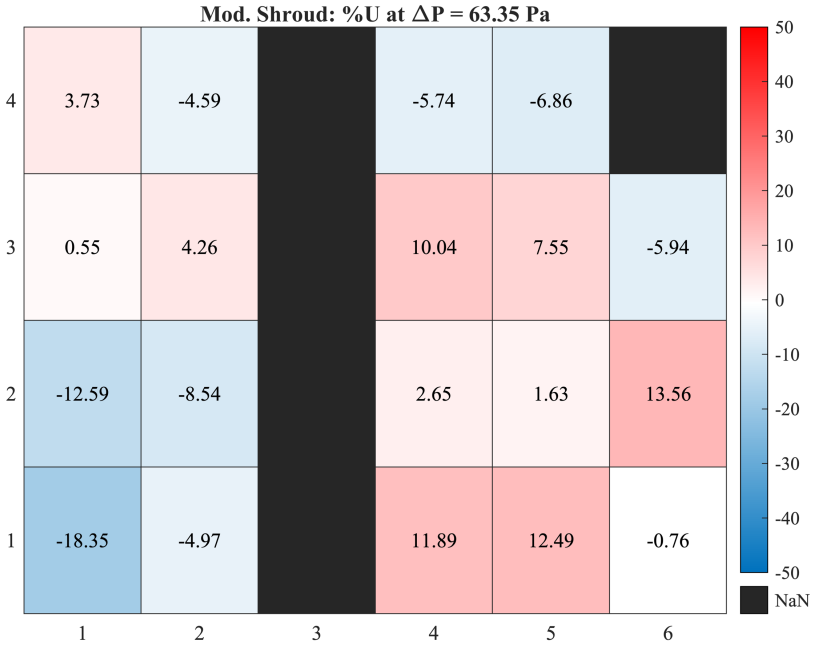

Figure E.3: Velocity Percent Difference at ΔP = 63.35 Pa (U_{avg} = 1.49 m/s)

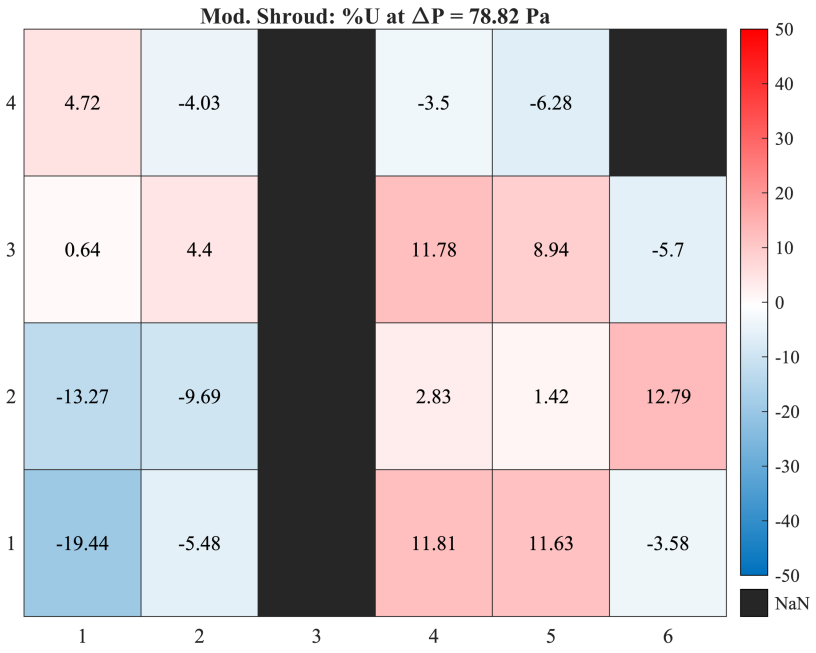

Figure E.4: Velocity Percent Difference at ΔP = 78.82 Pa (U_{avg} = 1.68 m/s)

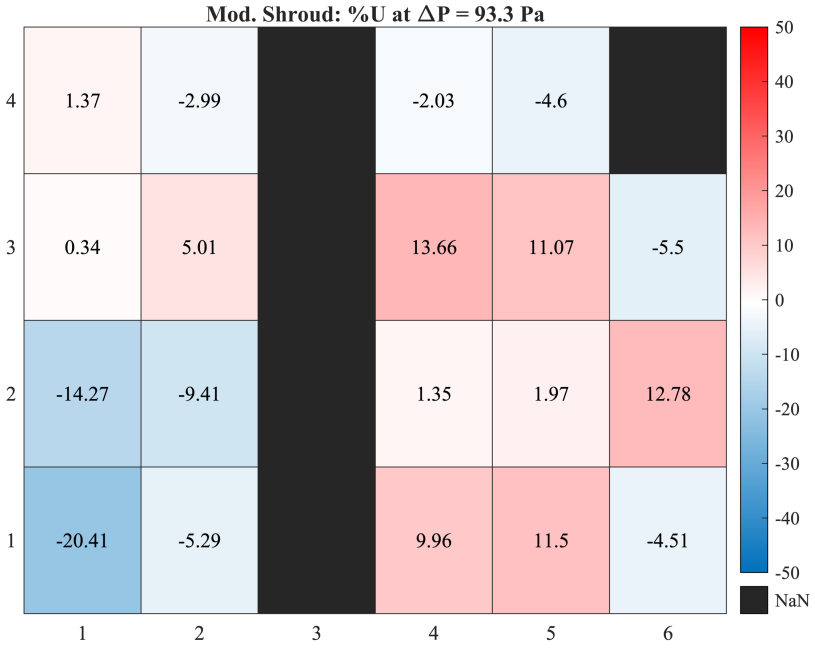

Figure E.5: Velocity Percent Difference at ΔP = 93.30 Pa (U_{avg} = 1.83 m/s)

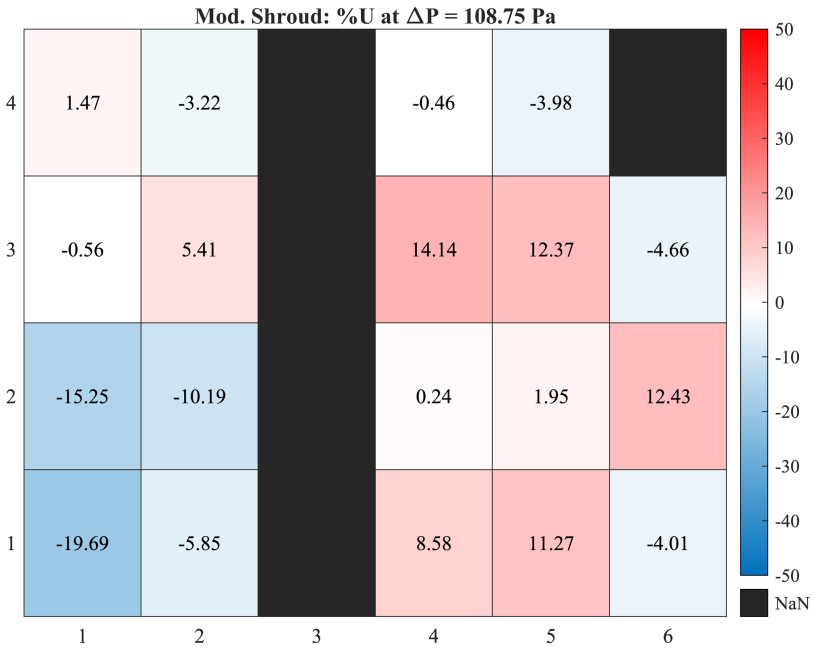

Figure E.6: Velocity Percent Difference at ΔP = 108.75 Pa (U_{avg} = 2.00 m/s)

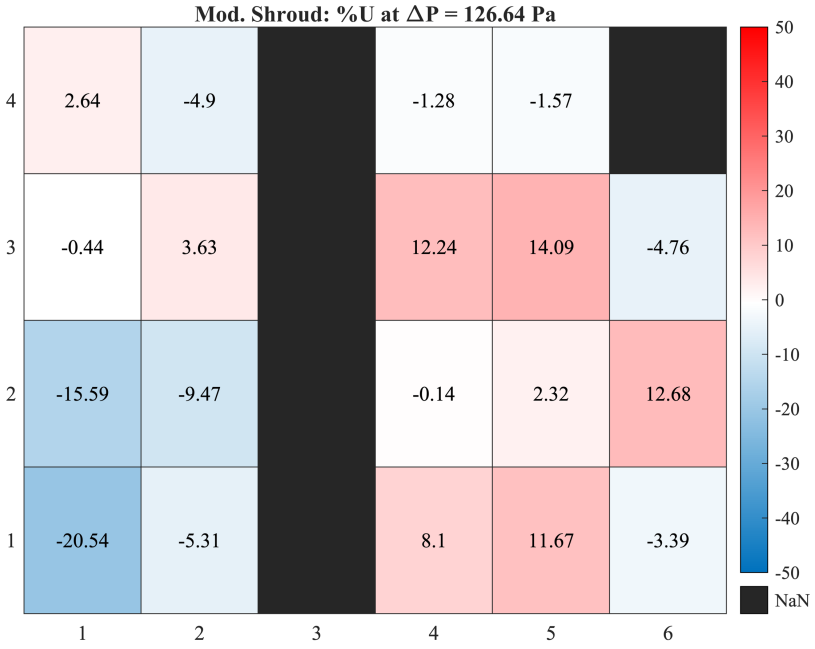

Figure E.7: Velocity Percent Difference at ΔP = 126.64 Pa (U_{avg} = 2.17 m/s)

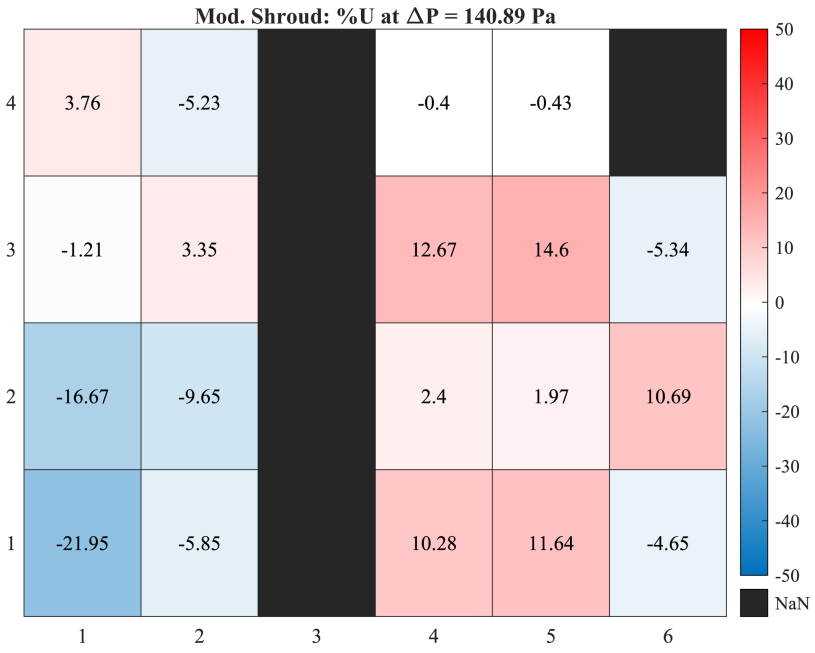

Figure E.8: Velocity Percent Difference at ΔP = 140.89 Pa (U_{avg} = 2.30 m/s)

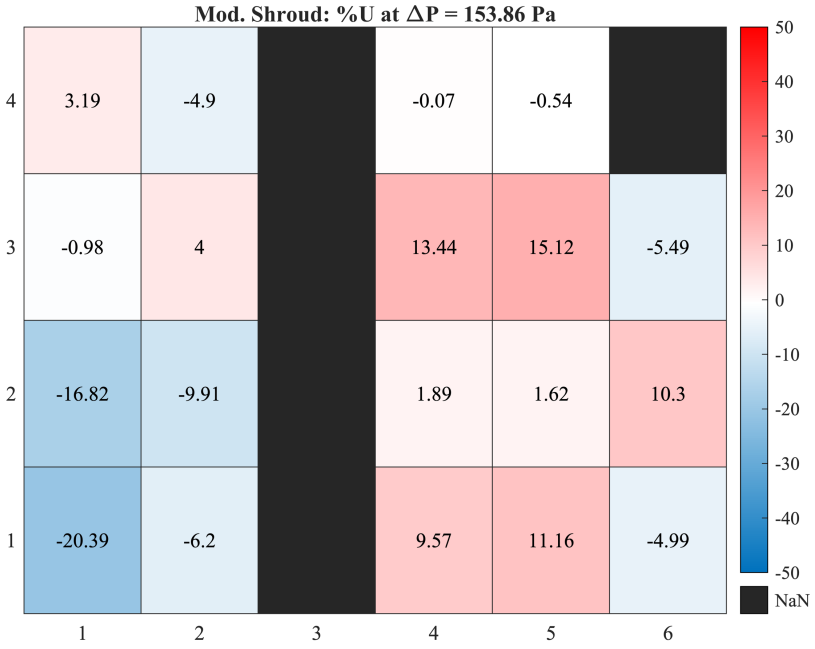

Figure E.9: Velocity Percent Difference at ΔP = 153.86 Pa (U_{avg} = 2.42 m/s)

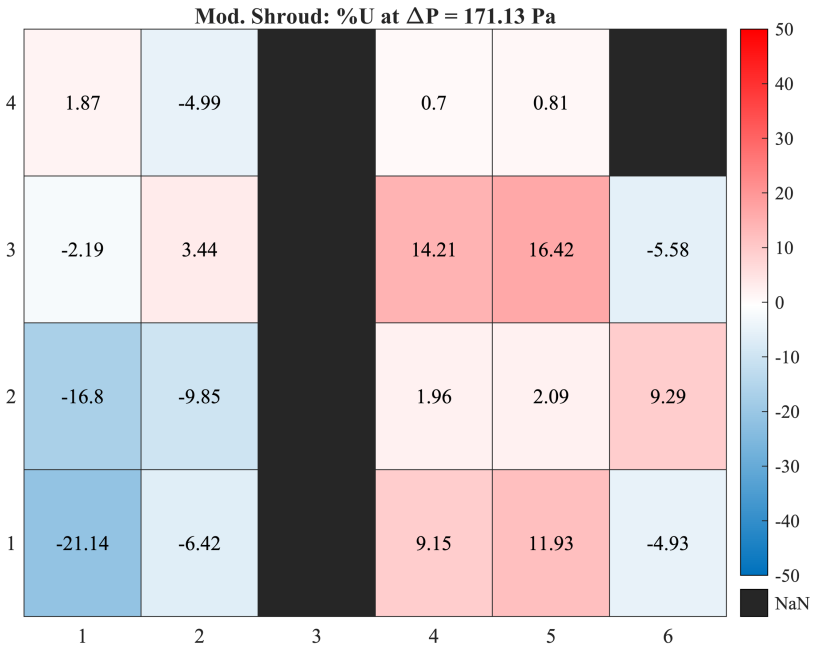

Figure E.10: Velocity Percent Difference at ΔP = 171.13 Pa (U_{avg} = 2.42 m/s)

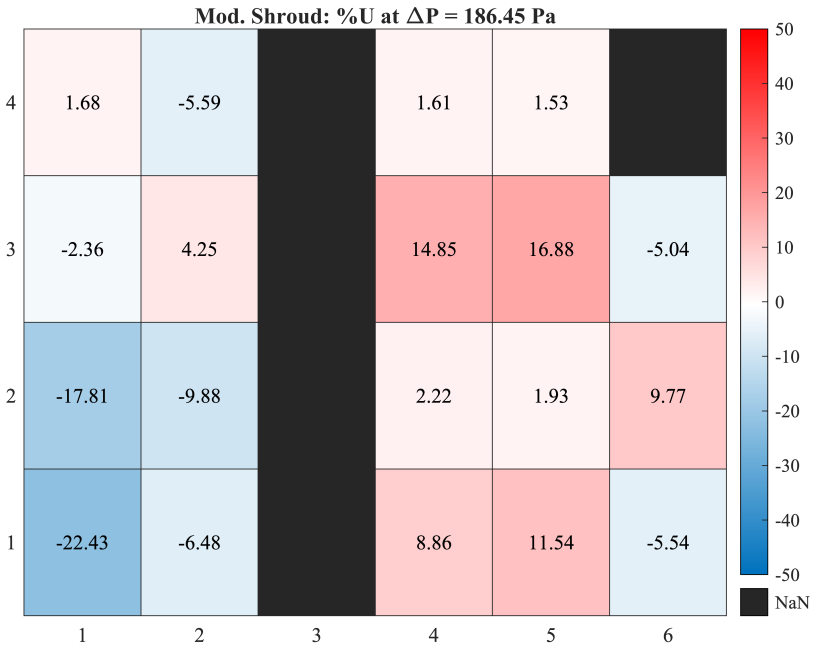

Figure E.11: Velocity Percent Difference at ΔP = 186.45 Pa (U_{avg} = 2.70 m/s)

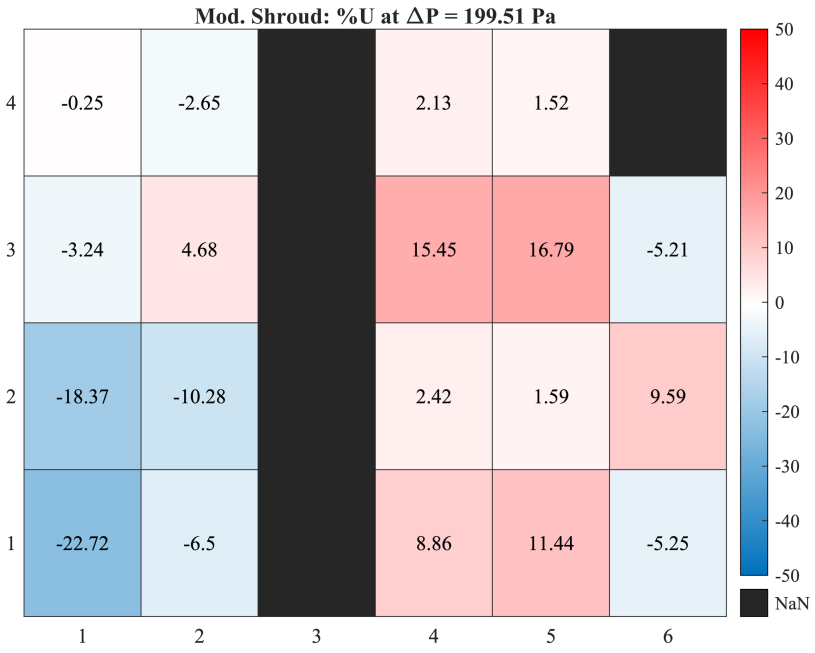

Figure E.12: Velocity Percent Difference at ΔP = 199.51 Pa (U_{avg} = 2.81 m/s)

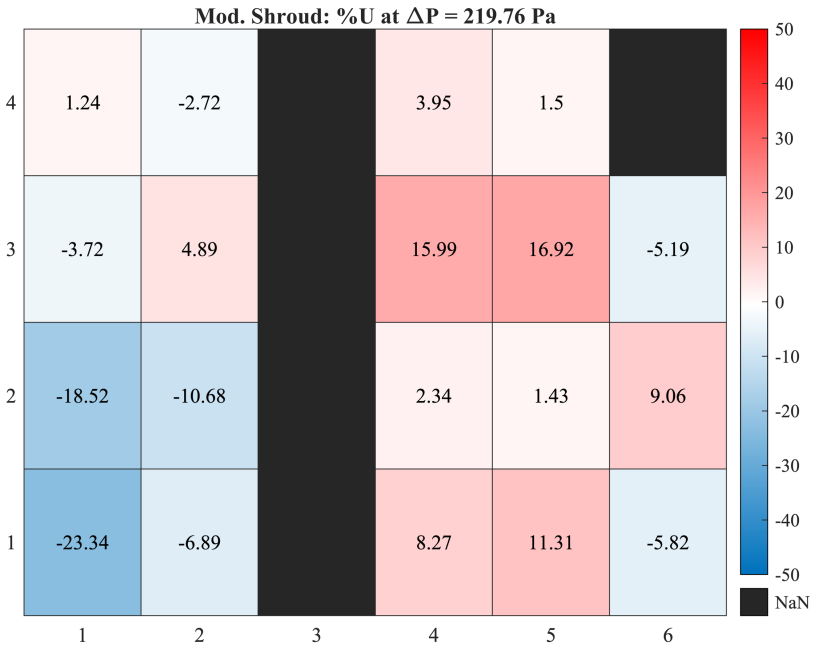

Figure E.13: Velocity Percent Difference at ΔP = 219.76 Pa (U_{avg} = 2.98 m/s)